Office of Energy Efficiency & Renewable Energy

National Renewable Energy Laboratory

Innovation for Our Energy Future

Fundamental Research and Development for Improved Crystalline Silicon Solar Cells

Final Subcontract Report
March 2002 — July 2006

A. Rohatgi
Georgia Institute of Technology
Atlanta, Georgia

Subcontract Report
NREL/SR-520-42324
November 2007

NREL is operated by Midwest Research Institute • Battelle Contract No. DE-AC36-99-GO10337

Fundamental Research and Development for Improved Crystalline Silicon Solar Cells

Final Subcontract Report
March 2002 — July 2006

A. Rohatgi
Georgia Institute of Technology
Atlanta, Georgia

NREL Technical Monitor: R. Matson/F. Posey-Eddy

Prepared under Subcontract No. AAT-2-31605-02

Subcontract Report
NREL/SR-520-42324
November 2007

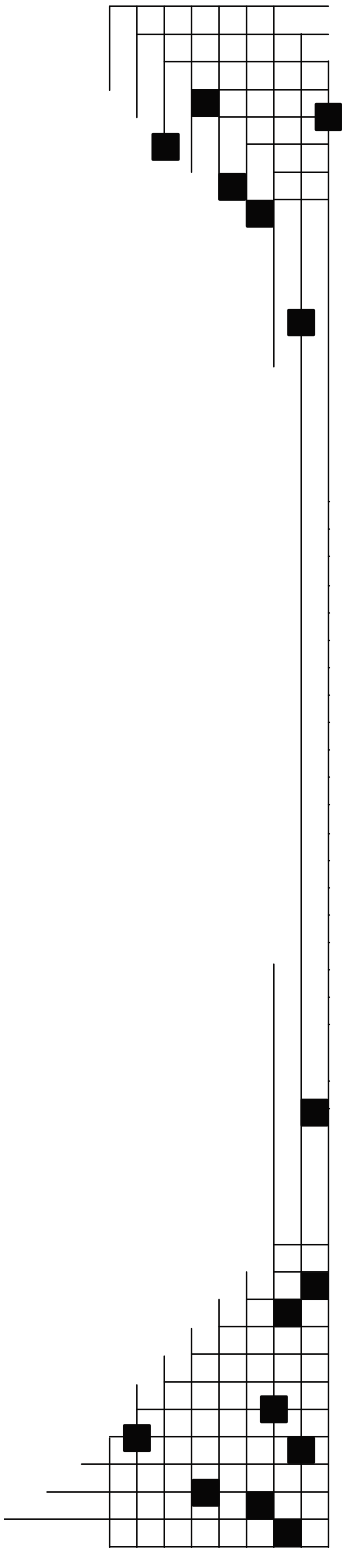

National Renewable Energy Laboratory
1617 Cole Boulevard, Golden, Colorado 80401-3393
303-275-3000 • www.nrel.gov

Operated for the U.S. Department of Energy
Office of Energy Efficiency and Renewable Energy
by Midwest Research Institute • Battelle

Contract No. DE-AC36-99-GO10337

Table of Contents

Summary

This report summarizes the progress made by Georgia Tech in the 2002-2006 period towards high-efficiency low-cost crystalline silicon solar cells under NREL Project # RCQ-1-31605 entitled Development of Low-Cost High-Efficiency Silicon Cells Through Fundamental Understanding of Critical Material and Technology Issues". The overall goal of the program is to improve the cost effectiveness of crystalline silicon photovoltaics by advancing the current understanding of hydrogen passivation and removal of harmful defects in silicon along with the development of novel conductive pastes and technologies for low resistance screen printed contacts. This program emphasizes fundamental and applied research on commercial substrates and manufacturable technologies. A combination of material characterization, device modeling, technology development, and complete cell fabrication are used to accomplish the goals of this program. This report is divided into five sections that summarize our work on *i) PECVD SIN-induced defect passivation (Sections 1 and 2); ii) the effect of material inhomogeneity on the performance of mc-Si solar cells (Section 3); iii) a comparison of light induced degradation in commercially grown Ga- and B-doped Czochralski Si ingots (Section 4);and iv) the understanding of the formation of high-quality thick-film Ag contacts on high sheet resistance emitters (Section 5).*

In Section 1, we investigate bulk defect hydrogenation via PECVD SiN deposition and anneal. We have found that a PECVD SiN film deposited at a frequency of ~150 KHz at ~400 °C is superior to the SiN deposited with a frequency of 13.56 MHz at 300 °C, despite the fact that the high-frequency SiN film contains more atomic hydrogen in the form of Si-H and N-H bonds. This suggests an additional source of hydrogen for the low-frequency SiN film, which is attributed to NH_3 pre-treatment during the low-frequency SiN deposition. The low-frequency SiN film showed an optimum hydrogenation temperature of ~750 °C while the high-frequency SiN film showed the optimum at ~800 °C in RTP. A ~2 μs as-grown lifetime increased to ~25 μs after 850 °C firing and ~50 μs after ~750 °C firing of the high- and low-frequency SiN films, respectively. A complete process sequence was developed through fundamental understanding to achieve record-high efficiency EFG Si cells. RTP contact firing with fast ramp-up and cooling gave ~1.4% increase in absolute cell efficiency compared to the slow belt firing used in production. This improvement was largely due to bulk lifetime enhancement associated with rapid cooling in RTP, which enhances the retention of hydrogen at the defects in EFG Si cells. It was found that the RTP contact firing (~700 °C/1 s) of the low-frequency SiN film with fast cooling rate (≥ 40 °C/s) could preserve the hydrogenated bulk lifetime due to higher retention of hydrogen a the defects. A two-step RTP processes, involving defect passivation at ~750 °C/60 s and screen-printed contact firing at ~700 °C/1 s, produced a record-high cell efficiency of 15.9% on Si ribbon.

In Section 2, we analyze the electrical activity of defects in ribbon mc-Si by scanning room-temperature photoluminescence spectroscopy before and after hydrogen passivation. This analysis revealed a strong inhomogeneity in the increase of minority carrier lifetime caused by the hydrogen defect passivation in mc-Si. We present experimental evidence that RTP-Al/SiN_x processing leads to strong lifetime enhancement caused by hydrogen defect passivation in low lifetime regions of mc-Si wafers. Additional details on the hydrogenation mechanism are revealed in a course of the de-hydrogenation study. Hydrogen out-diffusion shows a different rate or activation energy between high and low lifetime regions on the wafers.

The effect of material inhomogeneity on open-circuit voltage of String Ribbon Si solar cells is investigated by a combination of experimental results and a simple analytical

model in Section 3. Light beam-induced current measurements showed that a cell with no detectable defective region gave an efficiency of 15.9% with V_{OC} of 616 mV. However, a neighboring cell with highly defective regions covering 38% of its area, as determined by LBIC measurements, gave an efficiency of 14.1% with V_{OC} of 578 mV. Another cell with 19% highly defective regions gave an efficiency of 15.0% with V_{OC} of 592 mV. A simple and approximate analytical model was developed to quantify the loss in V_{OC} on the basis of recombination intensity and the area fraction of defective regions. This model showed that the majority of the loss in V_{OC} is associated with the most defective region, even if its area fraction is relatively small.

A systematic study of the variation in resistivity and lifetime on cell performance, before and after light-induced degradation in commercially grown B- and Ga-doped Cz ingots is presented in Section 4. Manufacturable screen-printed solar cells were fabricated and analyzed from different locations on the ingots. Despite the large variation in resistivity (0.57 to 2.5 Ω-cm) and lifetime (100-1000 μs) in the Ga-doped Cz ingot, the efficiency variation was found to be ≤ 0.5% with an average efficiency of ~17.1%. No LID was observed in these cells. In contrast to the Ga-doped ingot, the B-doped ingot showed a relatively tight resistivity range (0.87 Ω-cm to 1.22 Ω-cm), resulting in smaller spread in lifetime (60-400 μs) and efficiency (16.5-16.7%) along the ingot. However, the LID reduced the efficiency of these B-doped cells by about 1.1% absolute. Additionally, the use of thinner substrate and higher resistivity (4.3 Ω-cm) B-doped Cz was found to reduce the LID significantly, resulting in an efficiency reduction of 0.5-0.6% as opposed to >1.0% in ~1 Ω-cm ~17% efficient screen-printed cells. As a result, Ga-doped Cz cells gave 1.5% and 0.7% higher stabilized efficiency relative to 1 Ω-cm and 4.3 Ω-cm B-doped Cz Si cells, respectively.

Finally in Section 5, the physical and electrical properties of screen-printed Ag thick-film contacts are studied in an effort to understand and achieve good ohmic contacts to high sheet-resistance emitters. A combination of cross-sectional SEM/TEM, AFM, and SIMS measurements is used to analyze the Ag-Si interface and explain the electrical performance of three different screen-printed Ag pastes (A, B, and PV168) subjected to high and low-temperature firing conditions. Contact-resistance measurements and the solar cell parameters are used to establish a correlation between the electrical and physical properties of screen-printed contacts. Interface analyses showed that Ag does not make a full area contact to Si. Instead, there are dispersed Ag crystallites that are in direct contact to a small fraction of Si underneath the Ag grid. It was also found that larger Ag crystallites are formed at higher firing temperature, thus increasing the Ag-Si contact area fraction. At 750°C firing, all three pastes failed on a 100 Ω/sq emitter; PV168 and paste A failed because of a much smaller Ag crystallites and Ag-Si contact area fraction at the interface, and paste B failed because of excessive Ag penetration into the p-n junction. At a higher firing temperature of ~835°C, conventional paste A failed because of excessive diffusion of Ag and impurities into the emitter region which degraded the contact quality. Paste B failed because of the formation of very large (0.6-1 μm) Ag crystallites, which shunted the p-n junction. Of the three pastes, only the PV168 paste from DuPont gave acceptable contact quality on a 100 Ω/sq emitter with a solar cell fill factor (FF) of 0.782. This was the result of a more uniform distribution of re-grown Ag crystallites at the Ag-Si contact interface, in conjunction with significantly reduced Ag penetration into the Si emitter region.

1. PECVD SiN-Induced Defect Passivation and Rapid Thermal Processing for High-Efficiency EFG Silicon Solar Cells

1.1 Hydrogen Content and Defect Passivation Capability of Low- and High-Frequency PECVD SiN Films

Hydrogenation capability of a PECVD SiN can be a function of the deposition conditions such as plasma excitation frequency, deposition temperature, a ratio of NH_3 to SiH_4, or a pre-deposition NH_3 treatment. In this report, we investigated two different PECVD SiN films for defect passivation of EFG Si solar cells. A PECVD SiN film deposited with a plasma excitation frequency of 13.56 MHz at 300 °C is referred to as SiN-(1) while the SiN-(2) film was deposited at ASE Americas, using a frequency of 150 KHz and at temperatures of ≥ 400 °C in a tubular reactor.

Table 1-1 shows the difference in the important deposition variables for the two different SiN films used in this investigation. FTIR measurements were performed on the two SiN films, which showed that the SiN-(1) contains ~2.5 times more atomic hydrogen than the SiN-(2) after deposition but slightly less after the annealing at 850 °C for 2 min. It is important to note that FTIR only detects the atomic hydrogen in the form of Si-H and N-H bonds. Since the data in Table 1-1 indicates that much more atomic hydrogen is released from the SiN-(1) after 850 °C anneal, one would expect more hydrogenation from the SiN-(1).

Table 1-1. Deposition variables and characteristics of two different PECVD SiN films.

Variable	SiN-(1)	SiN-(2)
Excitation frequency	13.56 MHz	150 KHz
Deposition temperature (°C)	300	~400
Thickness (Å) as-deposited	~830	~780
Thickness (Å) after anneal	~750	~750
H content (cm^{-3}) as-deposited	2.5×10^{22}	1.1×10^{22}
H content (cm^{-3}) after anneal	$\sim5\times10^{21}$	$\sim7\times10^{21}$
Surface pre-treatment	None	NH_3 gas flow prior to SiN deposition

However, Figure 1-1 shows that this is not the case for the two different heat treatments in RTP: 700 °C/1s and 850 °C/120 s. These treatments were established for front contact and BSF formation, respectively. It was found that the SiN-(1) produced greater lifetime enhancement at 850 °C than 700 °C. On the contrary, the SiN-(2) showed that hydrogenation at 700 °C is much more effective than at 850 °C. In addition, the final lifetime values for the SiN-(2) passivation are much higher than the SiN-(1) for both the annealing conditions. This seems contrary to the FTIR data, which showed greater release of hydrogen from the SiN-(1). Furthermore, dehydrogenation seems more important for the SiN-(2) than the supply of hydrogen because 700 °C anneal gives superior passivation than

850 °C. This could happen if there is another large source of atomic hydrogen, in addition to the Si-H and N-H bonds inside the film, which makes the defect passivation dehydrogenation-limited rather than supply-limited. At low frequencies, the ions in the plasma can follow the excitation frequency and hence are expected to have higher energy and cause more damage to the wafer surface. In addition, the surface pre-treatment with NH_3 gas during the SiN-(2) deposition can implant hydrogen into the Si surface. According to Sopori et al. [NCPV Review Meeting, Colorado, 2001], surface damage in Si can absorb (or trap) a lot of atomic hydrogen. This form of hydrogen may not show up in the FTIR measurements but may be readily available for release and diffusion. Thus defect passivation using the SiN-(2) may not be limited by the supply of atomic hydrogen from the SiN film but by the retention of hydrogen at the defects. In order to support this hypothesis, a study was conducted in the next section, with and without the NH_3 surface pre-treatment.

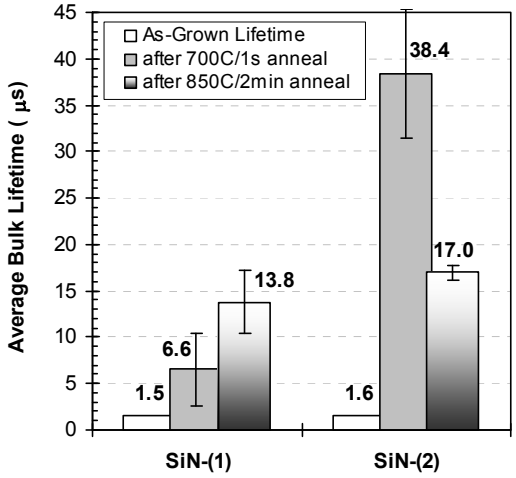

Figure 1-1. Comparison of bulk lifetimes in the EFG Si samples coated with two different PECVD SiN films. After SiN deposition on the front and Al screen-printing on the back, the samples were annealed simultaneously at 700 °C and 850 °C in RTP.

1.1.1 Impact of Surface Pretreatment with NH3 Prior to PECVD SiN Deposition

A systematic experiment was designed and conducted to understand the role of NH_3 surface pre-treatment on the degree of defect passivation of EFG Si. In this experiment, EFG Si wafers with the as-grown bulk lifetime of ~2 μs were used. After P diffusion at 930 °C for 6 min in the belt furnace, the bulk lifetime of the samples increased to ~6 μs due to P gettering. Then, the SiN-(2) film was deposited without (Scheme A) and with (Scheme B) the surface pre-treatment with NH_3 followed by 700 °C anneal in RTP to induce hydrogen passivation of defects.

It was found that annealing of SiN-(2) without the NH_3 pre-treatment (Scheme A) increased the bulk lifetime to ~18 μs while annealing of SiN-(2) with the NH_3 pre-

treatment (Scheme B) raised the bulk lifetime to ~36 μs (Figure 1-2). This clearly shows that the NH_3 pre-treatment helps the hydrogenation of defects in EFG Si. More research needs to show that this is due to hydrogen implantation or absorption of more atomic hydrogen at the Si and SiN interface.

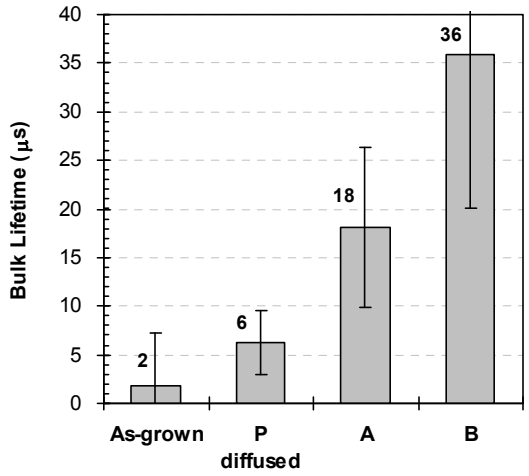

Figure 1-2. Effect of the surface pre-treatment with NH_3 during SiN-(2) deposition of EFG Si without the pre-treatment (A) and with the pre-treatment (B).

Figure 1-3 shows an identical experiment performed for the SiN-(1) film, which was deposited at 13.56 MHz PECVD reactor. Contrary to the SiN-(2), the SiN-(1) did not show the beneficial effect of the NH_3 pre-treatment. This could be related to lower surface damage or less hydrogen implantation due to lower ion energy at this high frequency.

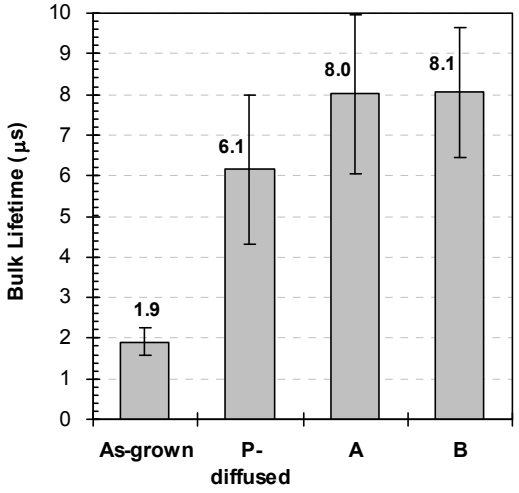

Figure 1-3. Effect of the surface pre-treatment with NH_3 on SiN-(1)-induced defect passivation of EFG Si.

In order to understand the relative importance of the release and diffusion of hydrogen versus retention of hydrogen for the defect passivation induced by the two SiN films, annealing temperatures were varied in the range of 600-900 °C in RTP. Figure 1-4 shows that the optimal annealing temperature for SiN-(2) was found to be ~750 °C as opposed to ~800 °C for SiN-(1). In addition, SiN-(2) increased the bulk lifetime to ~48 μs at ~750 °C while SiN-(1) gave a bulk lifetime of ~25 μs at ~800 °C, indicating that SiN-(2) is more effective in passivating defects in EFG Si. These results reveal that the optimal cell process sequence should be quite different for the two SiN films in order to maximize the hydrogen passivation of defects.

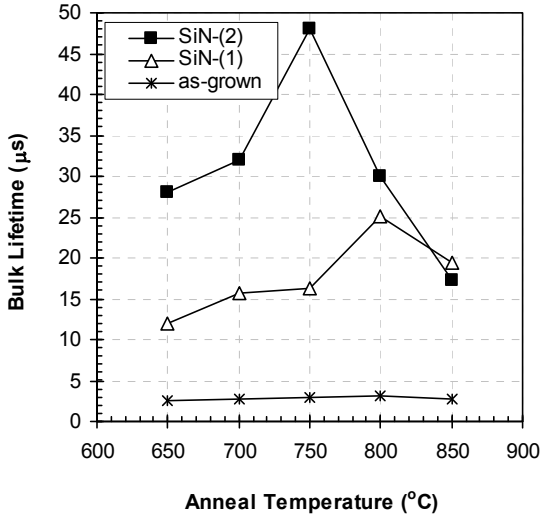

Figure 1-4. Bulk lifetime enhancement in EFG Si after annealing of SiN-(1) and SiN-(2) in RTP.

1.1.2 Impact of As-Grown Bulk Lifetime on SiN-(2)-Induced Defect Passivation of Screen-Printed EFG Silicon Solar Cells

In this section, screen-printed solar cells were fabricated on the SiN-(2)-coated EFG Si wafers with as-grown bulk lifetime in the range of 1-5 μs to study the impact of as-grown bulk lifetime on SiN-(2)-induced defect passivation. Since the two SiN films showed a very different degree of defect passivation as a function of the annealing temperature (Figure 1), the cells were fabricated using different firing schemes to maximize hydrogenation. The SiN-(1)-coated cells were fabricated, involving Al-BSF firing at 850 °C and Ag front contact firing at 740 °C in belt processing. For the SiN-(2)-coated cells, screen-printed Al on the back and Ag grid on the front were fired simultaneously at 700 °C for 1 s in RTP to achieve > 30 μs bulk lifetimes (Figure 1).

Figure 1-5 shows the cell efficiency of the screen-printed EFG Si solar cells with two-different SiN films. It was found that the SiN-(2)-coated cell efficiencies were much less dependent on the as-grown bulk lifetime compared to the SiN-(1)-coated cells. For example, the SiN-(2)-coated cells showed an absolute efficiency variation of less than 1% as opposed to ~3% for the SiN-(1)-coated cells for the as-grown bulk lifetimes in the range

of 1-5 μs. However, the efficiency difference between the two gradually decreased as the as-grown bulk lifetime increased. There was very little efficiency difference for the as-grown bulk lifetime of > 5 μs, which increased to ~50 μs for both the SiN films, using the different process sequences. For the as-grown lifetime of ~1 μs, the SiN-(1) gave a cell efficiency of ~11% while the SiN-(2) resulted in ~14% efficiency. Thus the SiN-(2) is more effective in improving poor quality as-grown EFG Si wafers compared to the SiN-(1).

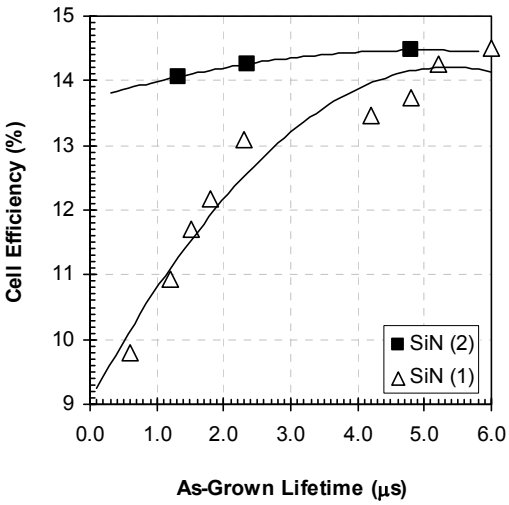

Figure 1-5. Efficiency of the screen-printed EFG Si cells with two-different SiN films as a function of as-grown bulk lifetime.

1.2 Process Design, Fabrication, and Analysis of High-Efficiency Screen-Printed EFG Si Solar Cells

A co-firing process in a conveyor belt furnace is commonly used in the PV industry to manufacture low-cost Si solar cells, where PECVD SiN AR coating and screen-printed (or pad-printed) Al-BSF and contacts are fired simultaneously. However, a short-and low-temperature belt co-firing could sacrifice the quality of Al-BSF in favor of contact quality.

EFG Si solar cells (2×2 cm^2) were fabricated using the two SiN films according to the four process sequences shown in Figure 1-6. The complete solar cells were analyzed to quantify the effect of each process sequence on bulk lifetime and solar cell parameters. Three separate solar cell runs were made for each process to account for the statistical variation in the as-grown property of EFG Si and validate the reproducibility of the cell parameters.

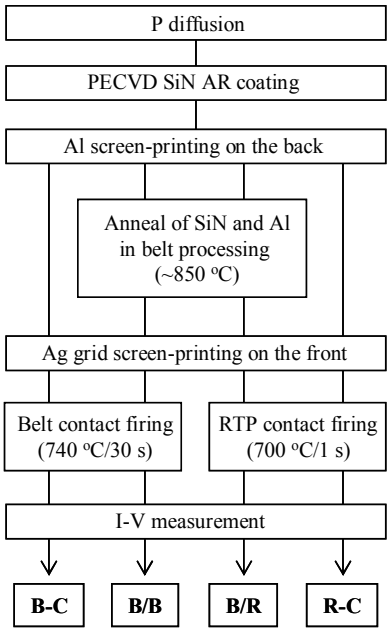

Figure 1-6. A design of four process sequences examined in this study for achieving effective defect passivation, Al-BSF, and contacts in EFG Si cells.

1.2.1 Development of Optimal Process Sequence for EFG Si Solar Cells with High-Frequency PECVD SiN

Table 1-2 summarizes the I-V results of the SiN-(1)-coated EFG Si cells fabricated using the four different process sequences outlined in Figure 1-6. The table shows the average, highest, and lowest efficiencies for about 55 EFG Si cells fabricated for each process scheme.

Table 1-2. I-V results of the screen-printed SiN-(1)-coated EFG Si solar cells for four different process schemes.

Process scheme	Voc (mV)	Jsc (mA/cm^2)	FF	Efficiency (%)		
				Average	High	Low
B-C	534.1	26.8	0.740	10.6	12.4	9.5
R-C	547.3	29.1	0.741	11.8	12.8	11.1
B/B	553.6	30.1	0.743	12.4	13.1	11.1
B/R	572.9	32.1	0.749	13.8	14.6	12.9

It was found that the co-firing schemes in the belt (Scheme B-C) and RTP (Scheme R-C) were less effective than the two-step firing schemes in the belt (Scheme B/B). Scheme B/R resulted in an average efficiency of 13.8%, which is ~1.4% higher in absolute efficiency than the scheme B/B, due to significantly higher Voc and Jsc. This indicates that the B/R

process scheme not only improves the Al-BSF quality but also enhances the defect passivation in the EFG Si cells.

Bulk lifetime is not so important for the FZ Si cells because the minority carrier diffusion length is much greater than the substrate thickness, both before and after cell processing. However, in low-cost EFG Si, the diffusion length in the as-grown state is generally much smaller than the substrate thickness, and it improves during the cell processing. As a result, both Voc and Jsc become very sensitive to process-induced bulk lifetime enhancement. Therefore, bulk lifetime measurements were performed on selected EFG Si samples before and after the cell processing to evaluate the effect of each process scheme on final bulk lifetime. In order to decouple the impact of contact firing induced hydrogenation, bulk lifetime was also measured after the 850 °C firing in the belt. This sample or process will be referred to as "B". Figure 1-7 shows the final bulk lifetime for the five different process schemes along with the as-grown bulk lifetime, which was somewhat low (1-2 μs) in this experiment. The figure shows the average values along with the standard deviation for 24 measurements.

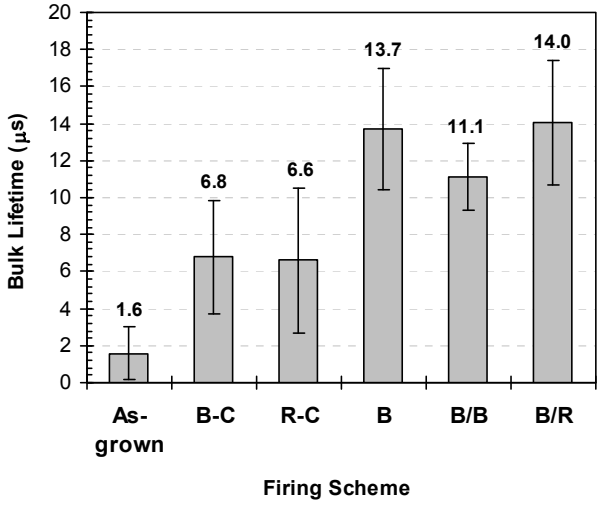

Figure 1-7. Bulk lifetime measurement results of the SiN-(1)-coated EFG Si for five different process schemes.

The average bulk lifetime went up from 1-2 μs to only 6.8 μs and 6.6 μs after the co-firing schemes B-C and R-C, respectively. This indicates that the co-firing of the SiN-(1) and Al at 700-740 °C is not very effective for the bulk lifetime enhancement in EFG Si. After firing the SiN-(1) and the Al simultaneously at 850 °C in the belt furnace, without a subsequent contact firing (Scheme B), the average bulk lifetime increased to 13.7 μs, indicating that the 850 °C firing in the belt furnace is much more effective in passivating defects than the co-firing at 700-740 °C either in the belt or RTP. A subsequent contact firing in the belt (Scheme B/B) was found to reduce the hydrogenated bulk lifetime to ~11 μs while the RTP contact firing (Scheme B/R) retained the hydrogenated bulk lifetime at ~14 μs. This difference is attributed to a higher retention probability of hydrogen at defects during the shorter and faster RTP contact firing at ~700 °C for ~1 s compared to the longer and slower belt contact firing at ~740 °C for 45 s, after the hydrogenation by the process B.

We found that, in very few cases, the average bulk lifetime did not correspond to the cell efficiency (Table 1-2 and Figure 1-7) because of the spatial non-uniformity of bulk lifetime in EFG Si. This is because very low lifetime regions, if present, can have greater influence on the cell performance. Since the average bulk lifetime values for the co-firing schemes B-C and R-C correspond to much smaller diffusion length (L < 200 μm) compared to the ~300 μm thick EFG Si substrates, the Al-BSF quality is not expected to have a significant effect on the cell efficiency. This is also supported by PC1D simulations, which showed a calculated efficiency difference of less than 0.5% for 300 μm-thick devices with diffusion length of less than 200 μm and BSRV values in the range of 102 to 104 cm/s. Thus the higher quality Al-BSF produced by the two-step firing scheme B/R, compared to the B/B and co-firing schemes, should have negligible effect on these EFG Si cells because diffusion length to the substrate thickness (L/W) ratio is much less than one. However, the EFG Si cell data in Table 1-2 show that the two-step firing scheme involving the RTP contact firing (Scheme B/R) produced 3.2% and 1.4% increase in absolute efficiency compared to the B-C and B/B processes, respectively. Since improved BSF due to the RTP contact firing cannot fully account for such huge increase in EFG Si cell efficiency, the RTP contact firing-induced improvement has to be attributed to the bulk lifetime enhancement. This is directly supported by the measured bulk lifetime data in Figure 1-7. The greater retention of the hydrogen at the defects during the RTP contact firing is the result of shorter firing time as well as the faster cooling rate (> 40 °C/s) compared to the slow cooling (< 10 °C/s) in the belt contact firing used in this study. Higher cooling rates help in retaining more hydrogen at the defects, resulting in a more effective defect passivation and higher bulk lifetime. Therefore, we conclude that the RTP contact firing improves the Al-BSF quality (or BSRV) due to high ramp-up rate and enhances bulk lifetime due to fast cooling. High-quality FZ Si cells, where L/W is much greater than one, primarily benefit from the improved BSRV; while the low-cost EFG Si cells, where L/W is smaller than one, benefit mostly from the improved bulk lifetime due to higher retention of hydrogen at defects.

It is important to note that this study was conducted using SiN-(1) film, which is not as effective as SiN-(2) when the as-grown lifetime value is low (1-2 μs), as shown in Section 1. Since the as-grown lifetime of EFG Si used in this study was less than 2 μs, the processed lifetime values with the SiN-(1) were well below 50 μs and the cell efficiencies were less than 15%. In Figure 1-5, we were able to achieve 14.5-15% efficient cells with SiN-(1) because the as-grown bulk lifetime was ~5 μs, as opposed to less than 2 μs. Thus SiN-(1) is not capable of raising the bulk lifetime of average EFG Si to over 50 μs using low-cost manufacturable technologies. Since Section 6.9 showed that SiN-(2) is more effective in hydrogenating low-lifetime EFG Si, the next section will focus on the fabrication and analysis of SiN-(2)-coated EFG Si cells to achieve higher efficiencies.

1.2.2 Development of Optimal Process Sequence for EFG Silicon Solar Cells with Low-Frequency PECVD SiN

The previous section showed that the best process sequence for SiN-(1)-coated EFG Si cells involved two-step firing (Scheme B/R). This process produced good BSF and contacts. However, hydrogenation was not sufficient to raise bulk lifetime to ~50 μs because of the fairly low as-grown lifetime of 1-2 μs. This resulted in average cell efficiencies below 14.0% with a maximum of ~14.5%. Therefore, in this section, EFG Si cells (2×2 cm^2) were fabricated using SiN-(2) using the same four process schemes (Figure 1-6). The as-grown bulk lifetime of the EFG Si used in this study was in the range of 1-2 μs.

Table 1-3 shows the I-V results of the EFG Si cells with SiN-(2) for the four different process schemes. The two-step firing scheme B/R, which was found to be best for SiN-(1), produced an average efficiency of 13.8% with a maximum efficiency of 14.9%. Contrary to SiN-(1) coating, the RTP co-firing (Scheme R-C) was found to be best for the SiN-(2)-coated EFG cells, resulting in an average efficiency of 14.3% with a maximum efficiency of 15% due to appreciably higher Jsc and Voc. Even the belt co-firing (Scheme B-C) was found to be more effective than the two-step B/B process. Thus the co-firing schemes seem to be better for SiN-(2) as opposed to two-step firing schemes for SiN-(1) for these four process schemes.

Table 1-3. I-V results of the screen-printed SiN-(2)-coated EFG Si solar cells for four different process schemes

Process Scheme	Average Voc (mV)	Average Jsc (mA/cm^2)	Average FF	Efficiency (%)		
				Average	High	Low
B-C	571.0	31.1	0.760	13.5	13.8	12.9
R-C	588.6	32.0	0.761	14.3	15.0	13.4
B/B	572.1	30.5	0.742	13.0	14.0	11.3
B/R	582.9	31.6	0.752	13.8	14.9	13.0

It is important to recognize that the overall cell efficiency of the SiN-(2)-coated EFG Si cells is appreciably higher than the SiN-(1)-coated cells for all the corresponding process schemes. These results are supported by the bulk lifetime measurements in Figure 1-8. The R-C process increased the average bulk lifetime from 1-2 μs to ~35 μs but is still less than 50 μs. Therefore, in the next section, we tried to optimize the hydrogenation temperature for SiN-(2) using the R-C process to achieve bulk lifetime over 50 μs.

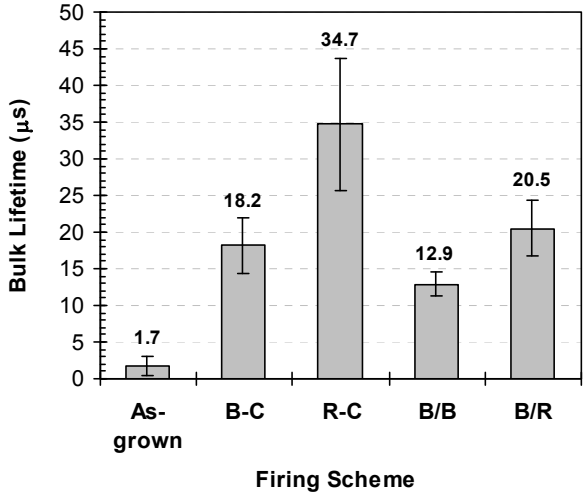

Figure 1-8. Bulk lifetime measurement results of the SiN-(2)-coated EFG Si for four different process schemes.

1.2.3 Optimization of Hydrogenation Temperature in RTP for Low-Frequency PECVD SiN to Achieve High-Efficiency EFG Si Cells with Photolithography Contacts

Since the optimum hydrogenation temperature of ~850 °C for the SiN-(1) in the belt furnace, the resulting optimum process sequence involved two-step firing (850 ^{o}C/2 min in the belt furnace and 700 °C/1 s in RTP), as discussed earlier. This sequence produced good contacts, BSF, and fairly effective hydrogenation. In the previous section, for the SiN-(2) we found that a relatively low temperature (700 °C) and short time (~1 s) RTP firing with fast cooling rate (> 40 °C/s) was very effective in producing good EFG Si cells (~15% efficiency). However, the firing condition may not be optimal for hydrogenation because the 700 ^{o}C/1 s firing condition was tailored to maintain good FF or screen-printed Ag contacts. Therefore, in this section, a study was conducted to determine the precise optimum hydrogenation temperature for the SiN-(2) in RTP and utilize it to achieve high-efficiency EFG cells first by using photolithography contacts, where we don't have to worry about the post-hydrogenation heat treatment because they are formed at the end.

1.2.4 Optimization of Hydrogenation Temperature for SiN-(2) in RTP

In this study, 10×10 cm^2 EFG Si wafers from the same growth were subjected to the P diffusion followed by the PECVD SiN-(2) coating on top of the emitter. After the screen-printing of Al on the back, the samples were fired in the RTP system at temperatures in the range of 600-850 °C for 60 s with two different cooling rates. To evaluate the degree of the SiN-(2)-induced hydrogenation, the fired samples were etched down to bare Si and immersed in the iodine-methanol solution for surface passivation for the bulk lifetime

measurement. The bulk lifetime was measured on ten different locations on each wafer and two wafers were used for each firing condition to account for nonuniformity.

Figure 1-9 shows the average bulk lifetime of the samples after the RTP firing of SiN-(2) and Al with two different cooling rates. The fast cooling rate (~40 °C/s) was ~40 times greater than the slow cooling rate. It was found that the slow cooling condition showed maximum bulk lifetime improvement at ~650 °C with the average lifetime of ~36 μs, as opposed to ~48 μs with a maximum of 74 μs for the ~750 °C anneal with fast cooling. This is the result of the competition between the release of atomic hydrogen from SiN, its diffusion through the bulk, and retention of hydrogen at the defects. These results show enhanced hydrogen passivation of defects at faster cooling rate due to higher retention of hydrogen at the defects. In addition, the 700 °C/60 s annealing increased the average bulk lifetime to ~40 μs, but the 850 °C/60 s annealing resulted in an average lifetime of only ~17 μs. This result explains why the two-step firing, involving the 850 °C hydrogenation in the previous section, was not very effective as it could be for SiN-(2). Furthermore, it also shows that 850 °C RTP firing is not appropriate for the SiN-(2)-induced hydrogenation. Figure 1-9 reveals that the 700 °C/1 s co-firing, which gave ~15% efficiency in the previous section, is sub-optimal for SiN-(2)-induced hydrogenation. In addition, the 750°C RTP firing, which is the optimum for the SiN-(2)-induced hydrogenation, is not good for screen-printed contacts because it gave low FF. These conflicts show the challenge of developing an optimal process sequence for EFG Si cells. Therefore, in the next section, EFG Si cells were fabricated with photolithography contacts first, using the optimum hydrogenation condition of ~750 °C/60 s in RTP.

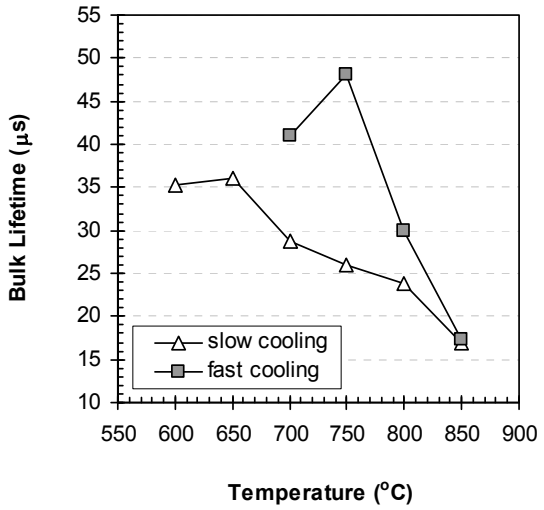

Figure 1-9. The average bulk lifetime along with standard deviation of EFG Si after the simultaneous firing of SiN-(2)/Al at temperatures of 600-850 °C in RTP. The firing time was fixed at 60 s.

1.3 Fabrication and Analysis of 15.8% Efficient EFG Si Solar Cell with Photolithography Contacts

In the previous section (Figure 1-9), we established that the optimal hydrogenation condition for SiN-(2) involved 750 °C /60 s firing in RTP, which could give the average bulk lifetime of ~50 μs required for ~16% efficient EFG Si cells with BSRV of 500-1000 cm/s. Unfortunately, the ~750 °C firing in the RTP is not suitable for screen-printed Ag grid contacts because it drives the metal too deep, causing junction shunting and low FF. Therefore, in this section, we decided to form evaporated metal contacts using lift-off photolithography after the hydrogenation of the cells at ~750 °C, Figure 1-10. This should result in the best hydrogenation and good contacts.

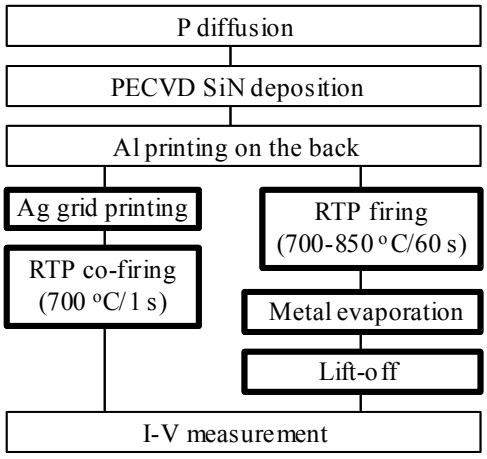

Figure 1-10. Process sequence and conditions used for fabricating the record-high efficiency EFG Si cells with the SiN-(2) and RTP firing. The left-hand side shows an industry screen-printed cell processing.

Table 1-4 shows the average efficiencies of the EFG cells (2×2 cm^2) as a function of the peak firing temperature in the range of 700-850 °C. As expected from the lifetime results in Figure 1-9, the ~750 °C firing was found to be best for maximum defect passivation, resulting in an average efficiency of 15.7% with a maximum of 15.8%. The efficiency drops on either side of ~750 °C. The reason for this optimum is that less hydrogen is released and diffused at temperatures below 750 °C while more hydrogen is dissociated from the defects at temperatures above 750 °C. This is supported by the bulk lifetime in Figure 1-9 and J_{sc} and V_{oc} values in Table 1-4. LBIC measurements were performed to map the electrical activity of defects over the cell area. In this technique, a He-Ne laser with wavelength of 905 nm is used to generate carriers, and the generated carriers are collected in short circuit mode to assess the recombination. Dark regions reflect less current collected or higher recombination. LBIC measurements in Figure 1-11 clearly show less recombination (more lighted regions) and higher spectral response (A/W) for the 15.8% efficient cell fired at ~750 °C.

Table 1-4. The result of I-V measurements on the EFG Si cells with photolithography contacts, in which the SiN-(2)/Al firing temperature was varied in the range of 700-850 °C in RTP.

Firing Temp. (^{o}C)	Voc (mV)	Jsc (mA/cm^2)	FF	Eff. (%)	Rs (Ω-cm^2)	Rsh (Ω-cm^2)
700	584	32.82	0.771	14.8	0.89	44193
750	603	33.19	0.785	15.7	0.60	50778
800	590	32.91	0.772	14.9	0.79	41321
850	567	30.26	0.764	13.1	0.64	42794

It is important to point out that once the SiN film was fired at ~750 °C it became very difficult to etch for a good lift-off photolithography. This caused appreciable amount of undercutting, resulting in somewhat wider openings than the photolithography grid design. In fact, the loss of current due to wider grid and FF of only ≤ 0.77 for these photolithography cells suggests that manufacturable screen-printed cells, which have wider grid and lower FF, with this hydrogenation condition could also give ~16% efficient cells. Therefore, in the next section, we developed a new process sequence using two-step firing in RTP to retain maximum hydrogenation while maintaining good screen-printed contacts.

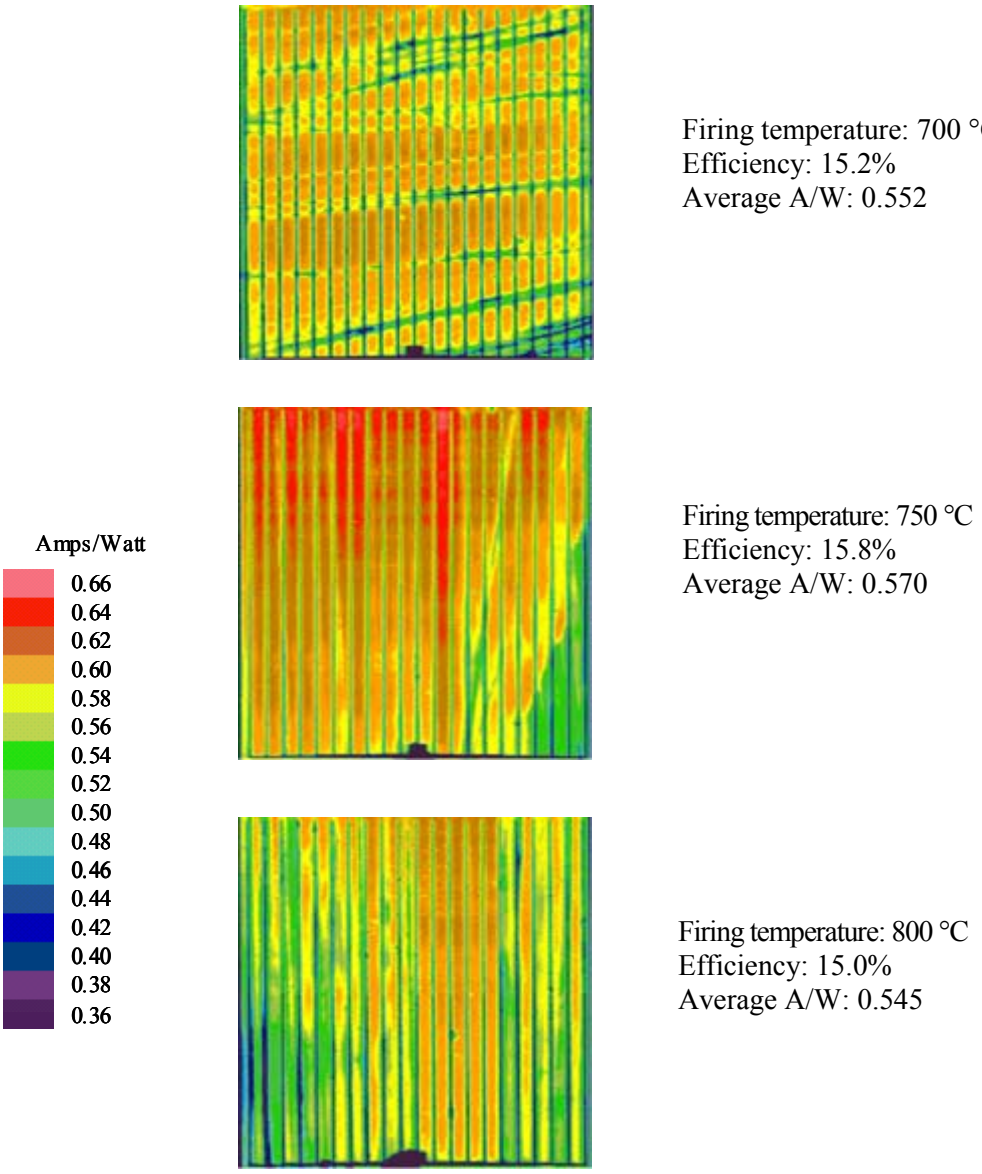

Figure 1-11. LBIC response of EFG Si cells fired at 700 °C, 750 °C, and 800 °C for 60 s in RTP. The values in the legend represent photo-response in A/W.

1.4 Fabrication and Analysis of Record-High Efficiency Screen-Printed EFG Silicon Solar Cell

Since low-cost screen-printed contacts are much more desirable and cost effective than the photolithography contacts, a new process sequence was established in this section that not only retains maximum defect passivation but also produces high-quality screen-printed contacts. Since the optimal hydrogenation condition (750 °C/60 s firing in RTP) is not appropriate for screen-printed contacts, we decided to use two-step firing: one for optimal hydrogenation and the second for good screen-printed contacts without loosing the hydrogen at the defects. Since post-hydrogenation anneal at high temperatures can cause dehydrogenation of defects, in this study, first we examined the extent of rapid cooling required for retaining the hydrogen at the defects.

EFG Si wafers were subjected to P diffusion, SiN-(2) deposition, and Al screen-printing, followed by an RTP annealing at ~750 °C for 60 s for maximum hydrogenation of the samples. After the hydrogenation, the samples were re-annealed in RTP to simulate contact firing at 700 °C for 1 s with four different cooling rates. Bulk lifetime measurements were performed to assess the impact of cooling rate associated with the RTP contact firing. This is important because hydrogen dissociates from the defects in EFG Si during post-hydrogenation annealing.

Figure 1-12 shows the relative change in bulk lifetime of hydrogenated EFG Si due to the RTP contact firing. As expected, the hydrogenated bulk lifetime decreased sharply for slow cooling rates. The slowest cooling rate (~1 °C/s) caused more than 50% reduction in bulk lifetime. This is attributed to reactivation of defects, resulting from evolution of the hydrogen from defects. At the cooling rate of ~30 °C/s, the reduction in the bulk lifetime was only ~3%. The hydrogenated bulk lifetime was completely preserved at the cooling rates of ≥ 40 °C/s.

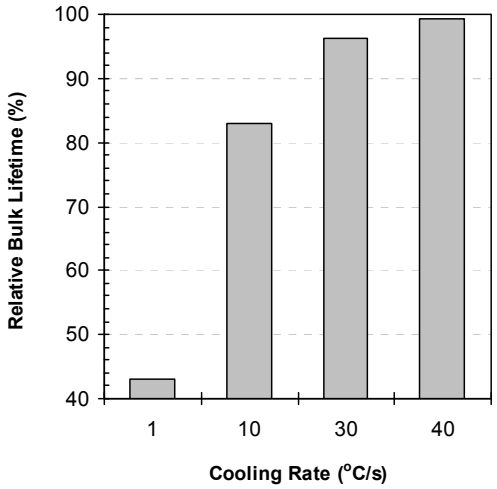

Figure 1-12. Relative bulk lifetime change of hydrogenated EFG Si due to RTP contact firing at ~700 °C for ~1 s with four different cooling rates.

In the previous sections, optimum hydrogenation condition for the SiN-(2) was found to be ~750 °C/60 s with a cooling rate of ≥ 40 °C/s, and the 700 °C/1 s RTP firing with ≥ 40 °C/s cooling rate could preserve hydrogenated bulk lifetime. In addition, we found that it could also produce good screen-printed contacts. This led to EFG Si cell fabrication with two-step RTP firing, involving ~750 °C/60 s for defect passivation using the SiN-(2) followed by ~700 °C/1 s for screen-printed contacts. Fast cooling rate of 40 °C/s was implemented for both steps.

Figure 1-13 shows a process sequence designed to take full advantage of the two optimized RTP firing steps for defect passivation and screen-printed contacts. Fabrication of EFG Si cells (2×2 cm^2) involved manufacturable P diffusion, PECVD SiN-(2) deposition, screen-printed metals, and two-step RTP firing. In this experiment, the RTP hydrogenation temperature was varied in the range of 730-780 °C to reestablish and support maximum defect passivation temperature of 750 °C for complete solar cells. As many as 61 EFG Si cells in three separate runs were fabricated to account for the statistical variation in property of EFG Si. The as-grown bulk lifetime was 1-2 μs, which represents average-quality EFG Si wafers.

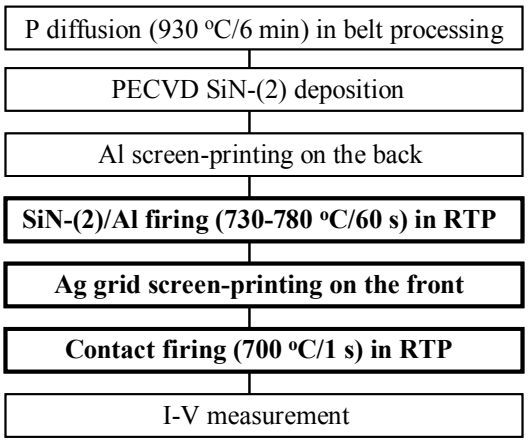

Figure 1-13. A process sequence for record high efficiency screen-printed EFG Si cells, involving two-step RTP for defect passivation and good contacts.

Tables 1-5A and 1-5B summarize the results of the screen-printed EFG Si cells as a function of the RTP hydrogenation temperature. Both average (Table 1-5A) and best (Table 1-5B) cell parameters for each hydrogenation temperature are shown. Note that ~750 °C hydrogenation in RTP was again found to be the optimum for defect passivation, resulting in average cell efficiency of 15% with a maximum of 15.9% for about 60 cells. Figure 1-14 shows that 15.9% represents the highest efficiency for screen-printed (or pad-printed) Si ribbon solar cells to date. Figure 1-15 shows the lighted I-V data for this record-high efficiency (15.9%) EFG Si cell (verified by National Renewable Energy Laboratory). This cell has excellent Voc of 615 mV, Jsc of 33.7 mA/cm^2, and FF of 0.769. This is the result of high bulk lifetime of > 50 μs, fairly good BSF, and high-quality screen-printed

contacts. Tables 1-5-A and 1-5-B show that for hydrogenation temperatures above 750 °C, the cell efficiency decreases rapidly because of reduced retention of hydrogen at defects. This is reflected in decrease of the Jsc and Voc values, despite better Al-BSF at higher temperature. It is noteworthy that the FFs are in the range of 0.761-0.783 because of very good contacts with low Rs (0.6-0.8 Ω-cm^2) and high Rsh (> 5×10^4 Ω-cm^2). This demonstrates that the short RTP contact firing at 700 °C is beneficial to both hydrogenation and screen-printed contacts due to fast cooling and heating rates.

Table 1-5A. The average parameters of the screen-printed EFG Si cells, in which two-step RTP firing was involved for defect passivation and contacts.

Hydrogenation Temp. (°C)	Voc (mV)	Jsc (mA/cm^2)	FF	Efficiency (%)
730	591	31.6	0.771	14.4
740	595	31.8	0.776	14.7
750	601	32.2	0.773	15.0
760	596	31.7	0.768	14.5
770	590	31.2	0.763	14.1
780	583	30.9	0.765	13.8

Table 1-5B. The best parameters of the screen-printed EFG Si cells, in which two-step RTP firing was involved for defect passivation and contacts.

Hydrogenation Temp. (°C)	Voc (mV)	Jsc (mA/cm^2)	FF	Efficiency (%)
730	605	32.6	0.771	15.2
740	607	32.8	0.773	15.4
750	615	33.7	0.769	15.9
760	610	33.1	0.770	15.5
770	600	32.2	0.781	15.1
780	598	31.6	0.771	14.6

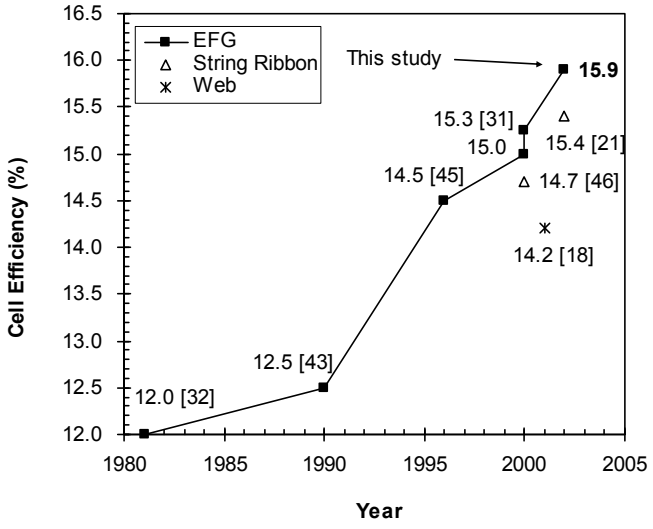

Figure 1-14. Efficiencies of screen-printed Si ribbon solar cells, involving the highest efficiency of 15.9% achieved in this thesis.

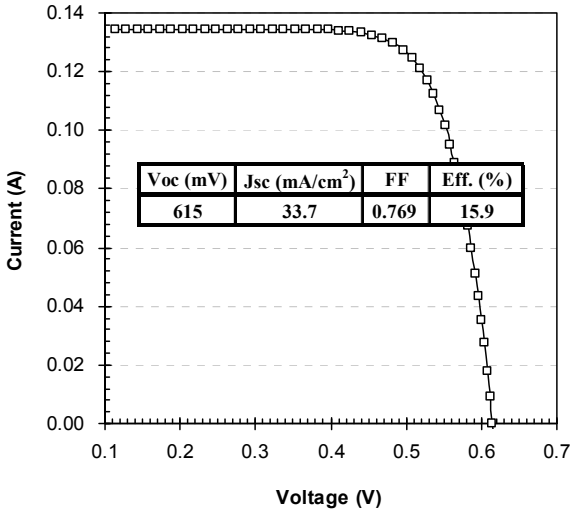

Figure 1-15. I-V curve for the 15.9% efficient screen-printed EFG Si solar cell, measured by National Renewable Energy Laboratory.

Figure 1-16 shows the efficiency distribution of the screen-printed EFG Si cells that were hydrogenated at the optimum temperature of ~750 °C. Efficiencies of about 60 cells were in the range of 14-16% with the most number of cells at ~15.2. The wide spread in efficiency is attributed to non-uniform distribution of impurities and defects in EFG Si. Figure 1-17 shows LBIC measurement on nine 2×2 cm^2 cells made on one 10×10 cm^2 EFG Si wafer. LBIC measurements show considerable nonuniformity of electrically active defects over the full wafer, even after the optimum hydrogenation. Although the efficiency of most cells on this wafer is ≥ 15%, Figure 1-17 shows a good correlation between the cell efficiency and the LBIC map.

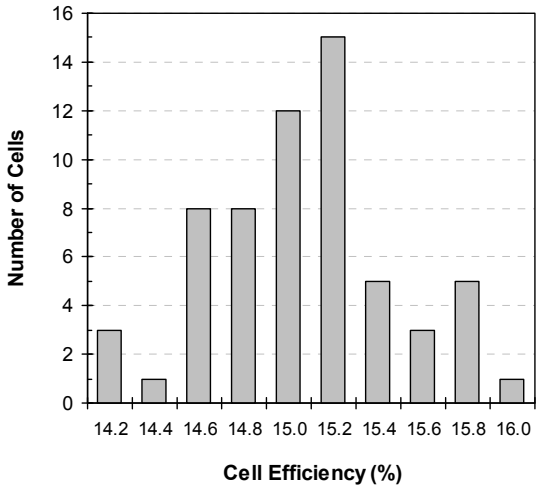

Figure 1-16. An efficiency distribution of 61 screen-printed EFG Si cells involving two-step RTP firing scheme.

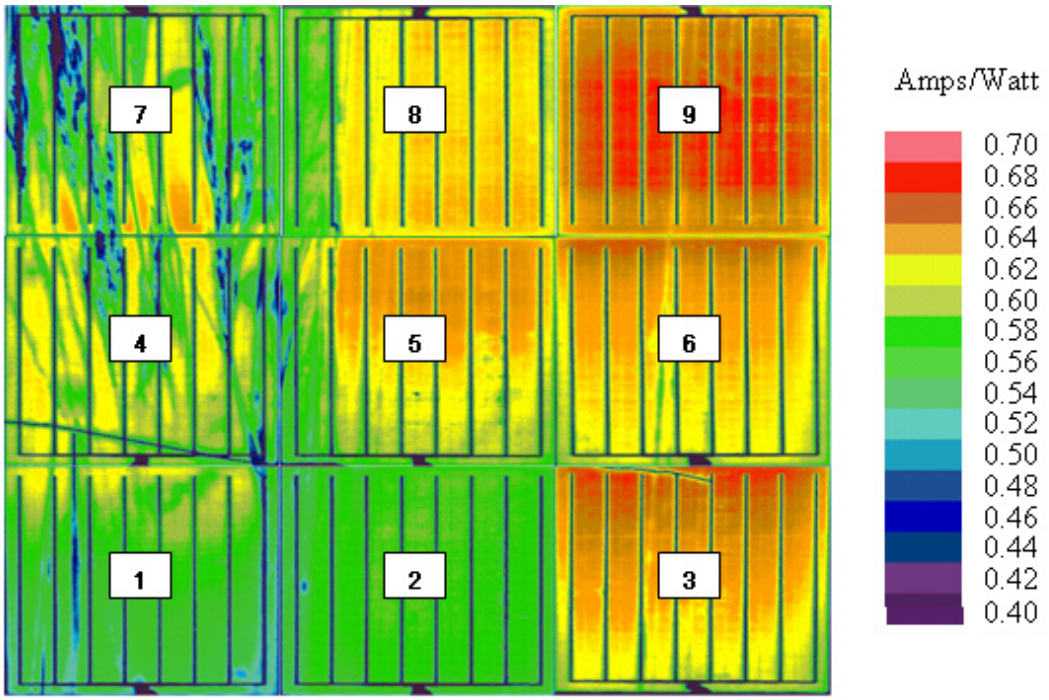

Figure 17. LBIC maps along with cell parameters of nine 2×2 cm^2 cells on a 10×10 cm^2 EFG Si, which were hydrogenated at 750 °C in RTP.

Cell No.	Voc (mV)	Jsc (mA/cm^2)	FF	Eff. (%)	LBIC response (A/W)
1	599	32.6	0.759	14.9	0.532
2	600	32.7	0.758	14.9	0.541
3	614	33.2	0.764	15.7	0.593
4	604	32.8	0.762	15.0	0.554
5	609	32.5	0.759	15.1	0.580
6	617	33.3	0.767	15.7	0.593
7	573	31.3	0.762	13.7	0.538
8	607	33.2	0.758	15.3	0.579
9	616	33.5	0.769	15.9	0.601

1.5 Conclusion

Hydrogenation due to PECVD SiN deposited with a frequency of ~150 KHz at ~400 °C was found to be superior to the SiN deposited with a frequency of 13.56 MHz at 300 °C, despite the fact that the high-frequency SiN film contained more atomic hydrogen in the form of Si-H and N-H bonds. This suggested an additional source of hydrogen for the low-frequency SiN film, which was attributed to NH_3 pre-treatment during the low-frequency SiN deposition. The low-frequency SiN film was found to be more effective in passivating defects in EFG Si with low as-grown bulk lifetimes (< 3 μs). The cell efficiency difference between the two SiN films decreased as the as-grown bulk lifetime increased to ~ 5 μs. The low-frequency SiN film showed an optimum hydrogenation temperature of ~750 °C while the high-frequency SiN film showed the optimum at ~800 °C in RTP. A ~2 μs as-grown lifetime increased to ~25 μs after 850 °C firing and ~50 μs after ~750 °C firing of the high- and low-frequency SiN films, respectively.

A complete process sequence was developed through fundamental understanding to achieve record-high efficiency EFG Si cells. For SiN-(1)-coated EFG Si cells, a two-step process scheme (~850 °C/2 min in the belt + ~700 °C/1 s in RTP) was found to be optimal for defect passivation and screen-printed contacts, resulting in an average efficiency of ~13.5% with a maximum of 14.6%. RTP contact firing with fast ramp-up and cooling gave ~1.4% increase in absolute cell efficiency compared to the slow belt firing used in production. This improvement was largely due to bulk lifetime enhancement associated with rapid cooling in RTP, which enhances the retention of hydrogen at the defects in EFG Si cells.

While a two-step firing, involving hydrogenation at 850 °C, was found to be best for EFG Si cells with SiN-(1), it was not appropriate for SiN-(2). This is because optimal hydrogenation temperature was found to be ~750 °C for SiN-(2)-induced defect passivation, compared to ~850 °C for SiN-(1). Since ~750 °C was too intense for screen-printed contacts, a two-step firing scheme was developed by optimizing the firing of screen-printed contacts after the hydrogenation. It was found that the RTP contact firing (~700 °C/1 s) with fast cooling rate (≥ 40 °C/s) could preserve the hydrogenated bulk lifetime due to higher retention of hydrogen a the defects. The two-step RTP processes, involving defect passivation at ~750 ^{o}C/60 s and screen-printed contact firing at ~700 °C/1 s, produced the record-high cell efficiency of 15.9% on Si ribbon to date.

2. RTP-Enhanced Hydrogen Passivation in Ribbon Multicrystalline Silicon Studied by Scanning Room-Temperature Photoluminescence Spectroscopy

2.1 Introduction

Impressive growth in the photovoltaic market over the past decade has been predominantly driven by advances in crystalline silicon technology. Multi-crystalline silicon (mc-Si), which is produced by many competing techniques, can meet low-cost production, high solar cells throughput and high efficiency requirements. The importance of the defect passivation or elimination in low-cost mc-Si wafers is recognized as a key requirement for achieving high efficiency solar cells. Solar cell production employs a set of process steps, which realize improvement in material's quality. These manufacturing steps include (a) phosphorous diffusion, (b) hydrogenation from the amorphous SiN_x:H layer, and (c) Al back contact firing. It was established recently that combined effect of simultaneous (b) + (c) steps using rapid thermal processing (RTP) technique provides additional benefits to solar cell efficiency through the hydrogen mediated defect reduction [2-3]. This new hydrogen passivation approach tentatively accounted for increased hydrogen incorporation in defect-enriched regions of mc-Si wafers and solar cells. In this paper, we report on scanning room-temperature photoluminescence (PL) spectroscopy study of the simultaneous rapid thermal annealing of Al on the back and SiN_x on the front (RTP-Al/SiN_x) hydrogenation mechanism.

2.2 Solar Cell Fabrication And Photoluminescence Analysis Procedures

For the PL excitation, the 800nm pulse AlGaAs laser diode with 140 mW peak power was used. PL mapping set-up and procedure are published elsewhere [2-4]. Materials used in this study were boron doped ~300 μm thick ribbon mc-Si wafers grown by Edge-defined Film-fed Growth (EFG) method. A set of commercial EFG wafers was prepared and processed as specified in Table 1. Each processing step was followed with PL mapping measurement at two principal luminescence bands as described below.

The PL spectrum of mc-Si wafers at room temperature is composed of two luminescence bands. First band (I_{BB}) shows a spectral maximum at 1.09eV and corresponds to band-to-band recombination in silicon. This band was characterized in a broad temperature range up to 750 K and attributed to direct recombination of free and bound to exciton electron-hole pairs [2-5]. The second "defect" band at 0.8 eV (I_{Def}) is observed only at selected regions on the wafer, and corresponds to deep luminescent defects located around the dislocation lines in mc-Si [2-6]. This defect band is a finger print of the low lifetime regions on wafers and caused by dislocations contaminated by impurity precipitates [2-4]. PL maps with reasonable spatial resolution can be used to deduce (a) the distribution of the effective minority carrier lifetime (τ_{eff}) [2-7], (b) the lifetime variation after a solar cell processing, and (c) the maps of the defect centers causing 0.8eV PL band. The τ_{eff} is composed of radiative, non-radiative, and surface recombinations and in general, dominated by non-radiative recombination in Si. In a

simple case neglecting a diffusion of the photo-generated minority carriers, the I_{BB} and I_{Def} can be expressed as following [2-4]:

$$I_{BB} = C_1 \times G \times \tau_{eff} / \tau_{rad} \qquad (1\text{-}2)$$

$$I_{Def} = C_2 \times G \times \tau_{eff} / \tau_{SRH} \qquad (2\text{-}2)$$

where G is the electron-hole pair's photo-generation rate, τ_{rad} is the radiative recombination lifetime, $\tau_{SRH} = (N_{Def}\, v_{th}\, \sigma_n)^{-1}$ is the Shockley–Read–Hall radiative lifetime, N_{Def} is the radiative defect concentration, v_{th} and σ_n are the electron thermal velocity and capture cross section, C_1 and C_2 are temperature dependent Si constants. A new parameter, $R = I_{Def} / I_{BB}$, can be introduced, to measure the point-by-point ratio of two PL intensities. Following Eqs. (2-1) and (2-2) it is clear that

$$R = I_{Def} / I_{BB} = \text{const} \times N_{Def} \qquad (3)$$

i.e. R-parameter allows directly accessing the PL defect concentration and their spatial distribution with the PL mapping procedure. Notice that the R-value is independent on other recombination defects in the bulk and at the surface, which contribute to τ_{eff}.

Table 2-1. Flow-chart of processing steps and PL results in EFG wafers. Average across the wafer values of the band-to-band PL (I_{BB}), defect band PL (I_{Def}) and R-parameter ($R= I_{Def}/ I_{BB}$) on sample #2 before and after each processing step are summarized.

	Sample stage	**Processing**	**I_{BB}**	**I_{Def}**	**R**
1	Initial		28.8	*)	*)
2	Hydrogenation	SiN_x deposition, Al back contact screen-print, RTP annealing at 750°C for 1sec, and removing SiN_x layer in 50% HF solution.	126.3	0.71	0.011
3	De-hydrogenation (600°C)	RTP annealing at 600°C for 1sec in N_2/O_2 ambient	112.5	0.61	0.013
4	De-hydrogenation (700°C)	RTP annealing at 700°C for 1sec in N_2/O_2 ambient	42.8	0.34	0.024

*) Defect band intensity is below sensitivity limit of the PL system.

2.3 Characterization of Defects in EFG Si Before and After Hydrogenation by Room Temperature PL Mapping

Figs. 2-1a and 2-1b show two PL maps, I_{BB} and I_{Def}, respectively, collected at identical sample spots on 50 mm × 22 mm EFG wafer after the 750 °C RTP-Al/SiN_x hydrogenation step. The distribution of I_{BB} maintains a profile of the effective lifetime according to Eq. (2-1) as published in [2-4]. The areas with low I_{BB} intensity correspond to high recombination activity of all defects (low lifetime regions), while the high I_{BB} values represent "good" or high lifetime regions. It was established previously that low I_{BB} regions are specified also by intense I_{Def} band, while in high I_{BB} regions this band is negligible [2-4]. This reverse contrast of I_{BB} and I_{Def} is illustrated in Figs. 2-1a and 2-1b after the hydrogenation was completed.

Hydrogenation leads to a significant increase in the band-to-band PL intensity (28.8 to 126.3) averaged across the sample, as presented in Table 2-1 (wafer #2). This effect can be interpreted as effective lifetime (τ_{eff}) upgrade due to RTP-Al/SiN_x processing [2-8]. In different samples we observed from 1.5 to 4.3 times hydrogenation-induced increase in average I_{BB} values. Notice that the defect band, which at initial stage had intensity below the PL system detection limit also increased in intensity after the hydrogenation due to the

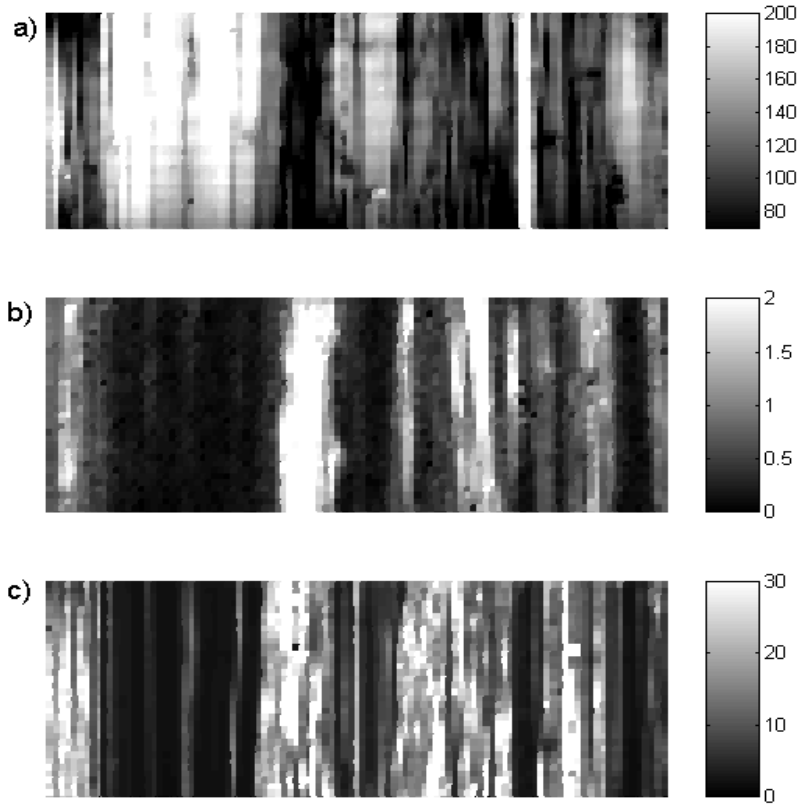

Figure 2-1. Room temperature PL mapping (a) band-to-band (b) defect band PL, and (c) point-by-point ratio of I_{BB} (hydrogenated)/I_{BB}(initial) representing lifetime upgrade effect. The mapping size is 50 mm x 22 mm, step=0.5 mm.

same effective lifetime upgrade according to Eq. 2-2. We observe that high PL and low PL areas on EFG wafers respond differently to the RTP-Al/SiN_x processing. Specifically, high I_{BB} areas prior to the hydrogenation show quite small, up to 30%, lifetime upgrade effect. In contrast, low I_{BB} areas show a spectacular lifetime upgrade, up to two orders of the magnitude, after the hydrogenation. Evidently, the average across the sample values of I_{BB} increase (Table 2-1) caused by hydrogenation represents a superposition of both areas. To illustrate the lifetime upgrade effect over the wafer one can introduce the upgrade coefficient as the point-by-point ratio of two band-to-band PL intensities, before and after the hydrogenation:

$$K_{up} = I_{BB}\,(\text{hydrogenated}) / I_{BB}\,(\text{initial}) = \tau_{eff}\,(\text{hydrogenated}) / \tau_{eff}\,(\text{initial}) \qquad (2\text{–}4)$$

The K_{up} map on the wafer #2 is plotted in Fig. 2-1c. To further quantify the lifetime upgrade, we show in Fig.2 PL data analyzed on two different areas on sample #2 with (a) "low" and (b) "high" band-to-band PL. Consistent with entire mapping in Fig. 2-1, low band-to-band PL area (a) shows in average 20-fold lifetime increase, while high band-to-band PL area (b) shows only 10% upgrade in lifetime. Notice that the y-axis on Fig. 2-2 has a logarithmic scale.

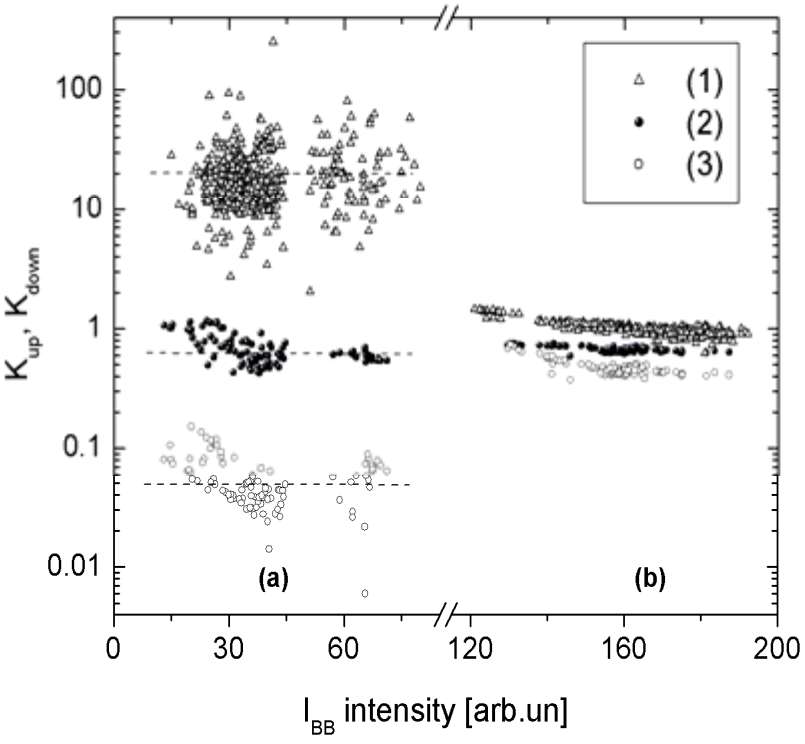

Figure 2-2. Lifetime up-grade and down-grade coefficients measured in areas with (a) low and (b) high band-to-band PL intensity; (1) corresponds to RTP-Al hydrogenation; (2) 600 °C RTP de-hydrogenation, and (3) 700 °C RTP de-hydrogenation.

Based on the above study, we conclude that RTP-Al/SiN_x hydrogenation significantly improves "bad" regions in EFG wafers, and has a little effect on the high lifetime areas.

To further explore the hydrogen incorporation mechanism in mc-Si, we performed two consecutive RTP annealings at 600 °C and 700 °C on the previously hydrogenated wafers after etching off the SiN_x:H layer (see Table 2-1 for the processing details). It was demonstrated recently that the average effective lifetime decreased after this processing step due to hydrogen out-diffusion, and reduction of bulk lifetime can lead to significant loss in solar cell efficiency [2-3]. In Table 2-1, we show PL results of such a de-hydrogenation experiment on wafer #2. Consistent with the lifetime data in literature, the RTP at 600 °C and 700 °C led to a gradual decrease in the PL intensity of both the luminescent bands, which is consistent with the hydrogen out-diffusion model for the observed lifetime down-grade [2-8].

Similar to the hydrogenation case, we analyzed the I_{BB} variation across the wafers after each de-hydrogenation anneal step. We calculated at every mapped spot the ratio of the band-to-band PL intensities after the RTP with respect to the hydrogenated stage by introducing the down-grade coefficient

$$K_{down} = I_{BB}\,(\text{de-hydrogenated}) \,/\, I_{BB}\,(\text{hydrogenated})$$

$$= \tau_{eff}\,(\text{de-hydrogenated}) \,/\, \tau_{eff}\,(\text{hydrogenated}) \qquad (2\text{-}5)$$

In Fig. 2-2, the K_{down} data points are shown for the same wafer regions as in the hydrogenation experiment, allowing comparing them with K_{up} distributions. In addition to the PL degradation across the entire sample, two other effects were observed. First, the low PL intensity region "a" showed much stronger lifetime downgrade than high PL region "b". Specifically, we observed up to 50-fold decrease in the PL intensity in the area "a" versus only a factor of two decrease in the area "b". Secondly, the PL intensity degradation due to RTP dehydrogenations anneal showed a different temperature annealing rate in "a" compared to "b" regions. This is evident by comparing points labeled as (2) and (3) in both areas. This indicates that the activation energies of the hydrogen out-diffusion process are quite different in both regions; lower in the low-lifetime regions and higher in the high lifetime regions. Moreover, the rapid decrease in I_{BB} in area "a" is in general agreement with the reported lifetime degradation [2-8]. To elaborate on details of the hydrogenation and de-hydrogenation processes, we present in Fig. 2-3 three PL line scans measured and calculated at identical wafer location. Data (a) represents the line-scan for the downgrade coefficient after the 700 °C RTP de-hydrogenation anneal. Notice that K_{down} shows up to 10 times reduction in lifetime in the areas marked by arrows. Data points in Fig. 2-3b represent R-parameter calculated according to Eq. (2-3) after the hydrogenation (open circles) and subsequent de-hydrogenation (closed circles) at 700 °C. First, notice that a clear inverse correlation between K_{down} and R-parameter or the radiative defect concentrations. Secondly, comparison of R-parameter distribution after the RTP-Al/SiN_x hydrogenation and spatial match of strongest down-grade lifetime effect and R-parameter peaks indicated by arrows. Subsequent 700 °C de-hydrogenation reveals that the increase in R-parameter or the PL defect concentration is caused by hydrogen out-diffusion. This

line-scan experiment is statistically in agreement with the behavior over entire EFG wafer area as illustrated in Table 2-1.

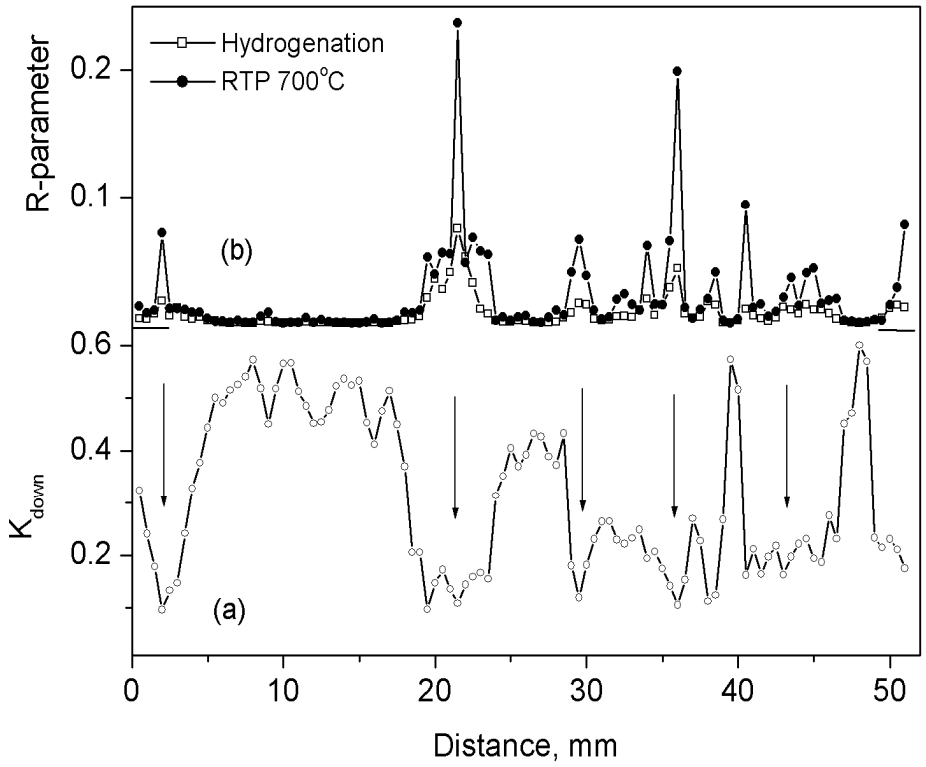

Figure 2-3. Lines scans of (a) down-grade coefficient after de-hydrogenation cased by 700 °C RTP; and (b) R-parameter after RTP-Al hydrogenation (open circles) and after 700 °C de-hydrogenation (closed circles).

2.4 Conclusions

In conclusions, scanning spectroscopic PL experiments on hydrogenated and de-hydrogenated EFG mc-Si wafers identified that the major effect of the RTP-Al/SiN_x anneal process consists of hydrogen incorporation into the regions with high recombination activity of defects involving contaminated dislocations. Hydrogenation passivates radiative and non-radiative dislocation defects in the low lifetime regions, improving the local minority carrier lifetime, which benefits the solar cell efficiency.

2.5 References

[2-1] S. Narasimha and A. Rohatgi, IEEE Trans. Electron Devices **45**, 1776 (1998)
[2-2] A. Rohatgi, D. S. Kim, K. Nakayashiki, V. Yelundur, and B. Rounsaville, Appl. Phys. Lett. **84**, 145 (2004).
[2-3] V. Yelundur, A. Rohatgi, A. Ebong, A. M. Gabor, J. I. Hanoka, and R. L. Wallace, J. Electron. Mater. **30**, 526 (2001).
[2-4] S.Ostapenko, I.Tarasov, J.P.Kalejs, et al, Semicond. Sci. Technol. 15 (2000) pp.840-848.
[2-5] V. Alex, S. Finkbeiner, J. Weber, J. Appl. Phys. **79** (1996), 6943.
[2-6] S. Ostapenko, M. Romero European Physical Journal: Applied Physics (2004), in press.
[2-7] I.Tarasov, S.Ostapenko, V. Feifer et al, Physica B, 273-274 (1999), pp.549-552
[2-8] K.Nakayashihi, D.S.Kim, A.Rohatgi, B.R.Bathey, Technical Digest of 14th International Photovoltaics Science and Engineering Conference, Bangkok, Thailand, 2004 p. 643.

3. Effect of Material Inhomogeneity on the Open-Circuit Voltage of String Ribbon Si Solar Cells

3.1 Introduction

The cost of photovoltaic (PV) systems needs to decrease by a factor of 2-4 to compete with traditional energy sources. Cast and ribbon multicrystalline Si (mc-Si) are promising low-cost materials for cost-effective PV systems. Since the Si substrate accounts for about 40% of the total cost of crystalline Si PV modules [3-1], the use of cheaper mc-Si materials without appreciable loss in efficiency should help in cost reduction. In general, mc-Si materials are cheaper than monocrystalline Si because of the simpler and less expensive crystal growth technique and equipment. The ribbon mc-Si growth techniques offer an additional cost benefit by eliminating the kerf loss associated with the mechanical sawing process and subsequent deep chemical etching used for saw damage removal [3-2],[3-3].

Table 3-1 Characteristics of PV-grade Si materials [3-2].

Material	Thickness (μm)	Resistivity (Ω-cm)	Carbon (cm^{-3})	Oxygen (cm^{-3})	Dislocations (cm^{-2})
Czochralski	200~400	1 – 3	$0.5\sim2.5\times10^{17}$	$0.1\sim2.0\times10^{18}$	500
Directional solidification	300	0.8 – 1.5	$<5.0\times10^{17}$	$<2.5\times10^{17}$	1.0×10^{5}
EFG	300	1 – 3	10^{18}	$2.4\sim4.0\times10^{17}$	$<1.0\times10^{6}$
String Ribbon	300	1 – 3	4.0×10^{17}	$<5.0\times10^{16}$	5.0×10^{5}

Table 3-1 lists important characteristics of these mc-Si materials along with the PV-grade monocrystalline Czochralski Si [3-2]. Unlike monocrystalline Si, cast and ribbon mc-Si suffer from high concentrations of impurities and crystallographic defects that are distributed inhomogeneously [3-2],[3-3]. These defects lead to relatively low as-grown carrier lifetimes, typically <30 μs in cast mc-Si wafer and <5 μs in ribbon Si, such as edge-defined film-fed growth and String Ribbon Si [3-4]. These minority carrier lifetime values are not sufficient to produce high-efficiency screen-printed Si solar cells. Therefore, it is necessary to enhance the carrier lifetime during the solar cell fabrication process in order to achieve high-efficiency and cost-effective screen-printed Si solar cells. P diffusion-induced impurity gettering and the SiN_x-induced hydrogen passivation of defects are routinely used as part of the solar cell fabrication sequence to enhance the carrier lifetime in these defective Si materials [3-4]-[3-9].

Inhomogeneously distributed electrically active defects are frequently found to be present in the mc-Si materials, even after effective P diffusion gettering and the SiN_x-induced hydrogen passivation of defects. Therefore, understanding and assessing the impact of the inhomogeneous distribution of defects on solar cell performance has become an area of active investigation. For example, Sopori [3-10] made an attempt to quantify the influence of material inhomogeneities on solar cell performance by developing a methodology and technique to extract an effective minority carrier diffusion length (L_{eff}) from the lateral and vertical distribution of defects to assess their impact on open-circuit voltage (V_{OC}). Mijnarends et al. [3-11] performed numerical simulations to investigate the lateral variations in material quality on solar cell characteristics and found that the wider distribution of diffusion length is detrimental to cell performance. In [12], a practical investigation was performed by fabricating multiple mini solar cells (0.9 x 0.9 mm^2) to examine V_{OC} across the mc-Si wafer. A strong correlation between local V_{OC} and minority carrier diffusion length was confirmed in these mini solar cells. It was concluded that a narrow distribution of diffusion length is desirable. Bell et al. [3-13] concluded that material inhomogeneities can significantly limit the voltage output, and grains with the low carrier lifetime determine the V_{OC} of mc-Si cells. Warta et al. [3-14] pointed out the limitations of the 1D simulation tools for predicting the performance of a mc-Si solar cell with a defective crystal structure. A diode network model was proposed and applied to compare the simulated and measured mc-Si solar cell performance. Nagel et al. [3-15] used the diode network model developed in [3-14] to simulate the solar cell performance parameters on the basis of lifetime mapping on commercial cast material, neglecting the surface recombination and metal contact effects. In [3-16], the diode network model was also used to demonstrate that a 20% defective region can lead to a 30 mV reduction in V_{OC}. Donolato [3-17] applied the Voronoi network model to mc-Si with columnar grains and showed that the grains with low carrier lifetime are responsible for the reduction in V_{OC}. Isenberg et al. [3-18] showed by 2D DESSIS simulation that the network model is not applicable if the lateral size of defective structures is smaller than the thickness or diffusion length in good regions.

In this section, an effort is made to improve the experimental and theoretical understanding of the impact of spatial distribution of defect inhomogeneities on fully processed high-performance screen-printed ribbon mc-Si solar cells. Since ribbon Si materials generally have an as-grown carrier lifetime below 5 μs, an attempt is made to enhance the gettering and passivation techniques to raise the average carrier lifetime above 90 μs in order to increase the sensitivity and the impact of low diffusion length regions (bad regions). Several 4 cm^2 screen-printed String Ribbon Si solar cells are fabricated and a simple methodology is developed to approximately determine the loss in V_{OC} in these cells resulting from a small fraction of bad region mixed with a large fraction of good region. Model calculations are performed by developing and using simple and approximate analytical expressions to assess the impact of recombination intensity and area fraction of bad regions on V_{OC}. Model calculations are compared with the experimental data to demonstrate that loss in V_{OC} resulting from material inhomogeneity can be predicted with reasonable accuracy by dividing the cell into two regions (best and worst) and using this simple analytical model.

3.2 Experiment

In this study, 300 μm thick, p-type 3-4 Ωcm String Ribbon Si material from Evergreen Solar (Marlboro, MA) was used. After the initial cleaning process, the wafers were P diffused in a $POCl_3$ furnace to form 40-50 Ω/sq n^+ emitters. A SiN_x anti-reflection coating with a thickness of 800 Å and a refractive index of 2.0 was deposited in a low-frequency plasma-enhanced chemical vapor deposition (PECVD) reactor. A commercial Al paste was then screen printed on the entire back surface and an Ag grid was screen printed on the front, followed by an anneal in a rapid thermal processing (RTP) system to (i) form an Al-doped back surface field (Al-BSF) on the rear surface, (ii) form a screen-printed Ag ohmic contact on the front surface, and (iii) promote the SiN_x-induced hydrogen passivation of defects. Several 4 cm^2 solar cells were fabricated on each wafer and isolated using a dicing saw, followed by a forming gas anneal at 400 °C for 10 min. The solar cell parameters were extracted by illuminated and dark current-voltage (I-V) measurements. The light beam-induced current (LBIC) scans were performed on selected solar cells to map the spatial non-uniformity of photoresponsivity using the PVSCAN5000 system [3-19] equipped with a 980 nm laser. Several regions on each solar cell were then selected to perform local light-biased internal quantum efficiency (IQE) measurements to quantify the difference in material quality in those regions in terms of L_{eff}, which includes bulk and surface effects.

3.3 Results and Discussion

3.3.1 LBIC Scans and IQE Measurements

The LBIC scan was performed on each cell to detect the material inhomogeneity and measure the recombination intensity of electrically active defects. Since several 4 cm^2 solar cells were fabricated on each large-area String Ribbon Si wafer, we selected the wafer containing cells with high, moderate, and low V_{OC} to conduct our study and evaluate the impact of inhomogeneously distributed electrically active defects on V_{OC}. Fig. 3-1 shows the LBIC maps of three String Ribbon Si solar cells on the same wafer with high, moderate, and low V_{OC}. These cells were selected because they also showed maximum contrast between defective and defect-free regions. Table 3-2 shows the performance parameters of these three String Ribbon Si solar cells. The LBIC maps in Fig. 3-1 show that cell 1 has relatively uniform current collection over the entire cell area, compared to the other two, with little or no detectable bad regions. This is also reflected in the high area-averaged LBIC response of 0.568 A/W along with a high V_{OC} of 616 mV and a cell efficiency of 15.9%. Cells 2 and 3 had a much lower V_{OC} of 592 and 578 mV with cell efficiencies of 15.0% and 14.1% and corresponding area-averaged LBIC response of 0.504 and 0.454 A/W, respectively (Table 3-2).

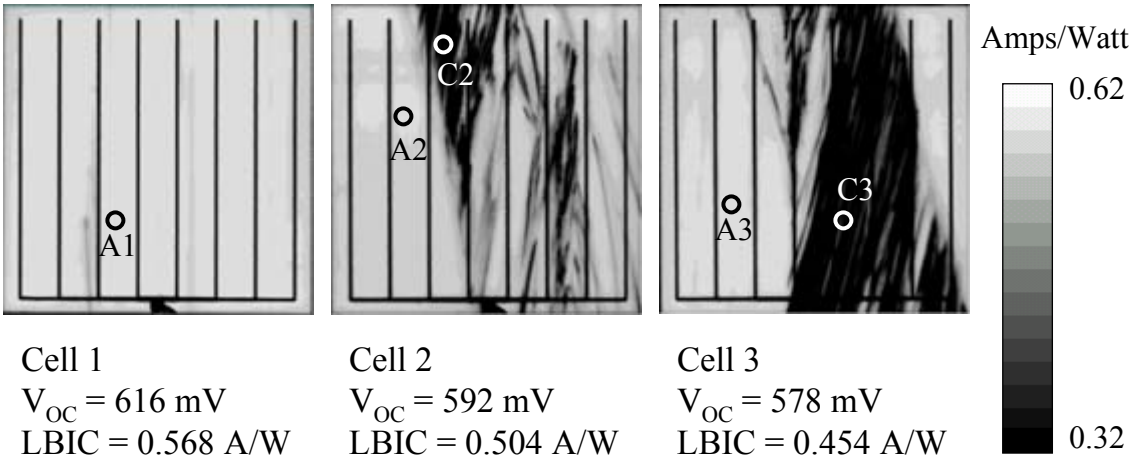

Fig. 3-1. LBIC maps of String Ribbon Si solar cells. High, moderate, and low V_{OC} cells are shown in left, center, and right sides, respectively.

Table 3-2 Measured String Ribbon Si solar cell parameters and LBIC responses.

Cell ID	V_{OC} (mV)	J_{SC} (mA/cm^2)	FF	Eff. (%)	LBIC (A/W)
1	616	33.5	0.773	15.9	0.568
2	592	32.7	0.774	15.0	0.504
3	578	31.4	0.778	14.1	0.454

After the illuminated I-V measurements and LBIC scans, light-biased IQE measurements were taken in selected areas of these String Ribbon Si solar cells, indicated by the circles in Fig. 3-1. Circles drawn are for visual aid and larger than the actual spot size (~1 mm in diameter) used for the IQE measurements. The circled regions A1, A2, and A3 on cells 1, 2, and 3, respectively, were selected based on the LBIC maps because they had the highest and nearly equal LBIC responses. These represent the best regions on the three cells. On the other hand, regions C2 and C3 on cells 2 and 3, respectively, gave the poorest LBIC response, indicating that these regions are the most defective regions on the cell. Fig. 3-2 shows the light-biased IQE response of all five regions (A1, A2, A3, C2, and C3). As expected, regions C2 and C3 showed a significant degradation in the IQE response in the long-wavelength range (>650 nm) relative to regions A1, A2, and A3. The IQE response in the long-wavelength range is indicative of the combined effect of carrier lifetime and back surface recombination velocity (BSRV) for 300 μm thick Si cells [3-20]. Consistent with

the LBIC response, there was no appreciable difference in the IQE response of regions A1, A2, and A3 in the long-wavelength range, supporting the fact that the best regions on the three solar cells (1, 2, and 3) are nearly identical, despite the significant difference in V_{OC} and defect inhomogeneity.

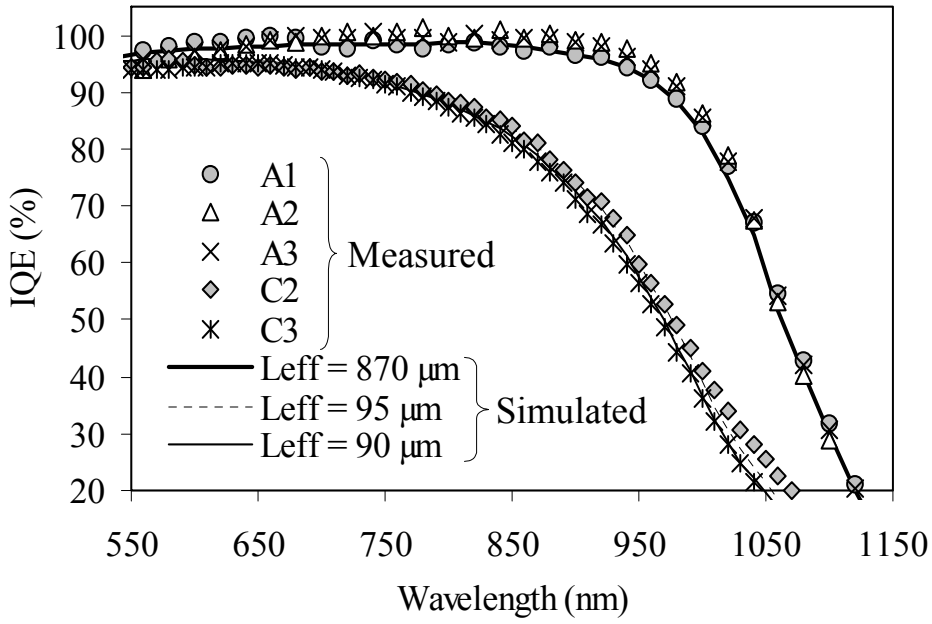

Fig. 3-2. Light-biased IQE response of selected regions (A1, A2, A3, C2, and C3) in String Ribbon Si solar cells and simulated (PC1D) IQE response corresponding to L_{eff} values of 870, 95, and 90 μm.

3.4 Extraction of Effective Diffusion Length L_{eff} from the IQE Response

V_{OC} is a strong function of recombination in the emitter, base, and at the surfaces. According to theory, the V_{OC} can be expressed as follows [3-21]:

$$V_{OC} = \frac{kT}{q} \cdot \ln\left(\frac{J_{SC}}{J_{oe} + J_{ob}} + 1\right), \tag{3-1}$$

where k is the Boltzmann constant, T is the temperature, J_{SC} is the short-circuit current density, J_{ob} is the base components of saturation current density, and J_{oe} is the emitter component of saturation current density. Since the three solar cells were selected from the same wafer, they should have identical emitters, and their J_{oe}, which is a function of emitter doping profile and surface recombination velocity, can be assumed to be identical.

Thus, the J_{oe}, which is a function of carrier lifetime and BSRV, must account for the majority of the difference in V_{OC}. The J_{ob} is expressed as follows [3-22]:

$$J_{\mathrm{ob}} = \frac{q n_i^2 D_n}{N_B L_{\mathrm{eff}}}, \tag{3-2}$$

where q is the electron charge, n_i is the intrinsic carrier concentration, D_n is the diffusion coefficient of electron, and N_B is the background doping concentration. The effective minority carrier diffusion length, L_{eff}, is defined as

$$L_{\mathrm{eff}} = L_b\left(\frac{1 + \frac{SL_b}{D_n}\tanh\frac{W}{L_b}}{\frac{SL_b}{D_n} + \tanh\frac{W}{L_b}}\right), \tag{3-3}$$

where S represents the BSRV, Lb ($=\sqrt{D_n \tau_b}$) is the bulk minority carrier diffusion length, τb is the bulk carrier lifetime, and W is the cell thickness. According to Eq. (3-3), L_{eff} is primarily a function of bulk and surface recombination for the fixed resistivity and thickness.

The L_{eff} value in any region of a solar cell can be extracted by matching the measured and simulated local area IQE response in the long-wavelength range (700-920 nm for 300 μm thick cells) using the PC1D simulation program [3-23]. This was done by determining and/or using the realistic inputs for the PC1D simulations. For example, front surface recombination velocity (FSRV) was extracted from the measured IQE response in the short-wavelength range [3-24]. Front doping was determined by the spreading resistance measurement. Base contact (or series resistance) and internal conductor (or shunt resistance) values were obtained from illuminated I-V measurements. The internal diode or junction leakage current J_{o2} value was extracted from the dark I-V measurement, assuming the second diode ideality factor of 2.0. Uniform distribution of D_n was assumed during the L_{eff} extraction using PC1D. Sontag et al. [3-25] reported a factor of two lower D_n value in ribbon Si material compared to monocrystalline Si material. The IQE response in long-wavelength range represents the correct value of L_{eff}, which is composed of L_b and BSRV, regardless of the D_n and τ_b values. Figure 3-2 also shows the match between the measured and simulated IQE response from all five regions, resulting in an L_{eff} of ~870 μm for regions A1, A2, and A3, ~95 μm for region C2, and ~90 μm for region C3. This was done by fixing the BSRV at 250 cm/s and varying the L_b (or τ_b) in PC1D until a good match in the long-wavelength range was achieved. BSRV and L_b were then used to obtain L_{eff} from Eq. (3-3). Note that these BSRV and L_b values do not necessarily represent the true BSRV and L_b values, but they still give the correct value of L_{eff}. This is because the L_{eff} is a function of both L_b (or τ_b) and BSRV [Eq. (3-3)]. This was validated by choosing different values of BSRV and performing the same procedure on IQE. As expected, different combinations of L_b and BSRV led to the same L_{eff} value.

Table 3-3 PC1D input parameters for String Ribbon Si solar cell simulation.

Device Parameter	**Input**
Base resistivity	3.0 Ωcm
Thickness	300 μm
FSRV	150,000 cm/s
Broadband reflectance	6.0%
Front surface coating	78 nm, index = 2.0
Rear internal reflectance	55%, diffuse
Front doping	Spreading resistance measurement
Base contact (Series resistance)	0.75 Ω ($0.75\ \Omega cm^2$)
Internal conductor (Shunt resistance)	5.0×10^{-5} S ($2.0\times10^{4}\ \Omega cm^2$)
J_{o2}	2.6×10^{-8} A

The L_{eff} value of 870 μm in region A1, in conjunction with the PC1D inputs in Table 3-3, was used to obtain the simulated solar cell I-V parameters, which agreed very well with the measured parameters of cell 1 (Table 3-4), which was nearly uniform. However, there was a significant difference between the measured solar cell parameters of the defective or poor solar cell 3 (Table 3-4) and the simulated cell parameters when a L_{eff} of 870 μm was used for the entire cell. Table 3-4 shows that there is a difference of 37 mV in V_{OC}. This difference is largely attributed to the existence of electrically active defects.

Table 3-4 Measured and simulated solar cell parameters on String Ribbon Si using extracted L_{eff} of 870 μm.

Cell ID	**V_{OC} (mV)**	**J_{SC} (mA/cm^2)**	**Eff. (%)**
Simulated	615	33.6	15.9
1	616	33.5	15.9
3	578	31.4	14.1

The next section shows the development of a simple analytical model to calculate the loss in V_{OC} from the area fraction and intensity of the recombination of the electrically active defects. The simulated results are then compared with the experimental data in Table 3-4.

3.5 Theoretical and Experimental Assessment of the Impact of Electrically Active Defects on Solar Cell Performance

3.5.1 Development of the Analytical Model to Assess the Loss in V_{OC} Resulting from Inhomogeneity

The non-uniform distribution of defects, such as grain boundaries, impurities, and dislocations, is common in mc-Si materials. Many of these defects act as localized carrier recombination centers resulting in spatial variation in L_{eff}.

The first step was to develop a simple and approximate analytical model for the quantitative assessment of the effect of distributed L_{eff} on V_{OC}. A mc-Si solar cell is essentially composed of a number of small solar cells (good and bad regions) in parallel, operating at a constant potential across the junction as a result of the electrical connection through grid, emitter, and substrate [3-26]. The total cell current, I, can be expressed as the summation of currents from local area cells:

$$I = I_1 + I_2 + \cdots + I_i. \tag{3-4}$$

Assuming the two-diode model, Eq. (3-4) can be expressed as

$$\begin{aligned} I_{o1}\exp(\frac{qV}{kT}-1) + I_{o2}\exp(\frac{qV}{n_2kT}-1) \;=\; & \{I_{o1,1}\exp(\frac{qV}{kT}-1) + I_{o2,1}\exp(\frac{qV}{n_2kT}-1)\} \\ & + \{I_{o1,2}\exp(\frac{qV}{kT}-1) + I_{o2,2}\exp(\frac{qV}{n_2kT}-1)\} \\ & + \cdots + \{I_{o1,i}\exp(\frac{qV}{kT}-1) + I_{o2,i}\exp(\frac{qV}{n_2kT}-1)\}, \end{aligned} \tag{3-5}$$

where V is the junction potential, I_{o1} and I_{o2} are the dark saturation current and the junction leakage current, respectively, and n_2 is the second diode ideality factor [3-27]. Since the I_{o2} component generally has a much smaller contribution to total current at V_{OC} compared to I_{o1} component, Eq. (3-5) can be expressed as

$$I_{o1} = I_{o1,1} + I_{o1,2} + \cdots + I_{o1,i}. \tag{3-6}$$

Since I_{o1} is composed of I_{oe} and I_{ob}, and I_{oe} can be independent of the defective region because carrier lifetime in the emitter region is generally dictated by the Auger recombination. Equation (6) can now be expressed as

$$I_{ob} = I_{ob,1} + I_{ob,2} + \cdots + I_{ob,i}, \tag{3-7}$$

$$a \cdot J_{ob,avg} = a_1 \cdot J_{ob,1} + a_2 \cdot J_{ob,2} + \cdots + a_i \cdot J_{ob,i}, \tag{3-8}$$

$$J_{ob,avg} = A_1 \cdot J_{ob,1} + A_2 \cdot J_{ob,2} + \cdots + A_i \cdot J_{ob,i}, \tag{3-9}$$

where $J_{ob,avg}$ is the area-weighted average of J_{ob}, a is the actual area, and A_i is the area fraction (a_i/a) of each region. Since J_{ob} is inversely proportional to the L_{eff} [Eq. (3-2)], Eq. (3-9) can be written as

$$L_{\text{eff,avg}}^{-1} = A_1 \cdot L_{\text{eff,1}}^{-1} + A_2 \cdot L_{\text{eff,2}}^{-1} + \cdots + A_i \cdot L_{\text{eff,i}}^{-1}. \tag{3-10}$$

The area-weighted average value of L_{eff} ($L_{eff,avg}$) can now be expressed as

$$L_{\text{eff,avg}}^{-1} = \sum_{i=1}^{n} (L_{\text{eff,i}}^{-1} \times A_i). \tag{3-11}$$

The effective J_{ob} ($J_{ob,eff}$) can now be determined by Eq. (3-2) using the $L_{eff,avg}$. Finally, the $J_{ob,eff}$ can be used as follows to obtain the V_{OC}.

$$\begin{aligned} V_{\text{OC}} &= \frac{kT}{q} \ln\left(\frac{J_{\text{SC}}}{J_{\text{o}}} + 1\right) \\ &= \frac{kT}{q} \ln\left(\frac{J_{\text{SC}}}{J_{\text{ob,eff}} + J_{\text{oe}}} + 1\right) \\ &\simeq \frac{kT}{q} \ln\left(\frac{J_{\text{SC}}}{J_{\text{ob,eff}}} + 1\right), \end{aligned} \tag{3-12}$$

where

$$J_{\text{ob,eff}} = \frac{q n_i^2 D_n}{N_B L_{\text{eff,avg}}}. \tag{3-13}$$

Note that Eq. (3-12) ignores the effect of J_{oe}, which is the case for these relatively low V_{OC} (<620 mV) solar cells where base quality dominates the V_{OC}. To support this assumption, J_{oe} was measured on high-resistivity (500-1000 Ωcm) n-type FZ Si using a photoconductance decay technique after double-sided P diffusion, SiN_x deposition, and firing in an RTP unit without the metallization. The measured J_{oe} of 187 fA/cm^2, without metallization, corresponds to a V_{OC} of 671 mV (assuming J_{SC} of 33.5 mA/cm^2), which is much higher than the measured V_{OC} of these cells. The presence of a front grid is expected to lower the emitter-limited value of V_{OC} somewhat, but it will still be much higher than the actual V_{OC} of these cells.

The loss in V_{OC} can now be calculated using the following analytical expression:

$$
\begin{aligned}
\Delta V_{\mathrm{OC}} &= V_{\mathrm{OC(defect\text{-}free)}} - V_{\mathrm{OC(defective)}} \\
&= \frac{kT}{q}[\ln(\frac{J_{\mathrm{SC,high}}}{J_{\mathrm{ob,high}}}+1) - \ln(\frac{J_{\mathrm{SC,avg}}}{J_{\mathrm{ob,eff}}}+1)] \\
&\simeq \frac{kT}{q}[\ln(\frac{J_{\mathrm{SC,high}}}{J_{\mathrm{ob,high}}}) - \ln(\frac{J_{\mathrm{SC,avg}}}{J_{\mathrm{ob,eff}}})] \\
&= \frac{kT}{q}\ln(\frac{J_{\mathrm{SC,high}}}{J_{\mathrm{SC,avg}}}\cdot\frac{J_{\mathrm{ob,eff}}}{J_{\mathrm{ob,high}}}) \\
&= \frac{kT}{q}\ln(\frac{J_{\mathrm{SC,high}}}{J_{\mathrm{SC,avg}}}\cdot\frac{L_{\mathrm{eff,high}}}{L_{\mathrm{eff,avg}}}),
\end{aligned}
\tag{3-14}
$$

where $V_{OC\ (defect\text{-}free)}$ corresponds to the V_{OC} value in the absence of localized bad regions with uniformly distributed high L_{eff} value ($L_{eff,high}$=870 μm in this study). $V_{OC(defective)}$ corresponds to $L_{eff,avg}$ and includes the combined effect of bad regions. The $J_{SC,high}$ and $J_{SC,avg}$ values, corresponding to $L_{eff,high}$ and $L_{eff,avg}$ were obtained from PC1D simulations by fixing the BSRV to the same value (250 cm/s) and adjusting the carrier lifetime to obtain the desired L_{eff} for PC1D simulation. Note that the choice of BSRV does not alter the PC1D output or J_{SC} significantly as long as the L_{eff} is the same.

3.5.2 Model Calculations to Assess the Loss in V_{OC} of a Cell With Two Regions of Different Recombination Intensity

Model calculations were performed using Eqs. (3-11), (3-13), and (3-14) to quantify the impact of inhomogeneous material quality on the V_{OC} of a cell by first dividing it into two regions (good and bad). The $L_{eff,high}$ for the good region was fixed at 870 μm (L_{eff} = 3 times cell thickness W), the $L_{eff,low}$ for bad region was varied, and the ratio of $L_{eff,low}/L_{eff,high}$ was used as a measure of the recombination intensity in the bad region. This ratio represents the recombination activity in bad region, and it increases with the increase in $L_{eff,low}$. The $L_{eff,low}$ values of 44, 87, 174, and 435 μm were selected for model calculation, corresponding to recombination intensities ($L_{eff,low}/L_{eff,high}$) of 0.05, 0.1, 0.2, and 0.5, respectively. To generate model curves, the area fraction of the bad region was varied from 0 to 50% for each recombination intensity and Eqs. (3-11), (3-13), and (3-14) were used in sequence to calculate $L_{eff,avg}$, $J_{ob,eff}$, and ΔV_{OC}. $J_{SC,high}$ and $J_{SC,avg}$ were calculated from PC1D using $L_{eff,high}$ and $L_{eff,avg}$ as inputs. All other inputs (Table 3-3) were kept the same. Figure 3-3 shows the results of analytical model calculations. It shows that 10% of the defective area with a recombination intensity of 0.05 can reduce V_{OC} by 28 mV of a device that is capable of producing V_{OC} of 623 mV, which was obtained from Eqs. (3-12) and (3-13) using $L_{eff,avg}$ of 870 μm and J_{SC} of 33.5 mA/cm^2. Figure 3-3 also shows that we need to get below a 5% area fraction with a recombination intensity of 0.5 to avoid any appreciable loss in V_{OC}. To determine the error associated with neglecting J_{oe}, the V_{OC} values were also calculated with J_{oe} of 187 fA/cm^2 using the following equation:

$$\Delta V_{OC} = \frac{kT}{q}[\ln(\frac{J_{SC,high}}{J_{ob,high} + J_{oe}} + 1) - \ln(\frac{J_{SC,avg}}{J_{ob,eff} + J_{oe}} + 1)]. \quad (3\text{-}15)$$

The error was found to be ±3 mV in this model calculation.

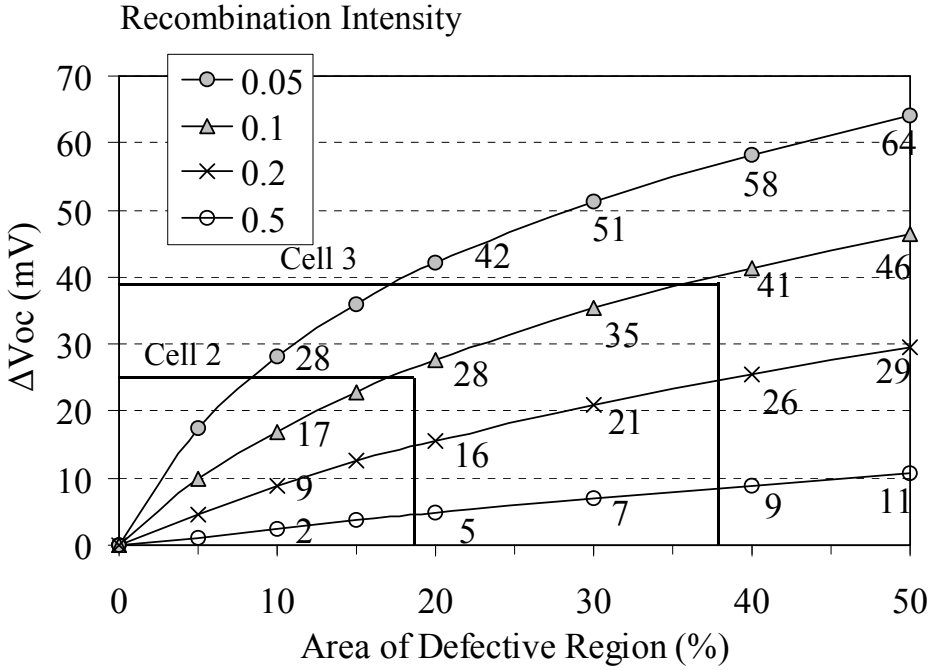

Fig. 3-3. Calculated loss in V_{OC} as a function of defective area with different L_{eff} ratio or recombination intensity. Cell was divided into two regions (good and bad). Base resistivity was assumed to be 3.0 Ωcm.

3.5.3 Model Calculations to Assess the Loss in V_{OC} of a Cell With Three Regions of Different Recombination Intensity

To estimate the error associated with dividing the cell into just two regions, rather than multiple regions, model calculations were performed to include a third region, referred to as the moderate region. In this calculation, the area fractions of all three regions (good, moderate, and bad) were varied. Each curve was obtained by fixing the area fraction of the bad region first and then varying the area fraction of the moderate region from 0% to 50%. The L_{eff} of the good and bad regions were kept at 870 µm and 95 µm. The L_{eff} in the moderate region was fixed at 400 µm and calculations were performed using Eqs. (3-11), (3-13), and (3-14) in sequence to obtain $L_{eff,avg}$, $J_{ob,avg}$, and ΔV_{OC}. The modeling results in Fig. 4 reveal that the bad region has the biggest influence on the loss in V_{OC} (17 mV) even when its area fraction is 10%. This is because, as the moderate area fraction increases from

0% to 50%, for the 10% bad area fraction, the loss in V_{OC} increases from 17 mV to only 24 mV. Figure 3-4 also shows that if the bad area fraction approaches or exceeds 40%, then it essentially dominates the loss in V_{OC}, which reaches ~40 mV in this example. Thus, an approximate analysis using the best and the worst regions can give a reasonable idea of the loss in V_{OC} resulting from the inhomogeneous distribution of electrically active defects. One can choose more than two or three regions for better accuracy using the same methodology. For a more exact analysis, point-by-point LBIC and IQE maps are needed over the entire cell area to calculate $L_{eff,avg}$ and $J_{ob,eff}$.

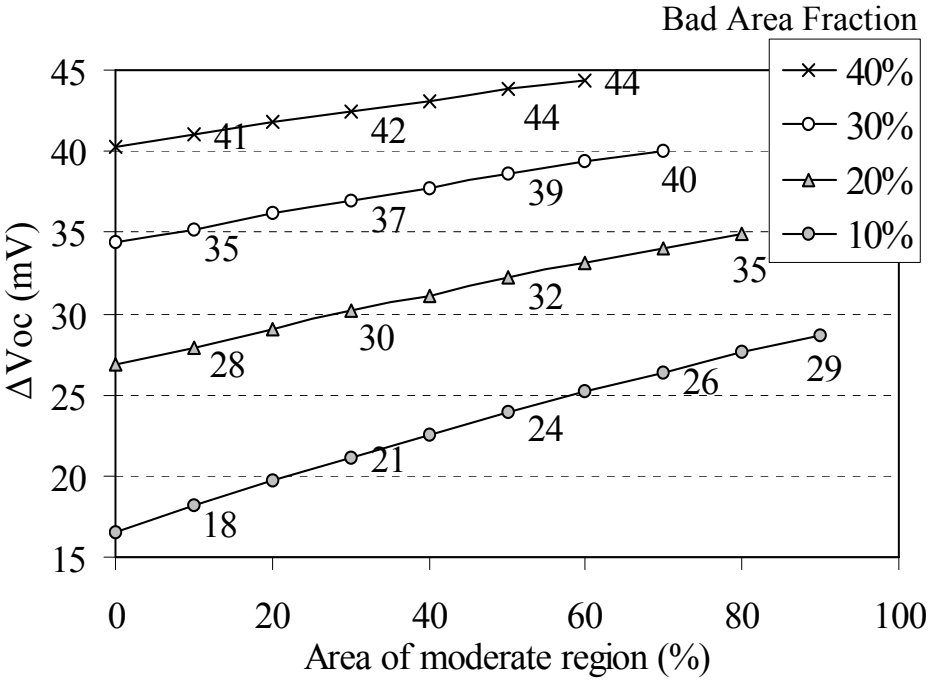

Fig. 3-4. Calculated loss in V_{OC} for each area fraction of defective region as a function of area fraction of moderate region. Base resistivity was assumed to be 3.0 Ωcm.

3.5.4 Application of the Analytical Model to Defective Cells

A statistical analysis of LBIC maps in Fig. 3-5 was used to assess the area fraction of defective regions. The LBIC output gives a map or range of spectral responses in A/W, which was divided into 16 equal size bins. Figure 3-5 shows the resulting histograms of the LBIC response for the three cells. Next, each cell was divided into two regions: good region with a spectral response ranging from 0.48 to 0.62 A/W and bad region with a spectral response ranging from 0.32 to 0.46 A/W. The area fraction of the two regions was determined by

$$A_i = \frac{\sum_{i=1}^{N} B_i}{\sum_{i=1}^{K} B_i}, \tag{3-16}$$

where B_i is the count in the i bin, N is the number of bins in that region (e.g., 0.32-0.46 A/W for region 2), and K is the total number of bins (=16 in this study). This analysis gave the area fractions of 0.02, 0.19, and 0.38 associated with the bad regions for cells 1, 2, and 3, respectively. Note that the grid coverage (6% of cell area) was removed from the histogram in Fig. 5 since there is no carrier generation below the grid. It is important to note that the same procedure can be used to divide the LBIC output into multiple regions instead of just two.

Recall that the light-biased IQE response in Fig. 3-2 showed a significant degradation in the long-wavelength IQE response of regions C2 and C3, relative to regions A2 and A3, and the measured and simulated IQE match gave L_{eff} values of 95 μm and 90 μm for regions C2 and C3, respectively, as opposed to 870 μm for regions A2 and A3. According to Eq. (3-2), this results in significantly higher J_{ob} values of 10-12 to 10-13 A/cm^2 in regions C2 and C3 relative to the good regions A2 and A3 where J of 10-14 A/cm^2 is obtained.

Using Eq. (3-11) and a $L_{eff,high}$ of 870 μm and $L_{eff,low}$ of 95 μm with an area fraction of 81% and 19% for the good and bad regions for cell 2 gives a $L_{eff,avg}$ value of 342 μm. Using the L_{eff} values of 870 and 342 μm along with the PC1D inputs in Table 3-3, J_{SC} values of 33.6 mA/cm^2 ($J_{SC,high}$) and 32.6 mA/cm^2 ($J_{SC,avg}$) are obtained from the PC1D simulations. Note that these J_{SC} values are in good agreement with the measured values of

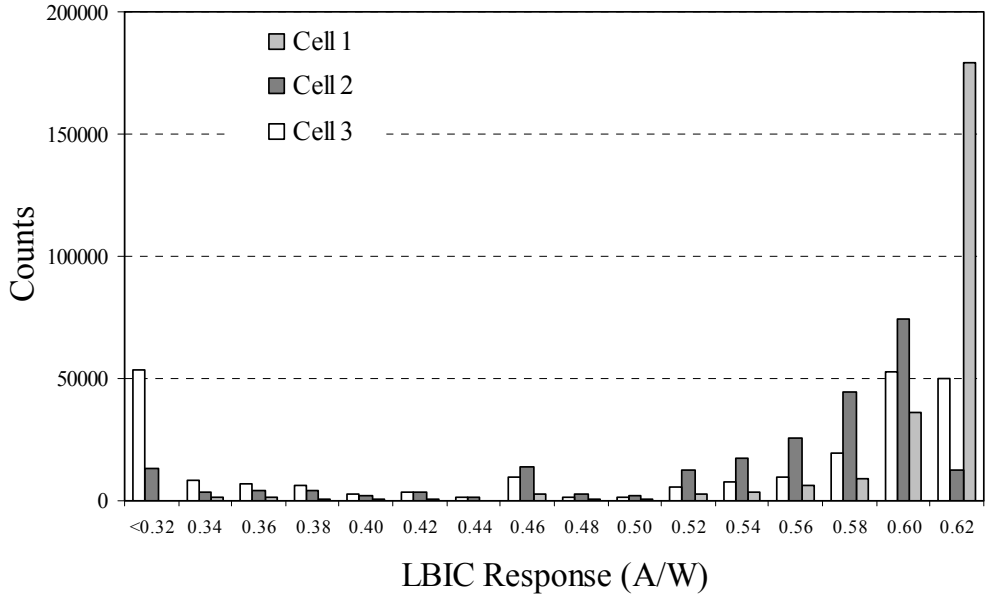

Fig. 3-5. Histograms of LBIC response shown in Fig. 1. The Ag grid coverage effect (6.0% of cell area) was removed from <0.32 A/W bin. Maximum LBIC response was 0.62 A/W for all three cells.

33.5 mA/cm^2 and 32.7 mA/cm^2 for cell 1 and 2, respectively (Table II). Finally, using these J_{SC} and L_{eff} values in Eq. (14) gives a ΔV_{OC} of 25 mV, which is in good agreement with the measured V_{OC} difference of 24 mV between cell 1 and 2 (Table 3-2).

Cell 3 was also analyzed using the same methodology described above. An $L_{eff,high}$ of 870 μm and $L_{eff,low}$ of 90 μm with a good and bad area fraction of 62% and 38% for cell 3 gave a $L_{eff,avg}$ value of 203 μm, which resulted in a $J_{SC,avg}$ value of 31.6 mA/cm^2 from the PC1D simulation. Note that this J_{SC} value is in good agreement with the measured value of 31.4 mA/cm^2 for cell 3 (Table 3-2). Equation (3-14) gave a ΔV_{OC} of 39 mV, which is again in good agreement with the measured V_{OC} difference of 38 mV between cells 1 and 3 (Table II). Cells 2 and 3 are mapped in Fig. 3-3 to show the agreement between cell data and model calculations. Even though the model and the procedure outlined above are valid for multiple-region analysis, a simple two-region analytical model gave a fairly good idea of the loss in V_{OC} resulting from the material inhomogeneity in these high-performance screen-printed mc-Si solar cells.

3.6 Conclusions

The effect of electrically active defects on V_{OC} was quantified and evaluated through a simple and approximate analytical model. Model calculations were performed to reveal the relationship between the area fraction, recombination intensity of defective region, and the loss in V_{OC}. In this study, three String Ribbon Si solar cells were used to test this model and understand the impact of defect inhomogeneity. A two-region analysis using the model developed in this study gave a reasonable estimate of the loss in V_{OC} resulting from defect inhomogeneity. LBIC and IQE measurements were used to estimate the area fraction and recombination intensity of the defective regions. Model calculations showed that a cell with a 38% area fraction of bad region with a recombination intensity of 0.1 can reduce the V_{OC} by 39 mV. This agreed well with the experimental data for cell 3, which showed a loss in V_{OC} of 38 mV. There was also a good agreement between the experimental data and model calculations, which showed that a 19% area fraction of bad region with a recombination intensity of 0.11 can reduce the V_{OC} by 25 mV. Model calculations revealed that in order to keep the loss in V_{OC} below 5 mV in high-performance devices, the area fraction of the defective region should be below 20% with a recombination intensity of 0.5 or greater.

3.7 References

[3-1] United States Department of Energy, "Solar Photovoltaic," Feb. 2005, http://www.eia.doe.gov/cneaf/solar.renewables/page/solarphotv/solarpv.html

[3-2] R.O. Bell and J.P. Kalejs, "Growth of silicon sheets for photovoltaic applications," J. Mater. Res., vol. 13, pp. 2732-2739, Oct. 1998.

[3-3] J.I. Hanoka, "An overview of silicon ribbon growth technology," Sol. Energy Mater. Sol. Cells, vol. 65, pp. 231-237, Jan. 2001.

[3-4] J. Jeong, A. Rohatgi, M.D. Rosenblum and J.P. Kalejs, in Proc. 28th IEEE Photovoltaic Specialists Conference, 2000, pp. 83-86.

[3-5] J. Jeong, Y.H. Cho, A. Rohatgi, M.D. Rosenblum, B.R. Bathey and J.P. Kalejs, in Proc. 29th IEEE Photovoltaic Specialists Conference, 2002, pp. 250-253.

[3-6] F. Duerinckx and J. Szlufcik, "Defect passivation of industrial multicrystalline solar cells based on PECVD silicon nitride," Sol. Energy Mater. Sol. Cells, vol. 72, pp. 231-246, Apr. 2002.

[3-7] A. Rohatgi, V. Yelundur, J. Jeong, A. Ebong, M.D. Rosenblum, and J.I. Hanoka, "Fundamental understanding and implementation of Al-enhanced PECVD SiNx hydrogenation in silicon ribbons," Sol. Energy Mater. Sol. Cells, vol. 72, pp. 117-126, Oct. 2002.

[3-8] V. Yelundur, A. Rohatgi, A. Ebong, A.M. Gabor, J.I. Hanoka, and R.L.Wallace, "Al-enhanced PECVD SiNx induced hydrogen passivation in string ribbon silicon," J. Electron. Mater., vol. 30, pp. 526-531, May 2001.

[3-9] J. Jeong, M.D. Rosenblum, J.P. Kalejs, and A. Rohatgi, "Hydrogenation of defects in edge-defined film-fed grown aluminum-enhanced plasma enhanced chemical vapor deposited silicon nitride multicrystalline silicon," J. Appl. Phys., vol. 87, pp. 7551-7557, May 2000.

[3-10] B.L. Sopori, "Inhomogeneities in silicon solar cells and their influence on cell performance - an experimental study," in Proc. 14th IEEE Photovoltaic Specialists Conference, 1980, pp. 606-611.

[3-11] P.E. Mijnarends, G.J.M. Janssen, and W.C. Sinke, "The effect of material inhomogeneities on the characteristics of semicrystalline silicon solar cells: the second diode," Sol. Energy Mater. Sol. Cells, vol. 33, pp. 345-360, July 1994.

[3-12] R. Baldner, H. Lautenschlager, C. Schetter, R. Schindler, and W. Warta, "Open circuit voltage losses in multicrystalline silicon: an investigation by mini solar cells," in Proc. 25th IEEE Photovoltaic Specialists Conference, 1996, pp. 641-644.

[3-13] R.O. Bell, M. Prince, F.V. Wald, W. Schmidt, and K.D. Rasch, "A comparison of the behavior of solar silicon material in different production processes," Sol. Energy Mater. Sol. Cells, vol. 41/42, pp. 71-86, June 1996.

[3-14] W. Warta, J. Sutter, B.F. Wagner, and R. Schindler, "Impact of diffusion length distributions on the performance of mc-silicon solar cells," in Proc. 2nd World Conference on Photovoltaic Energy Conversion, 1998, pp. 1650-1653.

[3-15] H. Nagel, A.G. Aberle, and S. Narayanan, "Method for the evaluation of the influence of gettering and bulk passivation on non-uniform block-cast multicrystalline Si solar cells," Di_us. Defect Data B, Solid State Phenom., vol. 67-68, pp. 503-508, 1999.

[3-16] B.L. Sopori, W. Chen, J. Gee, and K. Jones, "On the performance limiting behavior of defect clusters in commercial silicon solar cells," in Proc. 2nd World Conference on Photovoltaic Energy Conversion, 1998, pp. 152-155.

[3-17] C. Donolato, "Voronoi network modelling of multicrystalline silicon solar cells," Semicond. Sci. Technol., vol. 15, pp. 15-23, Jan. 2000.

[3-18] J. Isenberg, J. Dicker, and W. Warta, "Analysis of the effect of diffusion length distributions on global solar cell parameters by simplified 2D modeling," in Proc. 17th European Photovoltaic Solar Energy Conference and Exhibition, 2001, pp. 1571-1574.

[3-19] K.F. Carr, N. Carison, P. Weitzmann, B.L. Sopori, C. Marshall, and L. Allen, "Characterization of silicon solar cells and substrates with the PVScan 5000," in AIP Conference Proc. of 13th NREL Photovoltaic Program Rev., 1996, pp. 553-557.

[3-20] V. Meemongkolkiat, M. Hilali, and A. Rohatgi, "Investigation of RTP and belt fired screen printed Al-BSF on textured and planar back surfaces of silicon solar cells," in Proc. 3rd World Conference on Photovoltaic Energy Conversion, 2003, pp. 1467-1470.

[3-21] M.A. Green, Solar Cells, Kensington: UNSW, 1986.

[3-22] P.A. Basore, "Extended spectral analysis of internal quantum efficiency," in Proc. 23rd IEEE Photovoltaic Specialists Conference, 1993, pp. 147-152.

[3-23] V. Meemongkolkiat, M. Hilali, K. Nakayashiki, and A. Rohatgi, "Process and material dependence of Al-BSF in crystalline Si solar cells," in Technical Digests of 14th International Photovoltaic Science and Engineering Conference, 2004, pp. 401-402.

[3-24] M.M. Hilali, A. Rohatgi, and S. Asher, "Development of screen-printed silicon solar cells with high fill factors on 100 /sq emitters," IEEE Trans. Electron Devices, vol. 51, pp. 948-955, June 2004.

[3-25] D. Sontag, G. Hahn, P. Geiger, P. Fath, and E. Bucher, "Two-dimensional resolution of minority carrier diffusion constants in different silicon materials," Sol. Energy Mater. Sol. Cells, vol. 72, pp. 533-539, 2002.

[3-26] R. Sinton, "Predicting multicrystalline solar cell efficiency from lifetime measured during cell fabrication," in Proc. 3rd World Conference on Photovoltaic Energy Conversion, 2003, pp. 1028-1031.

[3-27] S.M. Sze, Semiconductor Devices Physics and Technology, New York: John Wiley & Sons, 1985.

4. Resistivity and Lifetime Variation along Commercially Grown Ga- and B-Doped Czochralski Si Ingots and Its Effect on Light-Induced Degradation and Performance of Solar Cells

4.1 Introduction

It is well known that solar cells fabricated on conventional B-doped Czochralski (Cz) Si suffer from degradation caused by the illumination or injection of carriers [4-1,4-2]. It has also been established that this light-induced degradation (LID) effect results from the presence of B and O simultaneously in Si [4-3,4-4]. Therefore, the LID effect can be removed by eliminating either B or O from Si. Several alternatives have been suggested and attempted in the literature to avoid LID in Cz Si including the 1) use of alternative dopants such as P for n-type and Ga for p-type Cz Si [4-3,4-5,-6] 2) reduction of interstitial oxygen to an acceptable level by growing Magnetic Cz [5] Si 3) use of higher resistivity B-doped Cz [4-2,4-7] and 4) process optimization [4-4,4-8 - 4-13]. Doping the Si ingot with Ga has advantages over other methods as it provides complete elimination of LID without modifying the cell structure or processing equipment. However, there are some drawbacks associated with the implementation of Ga. First, use of Ga dopant gives rise to a complication of managing the silicon feedstock [4-14]. Most Cz Si manufacturers for solar cells application rely on externally supplied remelt or potscrap. As Ga-doped remelt is not available on the open market, this situation likely necessitates the recycling of internally produced remelt, subsidized with virgin Si. Relying on virgin suppliers is not a cost-effective option and creates a significant risk since the availability and, more importantly, the cost of virgin Si fluctuates greatly. The other basic drawback of using Ga as a dopant is the low segregation coefficient of Ga in Si (k=0.008). This results in a much wider variation in resistivity along the Ga-doped ingot. If the solar cell fabrication process cannot tolerate this wider resistivity distribution, a significant yield loss in the crystal growth process would result in a substantial cost addition. Many research groups have tried to investigate the solar cell performance as a function of resistivity or the position in the ingot [4-11,4-15,4-16]. However, such relationship has never been established for the widely manufactured screen-printed solar cells on Si wafers obtained from B- and Ga-doped commercial Cz ingots grown in the same puller. Therefore, in this study, B- and Ga-doped Cz ingots were grown in an industrial environment at Shell solar industries, and the Cz Si wafers from different locations along the Ga- as well as the B-doped ingots were analyzed. Both the ingots were targeted to have resistivity of ~1 Ω-cm. In addition to the wafers from these two ingots, some B-doped thin wafers with higher resistivity (~4.3 Ω-cm) were included in the study to explore the reduction in the LID effect as proposed in the literature [4-17,4-18]. All three ingots were grown using the exact same growth method and equipment. The bulk lifetime in all the samples was determined by the contactless photoconductance measurement [4-19,4-20]. Manufacturable screen-printed solar cells were fabricated and analyzed using light IV-measurement.

4.2 Experimental Procedures

The Si wafers used in this study were taken from different locations along the two Cz Si ingots: six locations from the 950 mm long, ~1 Ω-cm, B-doped ingot and nine locations from the 925 mm long, 0.5-2.5 Ω-cm, Ga-doped ingot were selected (Table 4-1). Additional wafers were taken from a higher resistivity B-doped ingot (~4.3 Ω-cm) and thinned down to ~230 μm from ~290 μm. Table I summarizes all the wafers used in the study. The lifetime was measured on each sample both in the as-grown state and after the phosphorus emitter diffusion. The post-diffusion lifetime was measured on each sample after $POCl_3$ diffusion at ~880°C followed by etching of the sample down to Si bulk. The lifetime measurements were performed after 1) 200°C anneal to remove any LID effect [4-1] and 2) light-soaking for >20 hrs to obtain the stabilized lifetime after LID. The surface was passivated by iodine/methanol solution during the lifetime measurements.

Screen-printed Al-back surface field (BSF) solar cells (4 cm^2) were fabricated on all the wafers in Table 4-1 using an industrial process. First, the samples were textured in an alkaline etch and then $POCl_3$ diffused to obtain a ~45 Ω/sq emitter. Subsequently, SiN_x AR-coating was deposited on the front. All the samples were then subjected to full-area Al screen-printing on the backside, followed by Ag gridline printing on the front. The samples were then co-fired using rapid thermal processing. No special heat treatment was performed to minimize LID as proposed in the literature [4-4,4-8 – 4-13].

The I-V measurements were taken after annealing the cells at 200°C to remove the LID effect and to determine the cell performance without the LID. The I-V measurements were repeated on all the cells after light soaking them for >20 hrs to obtain the stabilized cell performance after LID.

4.3 Results and Discussion

4.3.1 Growth of Ga-doped Cz Ingots

The crystal growth process appears to be transparent to the use of Ga dopant because same method and equipment was used successfully for B- and Ga-doped Cz growth. In comparison with B-doped Cz Si, the growth of Ga-doped Cz Si does not require an extra effort on the growth control, melt contamination or maintaining structure loss. Maintaining the rate of structure loss is especially important for cost control since it is typically the highest loss category in a Cz crystal growth process. Consequently, no changes to the crystal growth process were necessary to achieve similar yields on Ga-doped ingot.

4.3.2 Resistivity Distribution Along Commercially Grown B-doped and Ga-doped Cz Ingots

Table 4-1 shows that the growth of low-resistivity B-doped ingot provides samples with a tight resistivity control, ranging from 0.87 Ω-cm to 1.22 Ω-cm. However, the resistivity variation is much larger (0.57-2.54 Ω-cm) in the case of the Ga-doped ingot compared to the B-doped ingot. The resistivity decreases appreciably from seed to tail end of the Ga-

doped ingot because of the low segregation coefficient of Ga (k=0.008) compared to B (k=0.8) in Si.

Table 4-1. Description of Cz Si samples used in the study.

Ingot	Thickness		Tail end			Seed end					
Low-ρ B-doped	290μm	Location	1	2	3	4	5	6			
		ρ (Ω·cm)	0.87	0.82	0.90	0.95	1.00	1.22			
Ga-doped	290μm	Location	1	2	3	4	5	6	7	8	9
		ρ (Ω·cm)	0.57	0.63	0.84	0.99	1.19	1.46	1.82	2.17	2.54
Hi-ρ B-doped	230μm	ρ (Ω·cm)	4.3								

4.3.3 As-grown and post-diffusion lifetime in wafers from B- and Ga-doped Cz ingots

4.3.3.1 B-doped ingots

The as-grown and post-diffusion lifetimes for the B-doped Cz samples are summarized in Figure 1a and 1b, respectively. The low-resistivity B-doped ingot showed a very tight distribution of the lifetime except at the seed end, where the lifetime was somewhat lower probably due to the swirl defects that occur in macroscopically dislocation-free Si with a high density of point defects [4-21]. All the bulk lifetime measurements in Figure 4-1 were performed at an injection level of $2x10^{14}$ cm^{-3}.

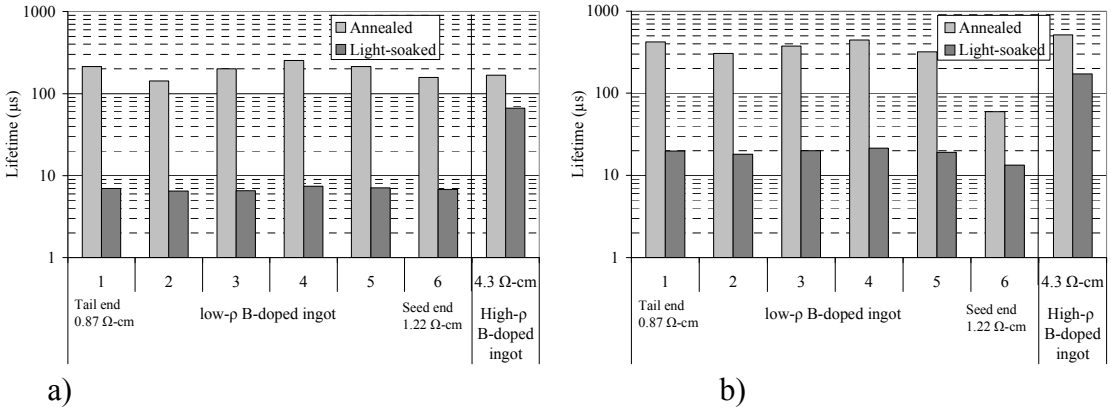

Figure 4-1. (a) As-grown and (b) post-diffusion lifetime before and after LID on wafers from different locations in the low- and high-resistivity B-doped Cz ingots.

Figure 4-1 shows that the phosphorus diffusion enhances the light-soaked lifetime significantly. This is attributed to 1) impurity gettering by phosphorus diffusion [4-22] and 2) the reduction of metastable defects (responsible for LID) by high-temperature treatment. For this reason, the lifetime in the finished cell correlates better with the post-diffusion lifetime rather than the as-grown lifetime. To consider the effectiveness of the high temperature process in the reduction of LID, it is useful to first calculate the normalized metastable defect concentration, defined as $N_t^* = \sigma_n \upsilon_{th} N_t$ [4-23]. This can be calculated from the lifetime in annealed and light-soaked states as follows:

$$N_t^* = \frac{1}{\tau_{light-soaked}} - \frac{1}{\tau_{annealed}} \qquad (4\text{-}1)$$

N_t^* was calculated using eq. (4-1) and the measured lifetime before and after LID at an injection level of $2x10^{14}$ cm^{-3} for all samples. The N_t^* values for as-grown and post-diffusion states are shown in Figure 4-2. Smaller value of N_t^* reflects lower concentration of metastable defects (N_t) that are responsible for LID. Our data shows that the phosphorus diffusion reduced the metastable defect concentration effectively by a factor of 2.8-3.1 in the low resistivity B-doped samples and by a factor of 2.4 in the high-resistivity B-doped sample. In spite of this respectable improvement, the LID managed to lower the post diffusion lifetime by a factor of 15-20 (from ~300-400 μs to ~20 μs) in the low-resistivity (~1 Ω-cm) B-doped wafers (Figure 1b). The high-resistivity B-doped sample, on the other hand, exhibited a much weaker LID effect due to lower B concentration, resulting in about a factor of three degradation in lifetime from ~500 μs to ~170 μs.

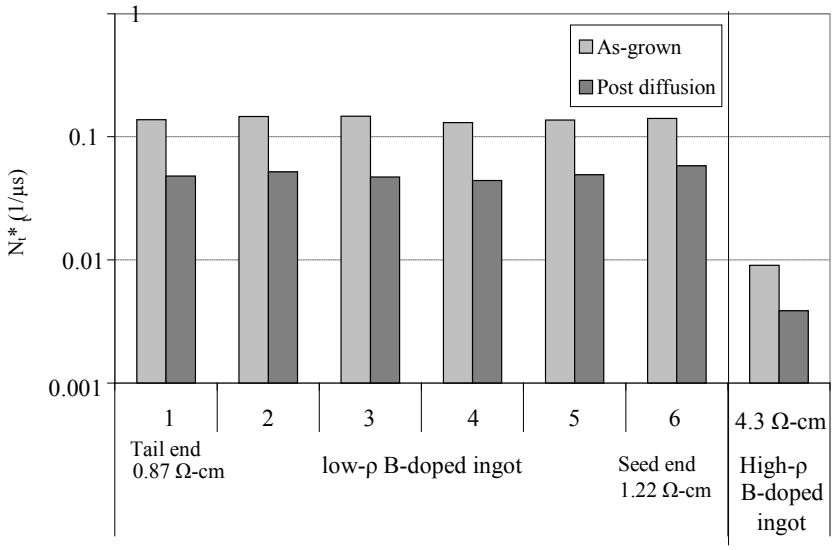

Figure 4-2. Normalized metastable defect concentration before and after diffusion process in B-doped Cz wafers.

4.3.3.2 Ga-doped ingot

The as-grown and post-diffusion lifetimes measured at the injection level of $2x10^{14}$ cm^{-3} for the Ga-doped Cz samples are summarized in Figure 4-3a and 4-3b, respectively. Unlike the B-doped wafers, Ga-doped wafers did not show any LID. However, the post-diffusion lifetime in Ga-doped ingot varied significantly from ~100 to ~1000 μs from seed to tail end partly because of the variation in the resistivity. Both resistivity and lifetime increased gradually from tail to seed end except for a drop at the seed end for the same reason (swirl defects) as the B-doped ingot. Notice that the phosphorus diffusion improved the lifetime of Ga-doped wafers by about a factor of 1.3 due to gettering of impurities.

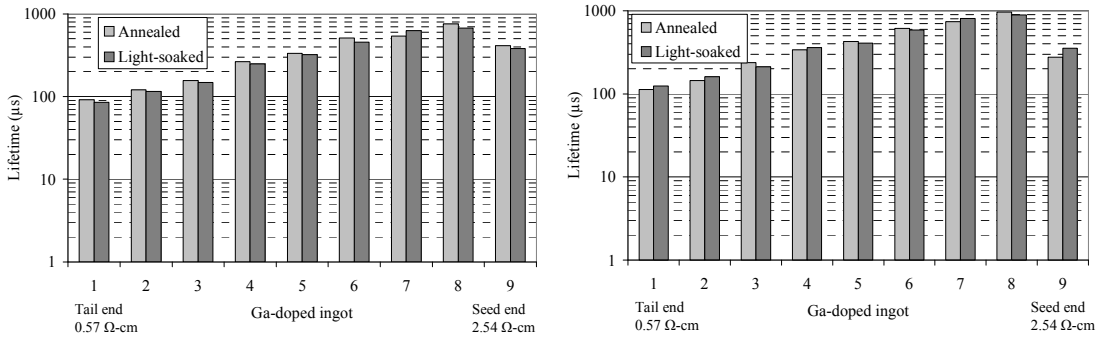

Figure 4-3. (a) As-grown and (b) post-diffusion lifetime before and after LID on wafers from different locations in Ga-doped Cz ingot.

4.4 LID and Performance of Screen-Printed Solar Cells

4.4.1 B-doped Ingots

Simple manufacturable 4 cm^2 screen-printed cells were fabricated with texturing, Al-BSF and SiN_x PECVD single-layer AR coating (Section 2). The efficiency of the solar cells fabricated on wafers taken from different locations on B-doped ingots is plotted in Figure 4-4. Both annealed (no LID) and light-soaked (after LID) states are included in the figure to assess the LID effect.

The efficiency prior to the LID in the low-resistivity B-doped ingot was quite uniform (~16.7%), except at the seed end where the efficiency dropped slightly to 16.5%. This is entirely consistent with the lifetime data in Figure 4-1b, which showed fairly uniform lifetime except at the seed end. However, the efficiency of all the low-resistivity B-doped cells decreased significantly by about 1.1% absolute after the light soaking, resulting in a final efficiency of only ~15.6%. This is also consistent with Figure 4-1b which shows that after the diffusion and light-soaking, the lifetime in all the wafers dropped to ~ 20 μs after LID. The high-resistivity (4.3 Ω-cm) thin (230 μm) B-doped Cz cell gave an efficiency of

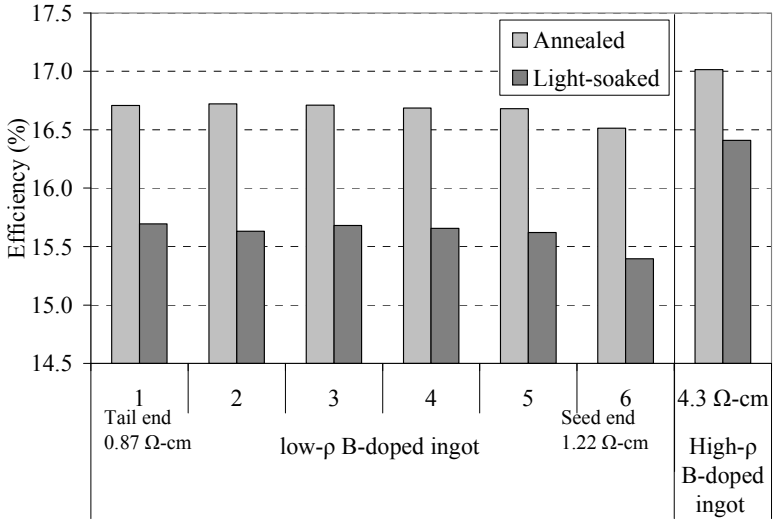

Figure 4-4. Screen-printed Al-BSF solar cells efficiency of samples from different locations from low- and high-resistivity B-doped Cz ingots.

17%, which is ~0.3% better than the low-resistivity B-doped cells. In addition, the LID effect was substantially reduced with an efficiency loss of ≤0.6% absolute as opposed to 1.1% for the low-resistivity thick cells, resulting in the stabilized efficiency of 16.4%. The reduced LID effect is attributed to 1) the reduction of B concentration in the higher resistivity material, resulting in fewer LID traps and 2) higher diffusion length to thickness ratio due to thinner material, resulting in decreased sensitivity to loss in diffusion length. Thus, higher resistivity and thinner material provides another strategy for reducing LID in B-doped Cz cells.

Device simulations were performed using PC1D program [4-24] to establish that the impact of LID on the cell efficiency is entirely based on lifetime degradation at maximum power point (MPP). Some of the key inputs used for PC1D simulation are summarized in Table 4-2. The simulated efficiency as a function of lifetime for a 300 μm thick 1.0 Ω-cm substrate and 230 μm thick 4.3 Ω-cm are plotted in Figure 4-5. Due to a strong asymmetry of the capture time constants for electrons and holes (τ_n/τ_p~0.1), specific for boron-oxygen-related recombination center [4-13], the bulk lifetime of a p-type material strongly depends on the injection level. This dependence of lifetime on injection level needs to be taken into account to assess the accurate and full impact of LID on cell efficiency. Therefore, first we measured the lifetime as a function of injection level in these samples as shown in Figure 4-6. This was done on diffused samples after the emitter was removed. Figure 4-6 confirms the asymmetric capture time constant because lifetime does vary strongly with injection level after LID. Notice that prior to LID, lifetime is high and is not a strong function of injection level. This measured lifetime data was used in conjunction with PC1D calculation of efficiency as a function of lifetime (Figure 4-5) to assess the loss in efficiency due to LID. To do this accurately, the loss in bulk lifetime was determined at the MPP. The device simulations were performed to determine the approximate injection level at the

injection level is not completely uniform along the device thickness. Carrier concentration profiles reveal that in the 1 Ω-cm cell, the injection level varied from $3x10^{12}$ cm^{-3} to $1.2x10^{13}$ cm^{-3} at MPP for 10-30 μs bulk lifetime. Figure 6 shows that in spite of this large variation in injection level, the lifetime should remain nearly constant at about 15 μs. Similarly for the 4.3 Ω-cm cell, the injection level at MPP was found to vary from $2.0x10^{13}$ to $3.1x10^{13}$ cm^{-3} for 80-200 μs bulk lifetime, resulting in a nearly constant lifetime of 105 μs at the MPP. These lifetime values were used in Figure 4-5 to obtain the predicted cell efficiency after LID of 15.7% for 1.0 Ω-cm and 16.6% for 4.3 Ω-cm cells. These efficiencies were in good agreement with the experimental data in Figure 4 (~15.6% for 1.0 Ω-cm and 16.4% for 4.3 Ω-cm Cz). Note that in Figure 4-5, if the measured lifetime at an injection level of $2x10^{14}$ cm^{-3} was used (which is closer to the open circuit voltage (V_{oc}) condition of the cells), the simulation would have underestimated the LID effect on efficiency due to the strong lifetime dependence on injection level. Figure 4-5 also shows that before LID, predicted efficiencies are ~16.7% and ~17.0% for 1.0 Ω-cm and 4.3 Ω-cm cells, which is again in good agreement with the experimental data even though the measured lifetime at $2x10^{14}$ cm^{-3} was used. This is because, prior to LID, measured lifetime is not a strong function of injection level. Thus, in order to predict the LID effect by simulation, one needs to recognize the strong injection level dependence of lifetime and use the measured lifetime at the injection level around the peak power point. Lifetimes in solar cell materials are often measured at the V_{oc} condition or even at higher injection level ($\geq 1x10^{15}$ cm^{-3}) to avoid trapping effects on lifetime data [4-25].

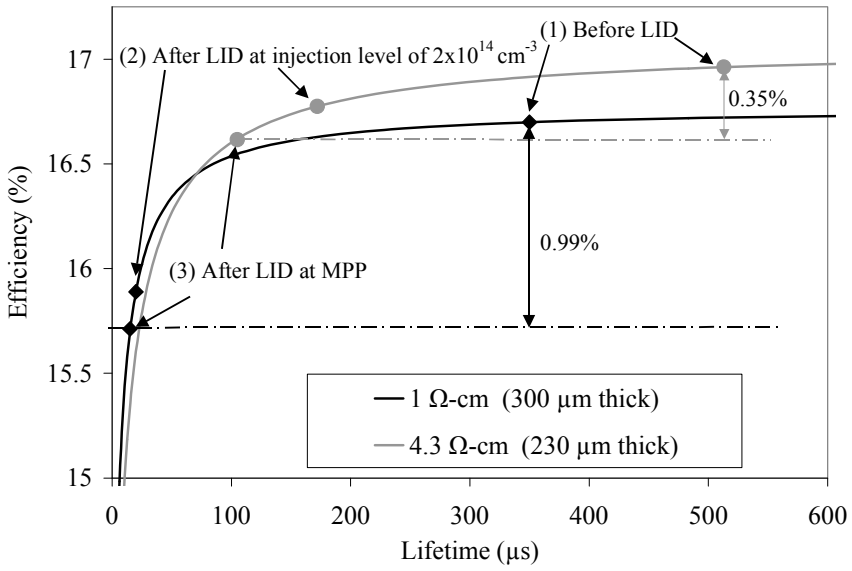

Figure 4-5. Simulated solar cell efficiency as a function of lifetime for a) 1.0 Ω-cm 300 μm thick Si substrate and b) 4.3 Ω-cm 230 μm thick Si substrate. Simulated curves are used to show the predicted cells efficiencies based on measured lifetime (1) before LID, (2) after LID but at injection level of $2x10^{14}$ cm^{-3}, and (3) after LID at an injection level at MPP.

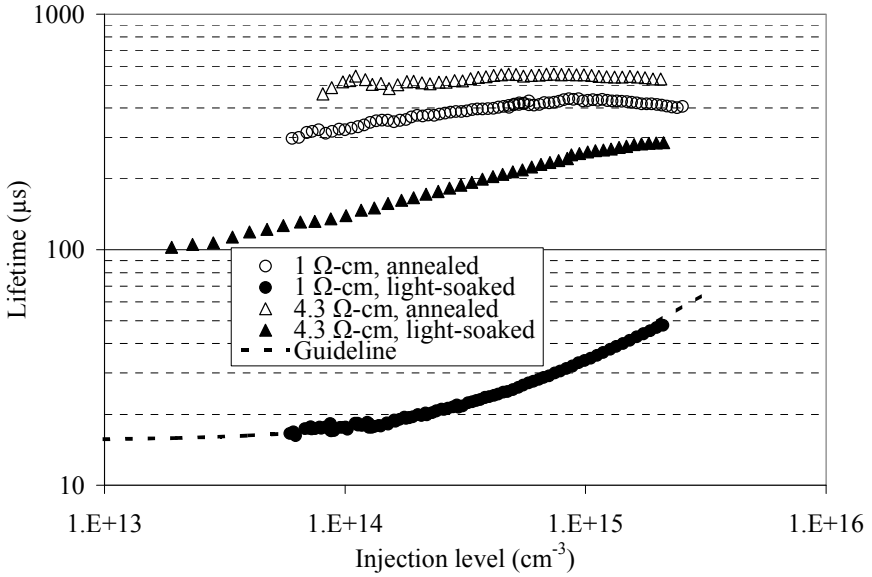

Figure 4-6. Measured bulk lifetime as a function of injection level, before and after LID, for ~1 Ω-cm and ~4.3 Ω-cm B-doped Cz.

Table 4-2. PC1D input parameters for screen-printed cell simulation.

Device Parameter	**Input**
Front surface	Textured, 54.74°, 3.535 µm
Front surface reflectance	From measurement
Broadband reflectance	6.75-7.00 %
Rear internal reflectance	60%, diffuse
Base contact	0.75-0.80 Ω
Internal conductor	1×10^{-4} S
J_{o2}	$3.2\text{-}3.5 \times 10^{-8}$ A
Front doping	45 Ω/sq, Erfc
FSRV	95,000-120,000 cm/s
BSRV	750 cm/s for 1.0 Ω-cm 150 cm/s for 4.3 Ω-cm

4.4.2 Ga-doped Ingot

The variation in efficiency of the screen-printed Al-BSF solar cells fabricated on wafers from different ingot locations of Ga-doped ingot is plotted in Figure 4-7. Both annealed (no LID) and light-soaked (after LID) states are included in the figure.

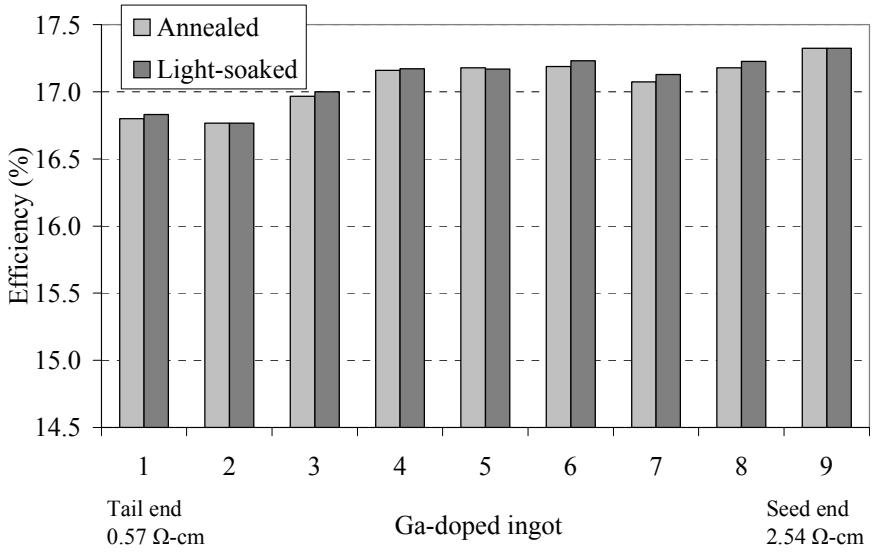

Figure 4-7. Screen-printed Al-BSF solar cells efficiency of samples from different locations from Ga-doped Cz ingot.

Unlike the B-doped ingots, the efficiency spread in Ga-doped ingot prior to the LID is somewhat larger (16.8%-17.3%), with the higher resistivity seed end producing slightly higher efficiency. This variation in efficiency is generally acceptable for production and is within the range of process-induced effects. Detailed analysis of cell parameters in Figure 8 shows that, despite the very wide variation in resistivity over the entire length of the ingot, the spread in Ga-doped cell efficiency is reduced because of the increase in V_{oc} and the decrease in short circuit current density (J_{sc}) as the resistivity decreases. Note that spread in current due to resistivity variation in Ga-doped cells may add to the spread in current due to the processing effects. However, if the cells are binned according to current and efficiency combination, rather than just current, then it will be possible to separate different resistivity cells in appropriate bins, to avoid cells' voltage mismatch losses, prior to module fabrication. Moreover, there is essentially no LID observed in the Ga-doped cells, resulting in ~1.5% higher absolute efficiency after light soaking relative to the low-resistivity B-doped Cz ingot. This gap in stabilized efficiency was reduced to ~0.7% when higher resistivity and thin B-doped Cz was used. These results show that the Ga-doped Cz ingot offers great potential for higher stabilized Cz cell performance (≥ 17%). In addition, a high-quality Ga-doped ingot can be grown in the same puller used for the B-doped ingot, without any modification.

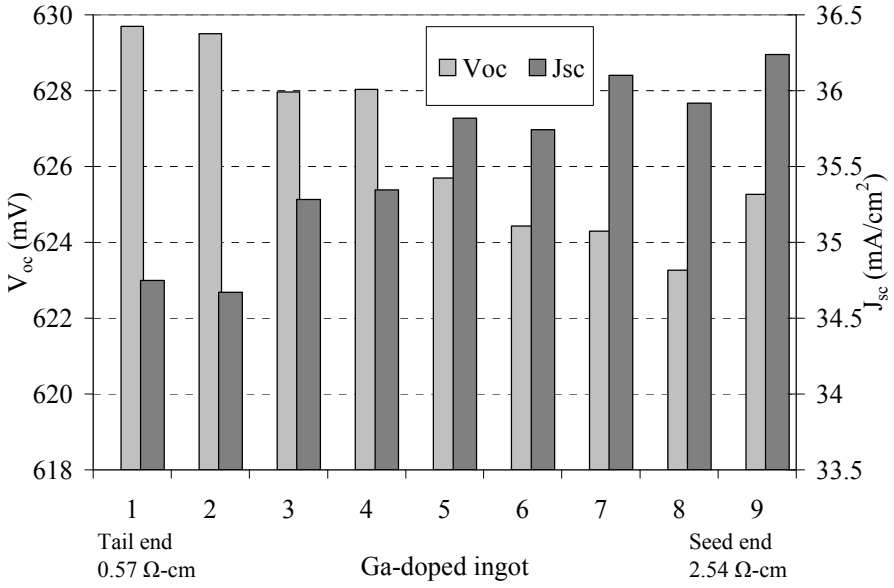

Figure 4-8. J_{sc} and V_{oc} as a function of ingot position in Ga-doped ingot.

Table 4-3 summarizes the average efficiency of solar cells from the three Cz Si ingots. These data demonstrate the potential of using Ga-doped Cz instead of B-doped Cz.

Table 4-3. Summary of averaged efficiency from different Cz ingots.

Dopant Type	**Resistivity (Ω-cm)**	**Efficiency (%)**	
		Annealed	**Stabilized**
Boron	~ 1.0	16.7	15.6
	~4.3	17.0	16.4
Gallium	0.57-2.54	17.1	17.1

4.5 Conclusions

This paper demonstrates the potential of using Ga dopant instead of B in p-type Cz Si to achieve high efficiency manufacturable screen-printed cells with no LID. Despite a large resistivity variation (0.57-2.54 Ω-cm) in the Ga-doped Cz ingot resulting from a small segregation coefficient of Ga in Si, the absolute efficiency of screen-printed Al-BSF solar cells was found to vary by <0.5% absolute over the entire length of the 925 mm long ingot. This is the result of the competing effect of increasing V_{oc} and decreasing J_{sc} as the resistivity decreases. In the 1 Ω-cm B-doped Cz, lifetimes decreased from 300-400 to ~20 µs after LID. In the 4.3 Ω-cm B-doped Cz, lifetimes decreased from 500 µs to 170 µs after LID. In the Ga-doped ingot, lifetimes were in the range of 100-1000 µs from seed to tail end, respectively, and showed no LID at all. This resulted in ~1.5% higher average

stabilized efficiency compared to the cells made on a 1 Ω-cm B-doped Cz and about 0.7% higher than efficiency with respect to 4.3 Ω-cm thin B-doped cells. These results were found to be in good agreement with device simulations performed using the measured lifetime at the injection level at MPP.

The use of thinner and high-resistivity B-doped Cz lessened the detrimental effect of LID. However, the LID remained appreciable and accounted for ~0.6 % absolute reduction in efficiency. Ga doping completely eliminated the LID in Cz cells and gave ≥ 17% efficient screen-printed solar cells.

4.6 References

[4-1] Fischer H, Pschunder W. Investigation of photon and thermal induced changes in silicon solar cells. In *Conference Record, 10th IEEE Photovoltaic Specialists Conference.* Palo Alto, November 1973; 404-411.

[4-2] Knobloch J, Glunz SW, Henninger V, Warta W, Wettling W. 21% efficient solar cells processed from Czochralski grown silicon. In Conference Proceedings, 13th European Photovoltaic Solar Energy Conference. Nice, October 1995; 9-12.

[4-3] Schmidt J, Aberle AG, Hezel R. Investigation of carrier lifetime instabilities in Cz-grown silicon. In Conference Record, 26th IEEE Photovoltaic Specialists Conference. Anaheim September/October 1997; 13-18.

[4-4] Glunz SW, Rein S, Warta W, Knobloch J, Wettling W. On the degradation of Cz-silicon solar cells. In Conference Proceedings, 2nd World Conference on Photovoltaic Solar Energy Conversion. Vienna, July 1998; 1343-1346.

[4-5] Glunz SW, Rein S, Knobloch J, Wettling W, Abe T. Comparison of boron- and gallium-doped p-type Czochralski silicon for photovoltaic application. Progress in Photovoltaics 1999; 7: 463-469.

[4-6] Saitoh T et al. Light degradation and control of low-resistivity Cz-Si solar cells – An international joint research-. In Technical Digest, 11th International Photovoltaic Science and Engineering Conference. Sapporo, September 1999; 553-556.

[4-7] Knobloch J, Glunz SW, Biro D, Warta W, Schäffer E, Wettling W. Solar cells with efficiencies above 21% processed from Czochralski grown silicon. In Conference Record, 25th IEEE Photovoltaic Specialists Conference. Washington, May 1996; 405-408.

[4-8] Nagel H, Merkle A, Metz A, Hezel R. Permanent reduction of excess-carrier-induced recombination centers in solar grade Czochralski silicon by a short yet effective anneal. In Conference Proceedings, 16th European Photovoltaic Solar Energy Conference. Glasgow, May 2000; 1197-1200.

[4-9] Rein S, Knobloch J, Glunz SW. Analysis of the high-temperature improvement of Cz-silicon. In Conference Proceedings, 16th European Photovoltaic Solar Energy Conference. Glasgow, May 2000; 1201-1205.

[4-10] Schmidt J, Cuevas A. Progress in understanding and reducing the light degradation of Cz silicon solar cells. In Conference Proceedings, 16th European Photovoltaic Solar Energy Conference. Glasgow, May 2000; 1201-1205.

[4-11] [-Glunz SW, Lee JY, Rein S. Strategies for improving the efficiency of Cz-silicon solar cells. In Conference Record, 28th IEEE Photovoltaic Specialists Conference. Anchorage September 2000; 201-204.

[4-12] Lee JY, Peters S, Rein S, Glunz SW. Improvement of charge minority-carrier lifetime in p(boron)-type Czochralski silicon by rapid thermal annealing. Progress in Photovoltaics 2001; 9: 417-424.

[4-13] Bothe K, Schmidt J, Hezel R. Effective reduction of the metastable Defect concentration in boron-doped Czochralski silicon for solar cells", In Conference Record, 29th IEEE Photovoltaic Specialists Conference. New Orleans May 2002; 194-197.

[4-14] Crabtree G, Jester TL, Fredric C, Nickerson J, Meemongkolkiat V, Rohatgi A. Production viability of gallium doped mono-crystalline solar cells. In Conference Record, 31st IEEE Photovoltaic Specialists Conference. Lake Buena Vista January 2005; 935-938.

[4-15] Metz A, Abe T, Hezel R. Gallium-doped Czochralski grown silicon: a novel promising material for the PV-industry. In Conference Proceedings, 16th European Photovoltaic Solar Energy Conference. Glasgow, May 2000; 1189-1192.

[4-16] Diez S, et al. Alternatives to boron-doped Czochralski for silicon solar cell processing. In Conference Proceedings, 19th European Photovoltaic Solar Energy Conference. Paris, June 2004; 504-507.

[4-17] Münzer KA, Holdermann KT, Schlosser RE, Sterk S. Thin monocrystalline silicon solar cells. IEEE Transactions on Electron Devices 1999; ED-46: 2055-2061.

[4-18] Damiani B, Ristow A, Ebong A, Rohatgi A. Design optimization for higher stabilized efficiency and reduced light-induced degradation in boron-doped Czochralski silicon solar cells. Progress in Photovoltaics 2002; 10: 185-193.

[4-19] Sinton RA, Cuevas A. Contactless determination of current-voltage characteristics and minority-carrier lifetimes in semiconductors from quasi-steady-state photoconductance data. Applied Physics Letters 1996; 69: 2510-2512.

[4-20] Nagel H, Berge C, Aberle AG. Generalized analysis of quasi-steady-state and quasi-transient measurements of carrier lifetimes in semiconductors. Journal of Applied Physics 1999; 86: 6218-6221.

[4-21] Fan TW, Qian JJ, Wu J, Lin LY, Yuan J. Tentative analysis of Swirl defects in silicon crystals. Journal of Crystal Growth 2000; 213: 276-282.

[4-22] Polignano ML, Cerofolini GF, Bender H, Claeys C. Gettering mechanisms in silicon. Journal of Applied Physics 1988; 64: 869-876.

[4-23] Glunz SW, Rein S, Lee JY, Warta W. Minority carrier lifetime degradation in boron-doped Czochralski silicon. Journal of Applied Physics 2001; 90: 2397-2404.

[4-24] Clugston DA, Basore PA. PC1D version 5: 32-bit solar cell modeling on personal computers. In Conference Record, 26th IEEE Photovoltaic Specialists Conference. Anaheim September/October 1997; 207-210.

[4-25] Cuevas A, Stocks M, Macdonald D, Kerr M, Samundsett C. Recombination and trapping in multicrystalline silicon. IEEE Transactions on Electron Devices 1999; ED-46: 2026-2034.

5. Understanding the Formation of High-Quality Thick-Film Ag Contacts on High Sheet-Resistance Si Emitters for Solar Cells

5.1 Introduction

Screen-printed solar cells have been around for about three decades; however, little is understood about the physics and chemistry of the formation of thick-film silver contacts to the Si emitter, as well as carrier transport at and near the Ag-Si interface and its precise correlation with the quality of the ohmic contact. Reasonably good quality screen-printed Ag contacts are routinely achieved on 45 Ω/sq emitters for solar cells. However, making good ohmic contacts to high sheet-resistance (80-100 Ω/sq) emitters is still a challenge. Several manufacturers around the world are working and partly succeeding on the development of Ag pastes that work for high sheet-resistance emitters [5-1]. Silver thick-film pastes typically contain silver powder, glass frit, and organic binder. The glass frit is important in influencing the contact quality because it can affect adhesion, conduction, and contact formation. The glass frit normally consists of lead oxide containing silicate glass. It has been shown that Ag dissolution in the glass frit occurs upon firing [5-2]. Recently, Ag crystallites have been shown to grow into the Si surface from the glass [5-3, 5-4]. The lead borosilicate glass layer over most of the interface is assumed to be insulating because of its high resistivity. Thus, current transport is projected to take place via islands of Ag and Si contact [5-5]. Ballif et al. validated the presence of Ag crystallites at the Ag-Si interface along with very low contact resistivity ($\sim 2\times10^{-7}$ Ω-cm^2) between these Ag crystallites and the Si emitter coupled with the very high resistivity (10^9 Ω-cm) of glass and thus current transport from the Ag crystallites to the Ag bulk through ultrathin glass regions has been proposed [5-6]. It has also been proposed [5-4] that conduction takes place via multi-step tunneling via metal precipitates in the glass layer between Ag crystallites at the Ag-Si interface and the Ag bulk of the grid. Moreover, the chemistry of glass frit/modifiers can greatly influence junction shunting and the junction leakage current because of etching of Si by the glass frit during the contact firing cycle and possible migration of metal impurities present in the glass into the emitter region [5-7- 5-9]. The above ideas have been used and expanded to explain why, of the three Ag pastes we have studied in this paper, PV168 paste from Dupont gave high fill factors (FFs) while the other two pastes did not work as well on 100 Ω/sq emitters [5-10, 5-11]. To gain a better understanding of the requirements for achieving good screen-printed ohmic contacts, two other widely used commercial thick-film pastes (A and B) were studied in an attempt to analyze and correlate the electrical and physical behaviors of screen-printed contacts.

5.2 Experimental Method

In this study, screen-printed n^+-p-p^+ solar cells (4 cm^2) were fabricated on single crystal Si using different Ag pastes and firing conditions on a 100 Ω/sq emitter. P-type, 0.6 Ω-cm, 300-μm-thick (100) float-zone (FZ) substrates were used for all the experiments. Silicon wafers were first chemically cleaned, followed by $POCl_3$ diffusion to form the n^+-emitter. After the phosphorus-glass removal and another clean, plasma-enhanced chemical vapor

deposited (PECVD) SiN_x antireflection (AR) coating was deposited on the emitter. Next, an Al paste was screen-printed on the backside and dried at 200°C. A Ag grid was then screen-printed on top of the SiN_x film, and Ag and Al contacts were co-fired (single firing step) in a lamp-heated three-zone belt-line furnace. All the cells were then isolated using a dicing saw and were annealed in forming gas at 400°C for ~15 minutes. Cross-sectional scanning electron microscopy (SEM) and plane-view atomic force microscopy (AFM) measurements were taken to study the structure of the Ag-Si interface. Cross-sectional conductive AFM (CAFM) images were taken to investigate the conductivity through the bulk of the PV168 Ag gridline for high and low firing temperatures. The CAFM technique uses a bias voltage applied between a highly conductive tip and the Al back contact as the tip passes over the cross-sectional grid. No etching was found necessary for the cross-sectional SEM and CAFM measurements. However, the Ag grid was etched prior to the AFM using HF, HNO_3 and HF acids in sequence to remove the metal and the glass to delineate the footprints of the etched Ag crystallites by removing the metal and the glass. The plane-view AFM images of the surface morphology were acquired in intermittent tapping mode. Cross-sectional TEM was performed on selected samples. The sample preparation for the TEM measurement involved standard mechanical polishing down to about 50 μm followed by dimple polishing down to a thickness around 5μm. The samples were then ion beam milled using a Gatan precision ion polishing system (PIPS) at low energy, and low angle. Secondary-ion mass spectroscopy (SIMS) measurements were taken on selected samples to determine the Ag and P concentration profiles in the silicon directly underneath the Ag grid using a CAMECA IMS-5F ion microscope. The Ag grid was etched in HCl for the SIMS measurements to prevent any Si etching. The samples were bombarded with 5.5 KeV O_2^+ primary ions for the analysis of Ag whereas14.5 KeV Cs^+ primary ions were used for P. The primary ion beam was rastered over an area of 150 μm × 150 μm. Positive or negative secondary ions were collected from a ~20-μm-diameter area in the center of the rastered crater for Ag and P, respectively. Contact resistance was determined by using the transfer-length method (TLM) pattern [5-12], printed simultaneously with the grid, while the cell parameters were measured by dark and light I-V measurements.

5.3 Results and Discussion

Three different screen-printing pastes (A, B, and PV168) were investigated using SEM, AFM, and SIMS analysis in conjunction with contact resistance and solar cell performance measurements to understand and establish a correlation between physical and electrical properties of screen-printed contacts on a high sheet-resistance emitter (100 Ω/sq). Two of the pastes (A and B) are widely used in industry, and the third paste (PV168) is commercially available from Dupont, but its use is not as widespread. All the three pastes contained some P which could result in self-doping. Therefore, SIMS measurements were first taken to check the formation of selective emitter via the injection of P underneath the gridlines. This was determined by printing and firing the three pastes on an undiffused wafer (no emitter). Figure 5-1 shows that all three pastes introduced limited amount of P near the Si; thus, for the high-temperature (835°C) firing condition used in this study injected P profiles resulted in sheet resistance of 900-5000 Ω/sq. More important, the

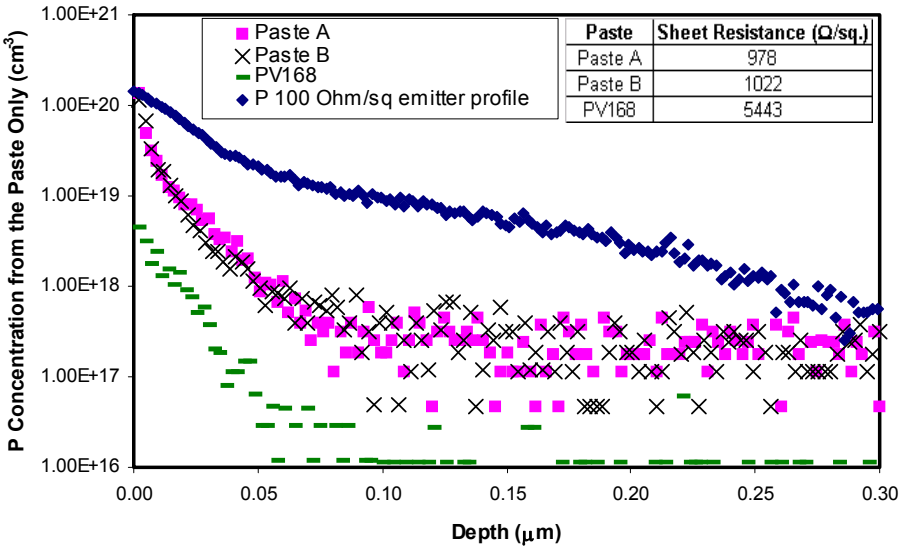

Figure 5-1. SIMS profiles of P detected in Si after 835°C fast firing of pastes A, B, and PV168 on undiffused Si. P profile for a 100 Ω/sq emitter is also shown for comparison.

self-doping P concentration is much smaller than the P concentration associated with the diffusion of 100 Ω/sq emitter (Fig. 5-1). Since the injected P concentration does not alter the net P concentration underneath the grid, selective emitter formation can be precluded (unless it is within a few atomic layers, which may be affected or dissolved during the removal of Ag with HCl). Figure 5-1 also shows that the PV168 paste introduces much less P into Si compared to pastes A or B when fired at high temperatures. Thus, we can ignore self-doping as the basis for any similarity and differences between the contacts formed by these pastes. This led to the SEM and AFM investigation of Ag crystallites and interface structure in the following sections to explain the difference in the electrical performance of the contacts.

5.3.1 Effect of Firing Temperature on the Ag-Si Contact Interface for PV168 Paste

Table 5-1 summarizes the electrical performance of contacts and solar cells fabricated with PV168 Ag paste on 100 Ω/sq emitter using conventional 750°C firing and a higher-temperature (835°C) firing. It is clear from Table 5-1 that the lower-temperature (750°C) co-firing of PV168 paste results in unacceptably high contact resistance (45 mΩ-cm^2) in conjunction with low FF (0.643) and poor cell efficiency (14.37%). However, the 835°C firing produced excellent ohmic contacts with specific contact-resistance of ~2 mΩ-cm^2 and series resistance of 0.7 Ω-cm^2, resulting in a FF of 0.77 on a 100 Ω/sq emitter and a FZ Si cell efficiency of 17.4%.

Table 5-1. The electrical performance of contacts and Si solar cells formed with paste PV168 on a 100 Ω/sq emitter using low- (conventional) and high-temperature firing.

Paste	Peak Temp.	Emitter (Ω/sq)	V_{oc} (mV)	J_{sc} (mA/cm^2)	FF	Eff (%)	n factor	R_s (Ω-cm^2)	R_{sh} (Ω-cm^2)	ρ_c (mΩ-cm^2)	J_{o2} (nA/cm^2)
PV168	750	100	643	34.75	0.643	14.37	1.06	4.391	148,900	45.59	14
PV168	835	100	646	34.48	0.782	17.42	1.08	0.854	131,404	1.98	15

To gain a better understanding of the cell results, contact interface analysis was performed using SEM, AFM, and SIMS. The SEM image (Fig. 5-2(a)) of the interface of the Ag-Si contact fired at 835°C revealed the presence 50-200-nm wide re-grown Ag crystallites. Figure 5-2(b) shows the AFM image of the plane view of the same sample (for 835°C firing) after etching the Ag and the glass frit. Distributed pits observed in the AFM image are indicative of the footprints of the Ag crystallites, which were removed during the Ag etching prior to AFM. The AFM image in Figure 5-2(b) also reveals that the depth of these crystallites in the Si is on the order of 50 nm (notice that the depth scale goes from 0-100 nm), which is much smaller than the junction depth of ~0.28 μm for the 100 Ω/sq emitter. This is in good agreement with the slight shift observed in the SIMS P profiles for regions with and without the gridline, which showed a displacement of ~55 nm, approximately equal to the penetration depth of the Ag crystallites for the PV168 paste [5-11]. The Ag crystallite penetration depth of only ~50 nm also explains why there was no appreciable shunting in the case of PV168 paste even after the 835°C firing. The R_{sh} and J_{o2} values were very reasonable (131.4 kΩ-cm^2 and 15 nA/cm^2, respectively), contributing to the observed high FF of 0.782 (Table 5-1).

The AFM images in Figures 5-2(b) also reveals a larger number of Ag crystallites than reported in [6] for a conventional paste and firing scheme. The regular transfer of dissolved Ag through the glassy layer to the Si surface, resulting in a regular distribution of a large number of Ag crystallites (shown in Fig. 5-2(a) and 5-2(b)) could be attributed to the lower glass transition temperature which has been shown to precipitate a larger amount of Ag crystallites [5-1]. The higher-temperature firing (835°C) dissolves more Ag into the glass frit, possibly reaching saturation, and upon cooling; the excess Ag may precipitate at the Ag-Si interface as crystallites. PV168 paste composition is such that even at ~835°C firing, which was necessary to give acceptable contact and series resistance, Ag crystallites were small enough (much less than the 0.28 μm junction depth) to avoid junction shunting. This was the key to achieving high FF on a 100 Ω/sq emitter with PV168 paste. For the lower temperature firing of 750°C Ag crystallites were very rare or generally not observed at all using high-magnification SEM. Hence, to explain this behavior TEM analysis was performed on the 750° C-fired sample. The TEM micrograph in Fig. 5-3 shows that a SiNO layer, which has a variable thickness, is not completely etched by the glass frit indicating a less aggressive glass frit chemistry compared with conventional pastes, which achieve good ohmic contacts at conventional firing temperatures. The thickness of the lead borosilicate glass varies extensively as shown in Fig. 5-3. The thickness of the SiNO layer is ~65 nm which is too thick for tunneling to take place. Full penetration of the antireflection coating is necessary for a good contact with the emitter leading to low contact resistance [5-7]. This explains the high contact resistance observed for the PV168 Ag paste when fired at conventional firing temperatures of ~750°C. Regions where the SiNO is completely etched could be very sparse at this firing temperature.

Over-firing increases the aggressiveness of the etching reaction between the glass frit and the SiNO layer. Thus, the SiNO is completely etched (in most regions), allowing the glass frit to reach and dissolve the underlying Si which recrystallizes upon cooling with the Ag crystallites growing epitaxially as shown in Fig. 5-2(a).

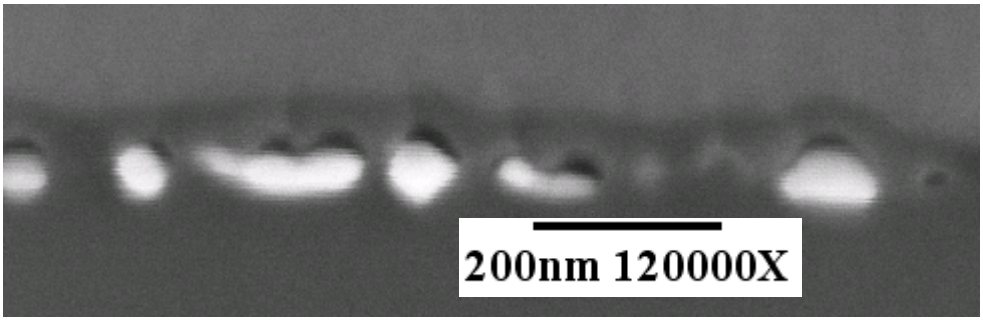

Figure 5-2(a). SEM image of the Ag-Si interface for PV168 fired at 835°C.

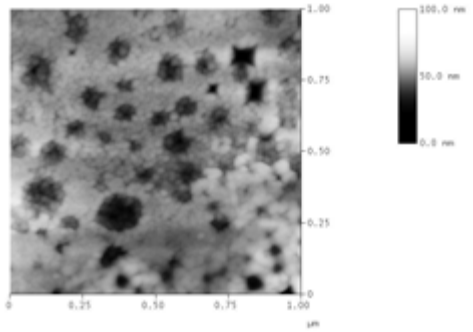

Figure 5-2(b). AFM plane-view of the Si interface for PV168 fired at 835°C.

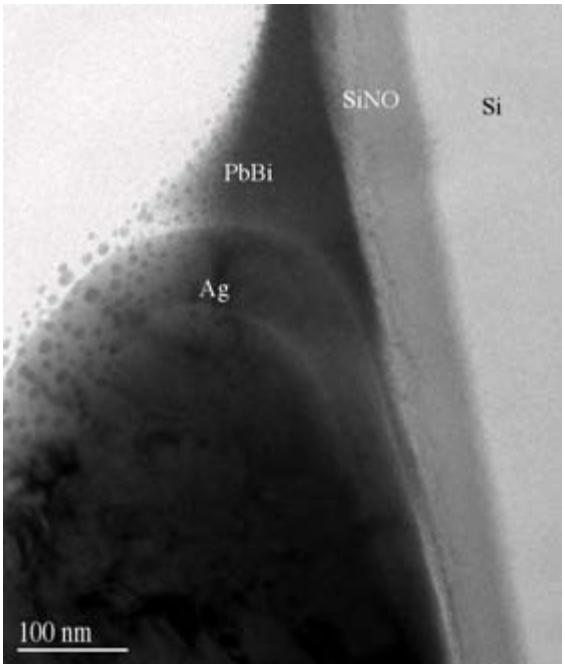

Figure 5-3. TEM micrograph of a 750°C-fired PV168 Ag/Si contact.

Figures 5-4(a) and 5-4(b) show the cross-sectional conductive AFM images of the bulk of the Ag gridline and the Si beneath it for 750°C and 835°C firing temperatures. This technique can probe the variation in the conductivity of the gridline from top to bottom. The presence of a glass layer in the grid or at the interface can lower the grid conductivity in those regions. The bright contrast shows high conductivity or high current between the probes for the same probing voltage applied between the back Al and the probing point in the grid. CAFM conductivity results can also be influenced by (a) the conductivity of the grid Ag, which could be a function of Ag grain size and sintering, (b) the area fraction of the Ag crystallites at the interface, (c) the number of direct contact points between the bulk of the Ag grid and the Ag crystallites at the interface, and (d) the conductivity of the frit or tunneling through the glass layer (where it is thin enough) to complete the current path between Ag crystallites at the interface and the bulk of the grid. Although a few direct interconnections between the interface Ag crystallites and the Ag bulk might exist, none were observed using both the high magnification SEM and TEM. The observed non-homogeneous conductivity of the Ag gridline in Figure 5-4, particularly near the Ag-Si interface, is attributed to the presence of varying thickness of high-resistivity glass between Si and the Ag grid.

The CAFM measurements also confirmed that both firing temperatures gave non-rectifying ohmic contacts because similar current values were obtained when the applied voltage polarity was switched. However, for the lower firing temperature of 750°C, absolute conduction through the bulk of the PV168 gridline was lower (~350 nA current at 200 mV) compared to 1800 nA current at 200 mV. To achieve the same current (≥1800 nA) for the 750°C-fired grid, the voltage applied to the grid had to be increased significantly from 200 mV to 1000 mV.

The Ag particle size, shape, surface area, surfacant treatment, as well as the glass frit all affect the sintering behavior of the Ag gridline [5-13,5-14]. The characteristics of the Ag particles and glass frit in PV168 are such that the Ag particles do not sinter as well at 750°C to produce higher Ag grain size within the bulk of the grid. It has been shown in [5-15] that the Ag grain growth increases with firing temperature, yielding denser films and causing the sheet resistivity of the Ag thick films to decrease with higher sintering temperatures in the range of 450°C -800°C. We found similar behavior for the PV168 Ag paste (Figs. 5-5(a) and 5-5(b)) where Ag grain size was of ~4.5 μm after the 835°C firing as opposed to ~2.1 μm for the 750°C firing. In addition, the grains formed at 835°C firing showed a very compact structure. This yielded a lower gridline resistivity of ~1.9 μΩ-cm, which is close to the resistivity of pure Ag (~1.7 μΩ-cm). The gridline resistivity after the 750°C firing was ~2.5 μΩ-cm.

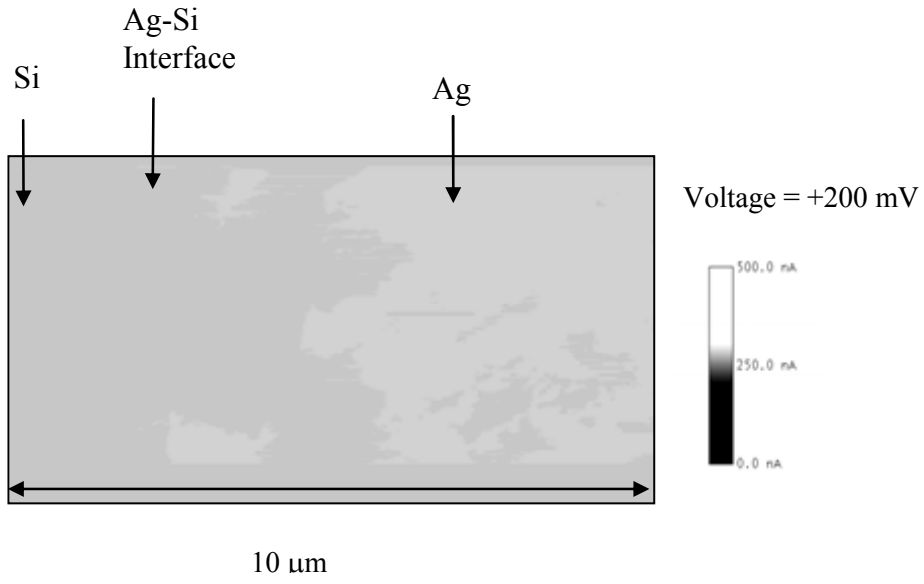

Figure 5-4(a). Cross-sectional conductive AFM of the Ag gridline fired at 750°C.

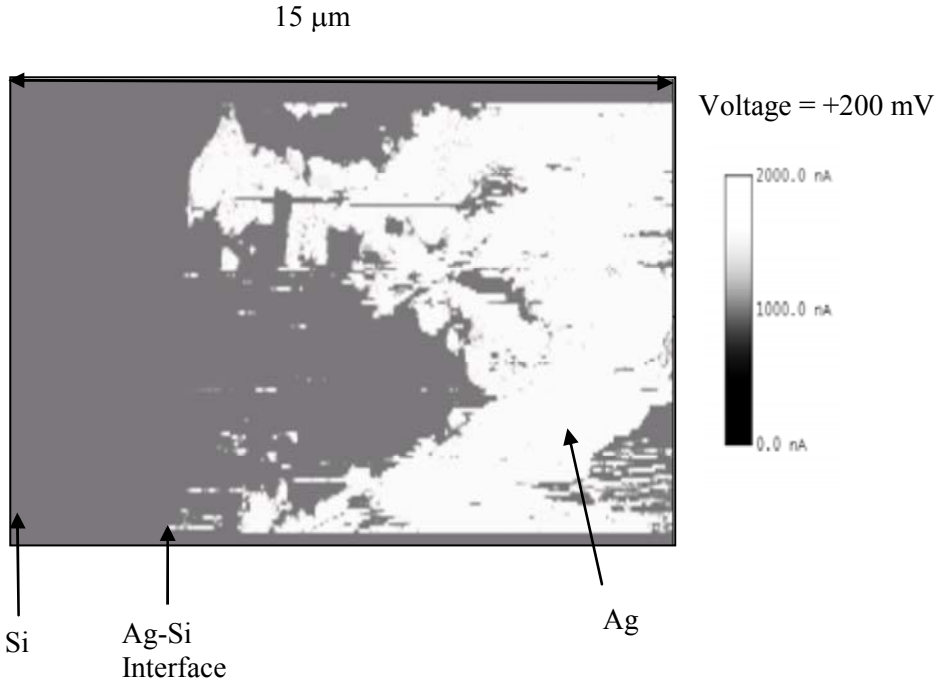

Figure 5-4(b). Cross-sectional conductive AFM of the Ag gridline fired at 835°C.

Figure 5-3 shows that 835°C firing produces larger Ag crystallites with increased Ag-Si contact fraction. If current transport mostly takes place via tunneling through ultra thin glass regions as proposed in [5-6], an increase in the area coverage of the Si emitter by the Ag crystallites would also increase the probability of encounter of these regions. Also, if the current transport takes place via direct interconnection between the Ag bulk and interface crystallites, an increase in the Ag-Si area coverage due to a larger number of Ag crystallites would also decrease the contact resistance. Finally, the relative conductivity of the darker regions near the Ag-Si interface in Figure 5-4, may be indicative of glass conductivity which is lower than that of the Ag. The electrical conductivity model for discontinuous metal structures is based on the tunneling process between metal granules [5-16]. Pb atoms usually agglomerate into large Pb crystallites, and thus, tunneling is difficult to occur; Bi ions have been found to decrease the conductivity of lead-silicate glasses significantly because they act as tunneling centers [5-16]. Bi has been observed in the glass frit in PV168 Ag paste (Fig. 5-3), which would explain why the glass is conductive, although not as well as Ag, as shown in Fig. 5-4. The conductivity is lower for both the Ag and glass regions for the 750°C firing due to the incomplete etching of the SiNO layer. Thus, the effective series resistance for the 835°C firing is only 0.854 Ω-cm^2 as opposed to 4.39 Ω-cm^2 for the 750°C firing (Table 5-1). The improvement in the sintering of the Ag particles for the higher firing temperature (835°C) is not significant enough to yield the observed improvement in conductivity shown in the CAFM images in Figure 5-4(b). From Figs 5-3 and 5-4 limited current transport between the Si emitter and the Ag bulk can be attributed as the main reason for the high contact resistance for the 750°C fired cell because of the incomplete etching of the dielectric layer. By increasing the aggressiveness of the glass frit in PV168 the SiNO layer could be completely etched at 750°C. Regions where the glass is very thin (Fig. 5-3) could help improve the current transport via tunneling or by facilitating the existence of a direct connection between the Ag crystallites and Ag bulk.

To understand the role of the frit we investigated another DuPont paste (PV167), which is analogous to PV168 but without the glass frit. We did not get proper adhesion with PV167 paste when fired at 835°C for a few seconds. This suggests that for the fast firing condition, the presence of the glass frit plays an important role in achieving proper contact even at the Ag-Si eutectic temperature of 835°C [5-17]. Thus, the glass frit helps to adequately dissolve Ag at the Ag-Si eutectic temperature to produce large uniformly distributed crystallites. In addition, the Ag also sinters well at 835°C to give large Ag grains. Even though the PV168 Ag paste was initially designed to operate as a self-doping paste at temperatures greater than the Ag-Si eutectic of 835°C, it appears that the Ag-Si alloying temperature is also significant in that it is the temperature where the glass frit and Ag particles of PV168 were designed to operate to give better contact quality [5-18]. This is why the PV168 performs well around the Ag-Si eutectic temperature and fails at the low firing temperature for high sheet-resistance emitters.

5.3.2 *Investigation of Screen-Printed Contacts to 100 Ω/sq Emitter Using Widely Used Commercial Pastes A and B and Conventional Firing Temperature*

After establishing that PV168 can form good contacts to a 100 Ω/sq emitter at 835°C, we investigated the performance of two widely used Ag pastes A and B. Commercial pastes are generally fired at sample temperatures around 750°C to avoid junction shunting. This process works well for the 45 Ω/sq emitter. Table 5-2 shows that pastes A and B gave reasonably low R_s (~0.8 Ω-cm^2), J_{o2} (~25 nA/cm^2), and high R_{sh} (>7 kΩ-cm^2) on 45 Ω/sq emitter, producing FFs of greater than 0.77 and cell efficiency >16.7% on FZ Si. However, Table 5-3 shows that both pastes failed on the 100 Ω/sq emitter with the 750°C firing condition.

Table 5-2. Electrical performance of contacts and solar cells formed with Ag pastes A and B using 45 Ω/sq emitters and conventional firing temperatures of 750°C

Paste	Peak Temp.	Emitter (Ω/sq)	V_{oc} (mV)	J_{sc} (mA/cm^2)	FF	Eff (%)	n factor	R_s (Ω-cm^2)	R_{sh} (Ω-cm^2)	ρ_c (mΩ-cm^2)	J_{o2} (nA/cm^2)
Paste A	750	45	631	33.10	0.782	16.34	1.10	0.802	7,838	0.24	25
Paste B	750	45	634	33.74	0.7816	16.71	1.09	0.880	96,782	0.43	26

Table 5-3 Electrical performance of contacts and solar cells formed with Ag pastes A and B using 100 Ω/sq emitters and conventional firing temperature of 750°C.

Paste	Peak Temp	Emitter (Ω/sq)	V_{oc} (mV)	J_{sc} (mA/cm^2)	FF	Eff (%)	n factor	R_s (Ω-cm^2)	R_{sh} (Ω-cm^2)	ρ_c (mΩ-cm^2)	J_{o2} (nA/cm^2)
Paste A	750	100	639	33.82	0.73	15.77	1.08	2.067	11,454	3.59	27
Paste B	750	100	582	34.19	0.575	11.44	3.59	0.449	43,518	0.4	2678

The plane-view AFM photograph in Figure 5-5(a) shows that the 750°C firing of paste A produced a highly irregular distribution of Ag crystallites. In addition, the contact area is quite small, which may not be suitable for high sheet-resistance emitters. This observation is consistent with reference [5-6] for conventional paste and firing conditions and explains the higher specific contact-resistance of ~4 mΩ-cm^2 on 100 Ω/sq emitter (Table 5-3). Table 5-2 shows that the same firing condition produced a contact resistance of 0.24 mΩ-cm^2 on the 45 Ω/sq emitter, indicating the need for more or larger Ag crystallites for high sheet-resistance emitters.

The AFM image in Figure 5-5(b) shows that paste B behaves quite differently than paste A for the 750°C firing. Paste B showed a fairly uniform distribution of small Ag crystallites (~25 nm in width). A regular distribution of small Ag crystallites is better for lower contact resistance compared to an irregular distribution of larger Ag crystallites, which are limited to certain regions only. The SEM image in Fig. 5-7 reveals that the Ag crystallites formed at the Ag-Si interface for paste B are on the order of 25-120 nm in size; thus, in some cases they are as large as those formed in the case of PV168 when fired at a higher temperature of 835°C. However, paste B consists of a more aggressive glass frit than PV168 Ag paste, which leads to excessive Ag penetration into the junction. This was confirmed by the SIMS measurements in Fig. 5-8, which reveal the presence of ~3×10^{17}

cm^{-3} Ag at or near the n^+-p junction which is ~0.28 μm deep. This increased the leakage current to 2678 nA/cm^2 (Table 3) and gave a lower FF of 0.635.

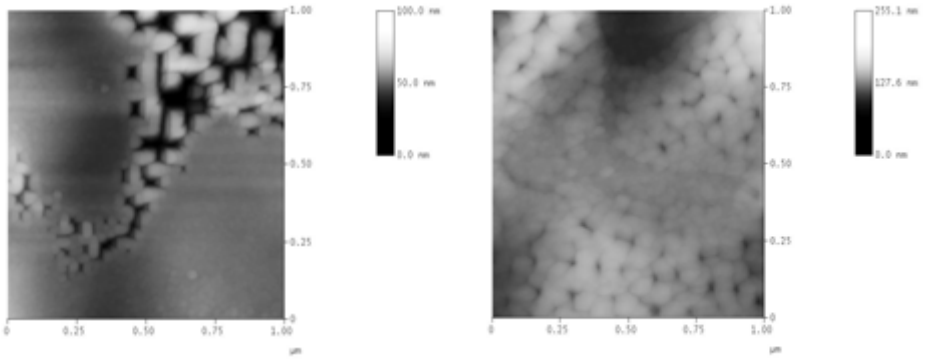

(a) (b)

Figure 5-5. AFM plane-view of the Si interface for (a) paste A and (b) paste B both fired at 750°C.

It has been demonstrated [5-19 – 5-21] that, in addition to promoting adhesion, proper glass frit chemistry can actually retard the Ag migration into the emitter, reducing shunting. Unlike the glass frit in paste PV168, the glass frit in paste B is not effective in arresting Ag close to the Si surface to provide good-quality contact to the shallow high sheet-resistance emitter even at 750°C firing.

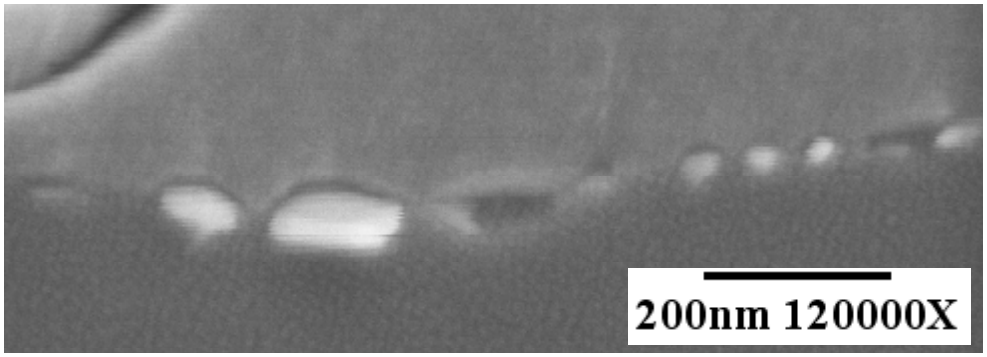

Figure 5-7. SEM of the Ag-Si interface for Paste B fired at 750°C.

Thus, the above analysis explains why pastes A, B and PV168 all failed on the 100 Ω/sq emitter at the conventional firing temperature of 750°C. Paste A failed because of higher contact resistance, attributed to non-uniform distribution of Ag crystallites and low contact area fraction; paste B failed because of the high junction leakage associated with excessive Ag and impurity penetration into the emitter; PV168 failed because of the sparse distribution of smaller Ag crystallites and low contact area fraction, resulting in high contact resistance.

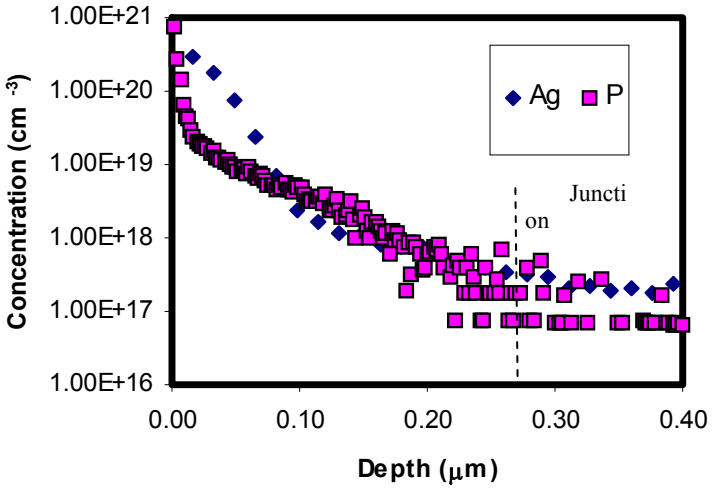

Figure 5-8. SIMS Ag and P profiles in Si for paste B at 750°C firing.

5.3.3 High Temperature (835°C) Firing of Conventional Pastes A and B on the 100 Ω/sq Emitter

The final step in applying this methodology to explain the performance of screen-printed contacts involved the study of the contact interface resulting from 835°C firing of pastes A and B. This is because PV168 worked at high temperature even though it failed at low temperature. The solar cell and contact data in Table 5-4 show that both the pastes failed again at 835°C, with the ideality factor (n) rising above three in conjunction with very high leakage current exceeding 14,000 nA/cm^2. At 835°C, paste A gave very good contact resistance of 0.59 mΩ-cm^2 in conjunction with series resistance of 0.83 Ω-cm^2, but it failed because of a very high junction leakage current (J_{o2}). The EDS measurements (Fig. 5-9) detected the presence of several metal elements in the glass frit of paste A at a very high concentration, deep into the emitter region. In addition, the SIMS measurements (Fig. 5-11) showed the presence of high Ag concentration at the junction.

Paste B failed again because of excessive shunting after the 835°C firing. The SEM image in Figure 5-10 shows a significant increase in the size of Ag crystallites, approaching 0.6-1 μm. Since this is larger than the junction depth of ~0.28 μm, it explains why the 835°C-fired paste B cells were so badly shunted. A comparison of Figs. 5-7 and 5-10 show that the Ag crystallites grew almost 10 times in size (~100 nm⇒ ~1000 nm) when the paste B firing temperature was raised from 750°C to 835°C. This is probably because the glass frit in paste B was able to dissolve a lot more Ag at the higher temperature and became highly supersaturated, producing large precipitates or crystallites at the interface upon cooling. This is also consistent with the Ag-Pb phase diagram [5-22]. The Ag SIMS profiles in Figure 5-11 clearly show that pastes A and B failed because of Ag-induced junction shunting while PV168 survived 835°C firing because of the significantly reduced penetration of Ag into the 100 Ω/sq emitter.

Table 5-4. Electrical performance of solar cells made with pastes A and B on 100 Ω/sq emitters using high-temperature firing.

Paste	Peak Temp	Emitter (Ω/sq)	V_{oc} (mV)	J_{sc} (mA/cm²)	FF	Eff (%)	n factor	R_s (Ω-cm²)	R_{sh} (Ω-cm²)	ρ_c (mΩ-cm²)	J_{o2} (nA/cm²)
Paste A	835	100	579	34.05	0.571	11.25	3.43	0.834	5,222	2.36	14,398
Paste B	835	100	555	34.55	0.528	10.11	3.82	0.490	5,740	0.59	16,139

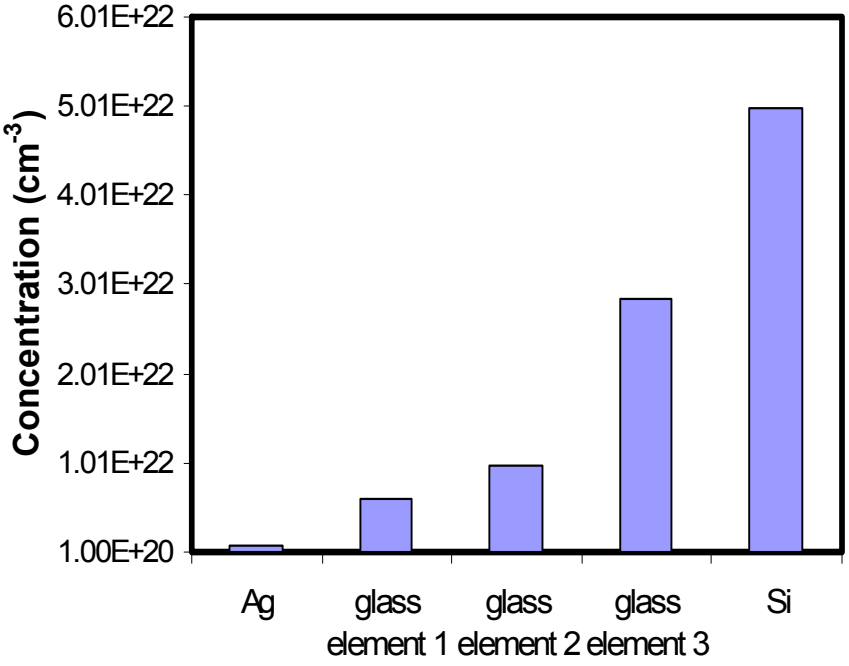

Figure 5-9. EDS analysis of the elements in the emitter region underneath the Ag contact for paste A.

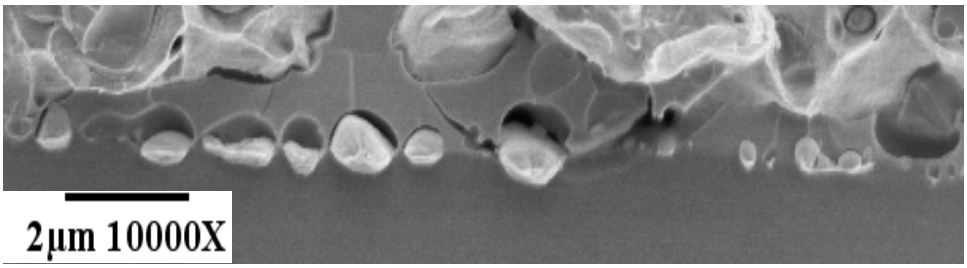

Figure 5-10. SEM images of the Ag-Si interface for paste B fired at 835°C.

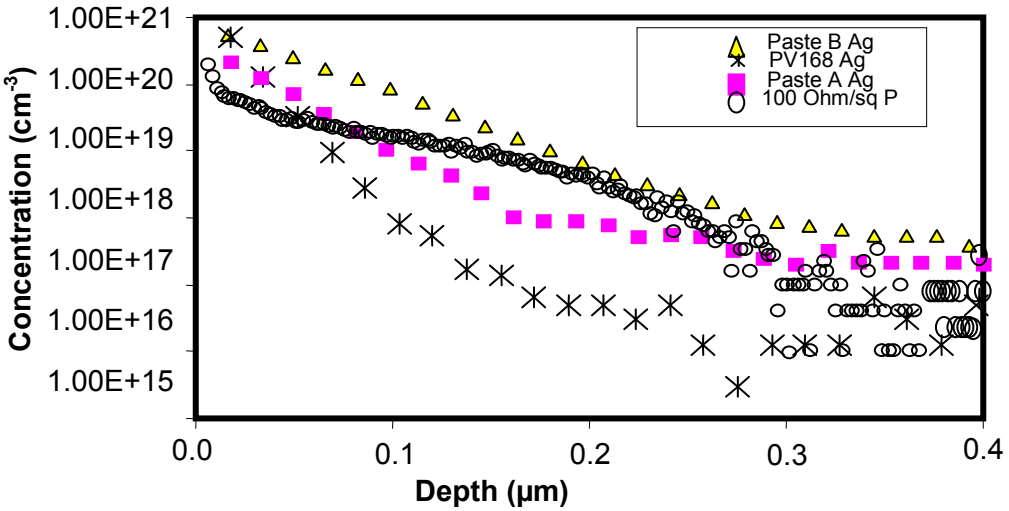

Figure 5-11. SIMS analysis of the three pastes fired at 835°C.

5.4 Conclusion

A combination of SEM or TEM with EDS, and AFM are very useful for understanding the contact structure and composition. These techniques along with the high detection limit of the SIMS analyses has been used to understand and explain the electrical behavior of the screen-printed contacts to high- and low-sheet-resistance emitters. Glass frit chemistry, Ag particle size and shape, and surface treatment of Ag particles should be tailored to minimize Ag migration into the emitter while producing uniform distribution of Ag crystallites with sufficient contact area fraction, which can give good contact resistance without junction shunting. Higher firing temperatures produce larger Ag crystallites. Proper glass frit chemistry can allow for complete etching of the SiN_x layer while arresting the diffusion of Ag into the junction as well.

We found that all the three pastes (A, B, and PV168) investigated in this study failed on the 100 Ω/sq emitter at a firing temperature of ~750°C. Paste A failed because of the non-uniform distribution of Ag crystallites with small contact area fraction. Paste B failed

because of excessive Ag penetration. PV168 failed because of low contact area fraction resulting from incomplete etching of the SiNx coating. At a firing temperature of 835°C, pastes A and B failed on 100 Ω/sq emitter because of junction shunting. Paste A failed because of an aggressive frit allowing excessive penetration of Ag along with other impurities into the emitter while paste B produced Ag crystallites larger than the junction depth. However, PV168 succeeded on the 100 Ω/sq emitter because the 835°C firing allowed the formation of uniform Ag crystallites of reasonable size, ~50 nm or much smaller than the junction depth of ~0.28 μm, while the frit chemistry maintained the Ag penetration below 0.2 μm. Thus, the combination of SEM, AFM, and SIMS measurements is quite effective in understanding the electrical behavior of screen-printed contacts and can lead to the development of screen-printed pastes that can produce high FF and cell performance at appropriate firing temperatures.

5.5 References

[5-1] M. M. Hilali, A. Rohatgi, C. Khadilkar, S. Kim, T. Pham, J. Salami, A. Shaikh, and S. Sridharan, "Development of Thick-Film Ag Paste to Achieve High Fill Factors in Screen-Printed Si Solar Cells with Low- and High-Sheet-Resistance Emitter," *Proc. of 19th European Photovoltaic Solar Energy Conference*, Paris, France, June 2004, in press.

[5-2] M. Prudenziati, L. Moro, B. Morten, and F. Sirotti, "Ag-Based Thick-Film Front Metallization of Silicon Solar Cells," *Active and Passive Electronic Components*, **Vol. 13**, pp. 133-150.

[8-3] C. Ballif, D. M. Huljić, A. Hessler-Wysser, and G. Willeke, "Nature of the Ag-Si Interface in Screen-Printed Contacts: A Detailed Transmission Electron Microscopy Study of Cross-Sectional Structures," *Proc. of the 29th IEEE PVSC*, New Orleans, 2002, pp. 360-363.

[8-4] G. Schubert, B. Fischer, and P. Fath, "Formation and Nature of Ag Thick Film Front Contacts on Crystalline Silicon Solar Cells," PV in Europe Conference, Rome (2002).

[8-5] K. Firor, S. J. Hogan, J. M. Barrett, and R. T. Coyle, "Series Resistance Associated with Thick-Film Contacts to Solar Cells," *Proc. of the 16th IEEE PVSC*, 1982, pp. 824-827.

[8-6] C. Ballif, D. M. Huljić, G. Willeke, and A. Hessler-Wysser, "Silver Thick-Film Contacts on Highly Doped N-type Silicon Emitters: Structural and Electronic Properties of the Interface," *Appl. Phys. Lett.*, **Vol. 82**, No. 12, March 2003, pp. 1878-1880.

[8-7] R. J. S. Young and Alan F. Carroll, "Advances in Front-side Thick Film Metallizations for Silicon Solar Cells," *Proceedings of the 16th European Photovoltaic Energy Conference*, Glasgow, UK, May 2000, pp. 1731-1734.

[8-8] G. C. Cheek, R. P. Mertens, R. Van Overstraeten, and L. Frisson, "Thick-film Metallization for Solar Cell Applications," *IEEE Transactions on Electron Devices*, **Vol. ED-31**, May 1984, pp. 602-609.

[8-9] R. Mertens, M. Eyckmans, G. Cheek, M. Honore, and R. Van Overstraten, "Critical Processing Parameter Optimization for Screen-Printed Semicrystalline Silicon Solar Cells," *Proc. of the 17th IEEE PVSC*, 1984, pp.1347-1351.

[8-10] M. Hilali, J.–W. Jeong, A. Rohatgi, D. L. Meier, and A. F. Carroll, "Optimization of Self-Doping Ag Paste Firing to Achieve High Fill Factors on Screen-Printed Silicon Solar Cells with a 100 Ω/sq. Emitter," *Proc. of the 29th IEEE PVSC*, New Orleans, May 2002, pp.356-359.

[8-11] M. M. Hilali, A. Rohatgi, and S. Asher, "Development of Screen-Printed Silicon Solar Cells with High Fill Factors on 100 Ohms/sq Emitters," *IEEE Trans. On Elect. Dev.,* **Vol. 51**, No. 6, June 2004, pp. 948-955.

[8-12] D. K. Schroder, Semiconductor Material and Device Characterization, New York: John Wiley & Sons, Inc., 1990.

[8-13] J. C. Lin, and C. Y. Wang, "Effect of Surfacant Treatment of Silver Powder on the Rheology of its Thick-Film Paste," *Materials Chemistry and Physics*, **Vol. 45**, 1996, pp. 136-144.

[8-14] S. B. Rane, P. K. Khanna, T. Seth, G. J. Phatak, D. P. Amalnerkar, and B. K. Das, "Firing and Processing Effects on Microstructure of Fritted Silver Thick Film Electrode Materials for Solar Cells," *Materials Chemistry and Physics*, Vol. 82, 2003, pp. 237-245.

[8-15] J. C. Lin, and C. Y. Wang, "Effect of Surface Properties of Silver Powder on the Sintering of its Thick-Film Conductor," *Materials Chemistry and Physics*, **Vol. 45**, 1996, pp. 253-261.

[8-16] O Growski, L. Murawski, and K. Trzebiatowsky, "The Surface Conductivity of Lead Glasses," *Journal of Physics D: Applied Physics*, **Vol. 15**, 1982, pp. 1097-1101. edited by T. B. Massalski, (American Society for Metals, Materials Park, OH, 1990) pp. 92-94.

[8-18] D. L. Meier, Hubert P. Davis, Ruth A. Garcia, and Joyce A. Jessup, "Method and Apparatus for Self-Doping Contacts to a Semiconductor," Ebara Corporation, U.S. patent #6,703,295, March, 2004.

[8-19] C. Khadilkar, S. Kim, T. Pham, A. Shaikh, and S. Sridharan, "Characterization of Silver Front Contact in a Silicon Solar Cell," *Technical Digest of the14th International Photovoltaic Specialists Energy Conference,* Bangkok, Thailand, 2004, pp. 443-444.

[8-20] A. Shaikh, S. Sridharan, T. Pham, and C. Khadilkar, "Designing a Front Contact Ink for SiN_x Coated Si Solar Cells" " *3rd World Conference on Photovoltaic Energy Conversion*, Osaka, Japan, May, 2003.

[8-21] S. Sridharan, C. Khadilkar, T. Pham, and A. Shaikh "Characterization of Silver/Glasss/Silicon Front Contact Interface in a Silicon Solar Cell" *presented at the 13th Workshop on Crystalline Silicon Solar Cell Materials and Processes*, Vail, Colorado, August, 2003, pp. 162-165.

[8-22] I. Karakaya and W. T. Thompson in *Binary Alloy Phase Diagrams*, 2nd edition edited by T. B. Massalski, (American Society for Metals, Materials Park, OH,1990), pp.72-73.

REPORT DOCUMENTATION PAGE

Form Approved
OMB No. 0704-0188

PLEASE DO NOT RETURN YOUR FORM TO THE ABOVE ORGANIZATION.

1. REPORT DATE *(DD-MM-YYYY)*	2. REPORT TYPE	3. DATES COVERED *(From - To)*
November 2007	Subcontract Report	March 2002 – July 2006

4. TITLE AND SUBTITLE
Fundamental Research and Development for Improved Crystalline Silicon Solar Cells: Final Subcontract Report, March 2002 – July 2006

5a. CONTRACT NUMBER
DE-AC36-99-GO10337

5b. GRANT NUMBER

5c. PROGRAM ELEMENT NUMBER

6. AUTHOR(S)
A. Rohatgi

5d. PROJECT NUMBER
NREL/SR-520-42324

5e. TASK NUMBER
PVA72101

5f. WORK UNIT NUMBER

7. PERFORMING ORGANIZATION NAME(S) AND ADDRESS(ES)
Georgia Institute of Technology
Atlanta, Georgia 30332-0420

8. PERFORMING ORGANIZATION REPORT NUMBER
AAT-2-31605-02

9. SPONSORING/MONITORING AGENCY NAME(S) AND ADDRESS(ES)
National Renewable Energy Laboratory
1617 Cole Blvd.
Golden, CO 80401-3393

10. SPONSOR/MONITOR'S ACRONYM(S)
NREL

11. SPONSORING/MONITORING AGENCY REPORT NUMBER
NREL/SR-520-42324

12. DISTRIBUTION AVAILABILITY STATEMENT
National Technical Information Service
U.S. Department of Commerce
5285 Port Royal Road
Springfield, VA 22161

13. SUPPLEMENTARY NOTES
NREL Technical Monitor: Richard Matson/Fannie Posey-Eddy

14. ABSTRACT *(Maximum 200 Words)*
This report summarizes the progress made by Georgia Tech in the 2002-2006 period toward high-efficiency, low-cost crystalline silicon solar cells. This program emphasize fundamental and applied research on commercial substrates and manufacturable technologies. A combination of material characterization, device modeling, technology development, and complete cell fabrication were used to accomplish the goals of this program. This report is divided into five sections that summarize our work on i) PECVD SiN-induced defect passivation (Sections 1 and 2); ii) the effect of material inhomogeneity on the performance of mc-Si solar cells (Section 3); iii) a comparison of light-induced degradation in commercially grown Ga- and B-doped Czochralski Si ingots (Section 4); and iv) the understanding of the formation of high-quality thick-film Ag contacts on high sheet-resistance emitters (Section 5).

15. SUBJECT TERMS
PV; silicon; research and development; solar cells; crystalline; high efficiency; low cost; characterization; device modeling; defect passivation; light-induced degradation; Ag contacts;

16. SECURITY CLASSIFICATION OF:			17. LIMITATION OF ABSTRACT	18. NUMBER OF PAGES	19a. NAME OF RESPONSIBLE PERSON
a. REPORT	b. ABSTRACT	c. THIS PAGE			
Unclassified	Unclassified	Unclassified	UL		19b. TELEPHONE NUMBER (*Include area code*)

Standard Form 298 (Rev. 8/98)
Prescribed by ANSI Std. Z39.18